UNIVERSITAT POLITÈCNICA
DE CATALUNYA

COMPUTATIONAL AND APPLIED PHYSICS PROGRAM

Thermal convection in rotating spherical shells

Ferran Garcia Gonzalez

Thesis report presented to obtain the Doctor Degree of the Universitat Politècnica de Catalunya under the supervision of Dr. Juan Sánchez Umbría and Dr. Marta Net Marcé.

Barcelona, 2012

Chapter 5

Low Prandtl number finite-amplitude convection: non-slip boundary conditions

5.1 Introduction

This chapter is devoted to the study of the flows and patterns of convection bifurcated from the primary travelling waves. Several numerical studies describe oscillatory types of convection at different regions of the parameter space, mainly with stress-free boundary conditions (see [129, 3, 114, 29, 106] among others). In [129] it was found, for $\sigma = \infty$, that the instability of the travelling waves gives rise to amplitude or shape modulations. Several types of oscillations with different azimuthal wave numbers were found at low σ in [3]. In both cases they found an strong increase of the heat transfer produced by the onset of the vacillations. A more detailed study of the finite-amplitude physical properties, including helicity or differential rotation, and of the role of equatorial symmetry or the onset of polar convection is performed in [114] for several Prandtl numbers. With $\sigma = 1$ and for weak supercritical conditions the flow is strongly oscillatory displaying an intermittent pattern [29].

Intermittent transition to turbulence was first described in [92] in the simple dissipative Lorenz model. It was shown that the intermittent behaviour comes from an instability of a periodic motion. A new type of intermittent route to chaos, in presence of symmetry, was described in [85]. In this case at the bifurcation, two unstable cycles merge into a stable one to produce an unstable limit cycle. Such transition can be observed in hydrodynamic systems with symmetric boundary conditions.

For slow rotating self-graviting spherical shells, [28, 27] demonstrate the existence of a robust heteroclinic cycle near the onset of convection, which is the responsible of the intermittent behaviour. However, in fast rotating spherical shells with stress free

boundary conditions, equatorially symmetric intermittent structures were also found [51, 50, 29, 106]. In these type of flows, there are intermittent periods in which the fluid is nearly stagnant, and periods with strong localised convection. The latter convective structures, which regenerate the differential rotation are destroyed by the action of the shear of the flow. According to [6], it is not clear if this behaviour could persist even if the dissipation were in the boundary layers, rather than in the interior of the fluid.

Using three-dimensional numerical computations and the free-slip case, [29] predicts, using the scaling laws in the limit of negligible viscosity, the observed magnitude of the zonal winds at the surface of the large gas planets. As noticed in the introduction, small-scale convection transfers kinetic energy into the strong mean zonal flow via Reynolds stresses. The Earth's core zonal flow can not be predicted by the analysis of [29], not only due to the friction in the Ekman boundary layers, but also mainly by the effect of the electromagnetic stresses which tend to damp zonal motions.

The role of zonal circulations in Earth's outer core models has also been analysed in experimental and numerical studies [6, 104, 41]. In the experiments the gravity force is supplied by the centrifugal acceleration, thus changing to cylindrical the radial dependence of the buoyancy force. However, this is of secondary importance at low and mid-latitudes.

Making use of the quasi-geostrophic approximation, scaling laws for the zonal flow and other mean quantities were obtained and contrasted with experimental results in [6], these scaling laws were revisited in [41]. In contrast, in [104] other model approximations were used to derive new asymptotic laws. In the latter study, the differences with the scalings of [6, 29] were analysed. These scaling laws are used to extrapolate realistic values on the Earth's outer core, but have never been contrasted with three-dimensional numerical simulations.

The mathematical model, widely used to derive the partial differential evolution equations, their spatial discretization, and the time integration method used in the present study, are described in chapter 4. For further details see Secs. 4.2 and 4.3 and references therein. The numerical solutions can be computed by imposing a m_d-fold azimuthal symmetry. This is accomplished by only retaining the modes with wave number $m = km_d$, $k \in \mathbb{Z}$, in the truncated spherical harmonics expansion of the unknowns (Eq. (4.6) of Sec. 4.2). Besides of reducing the numerical effort for obtaining time-averaged properties of strongly supercritical flows, the constrains on the symmetry can be used to found unstable flows near the onset. However, one must be cautious in the use of the symmetry assumptions because of the possibility of finding solutions which are unstable with respect to perturbations breaking the symmetry.

Non-slip boundary conditions are applied for comparative purposes with previous laboratory experiments [6, 104, 41]. In these experiments, the temperature difference is applied through the lids, so differential heating is considered in the model. Then in this part of the study $Ra = Ra_e$ has been used. In addition the estimated Prandtl number $\sigma = 0.1$ for the Earth's outer core and its radius ratio $\eta = 0.35$ is considered [6]. A moderate value of η ensures a moderately small critical wave number at the onset of con-

vection [1], which reduces considerably the number of spatial discretization points. On the other hand, real applications are characterised by high Taylor, or, equivalently, low Ekman numbers. Our simulations are performed with $E \lesssim 10^{-4}$, which is a value far away from those of real applications, but it is sufficiently small to belong to the asymptotic regime, where the power laws of the critical parameters at the onset are satisfied (Chapter 3).

The critical parameters at the onset of convection, such as the critical Rayleigh number R_c, the critical precession frequency ω_c and the critical azimuthal wave number m_c, depending on E, where obtained in Chapter 3 and are also summarised in Table 5.8 of Appendix A. With $E = 10^{-4}$, the first bifurcation, which breaks the axisymmetry of the conductive state, is a supercritical Hopf bifurcation giving rise to a $m = 6$ wave, travelling in the azimuthal direction. The preferred eigenfunctions are symmetric with respect to the equator, and they have negative precession frequencies ω_c, namely the drifting velocities $c = -\omega_c/m$ are positive, and the waves travel in the prograde direction. Moreover, they consist of quasi-geostrophic convective columns attached to the inner sphere and confined in a coaxial cylinder of radius $r_i < r_c < r_o$.

The results presented here extend previous stress-free numerical studies [29], by using non-slip boundary conditions and the low Prandtl number $\sigma = 0.1$. The oscillatory types of convection, as well as the scaling of the flow properties in the regime of fully developed convection, are studied. In addition, the experimental results and scaling laws of [6, 104, 41] are compared with our three-dimensional DNS simulations. Finally our results are used to extrapolate physical values in a similar situation to the present day Earth's outer core.

The study is organised as follows: First, the definition of the flow properties which will be studied is introduced in Sec. 5.2. The oscillatory types of convection found when the Rayleigh number is increased, from weak to strong supercritical values, are described in Sec. 5.3. The study of the variation of the location of the convection with Ra is performed in Sec. 5.4 by computing relevant physical properties at different collocation points inside the shell. The purpose of Sec. 5.5 is following [29] to find asymptotic relations for the limit where viscosity plays a negligible role. In Sec. 5.6 a comparison with previous experimental results and scaling laws is performed. In Sec. 5.7 the scalings are used to extrapolate Earth's outer core values and the final conclusions are discussed in Sec. 5.8. Finally, in the Appendix A the numerical results are validated.

5.2 Selected output data of the flows

Several output data are presented in this study. The local output data consists of snapshots of selected variables of the problem at selected inner points of the domain. Typically the components of the velocity field $\mathbf{v} = \nabla \times (\Psi \mathbf{r}) + \nabla \times \nabla \times (\Phi \mathbf{r})$ evaluated at representative points, or the real part of some spherical harmonic coefficients of the temperature

perturbation $\mathcal{R}\Theta_l^m(r_j,t)$ at some radial positions r_j, are taken.

Global data are physical properties averaged over the whole volume, or on the surface of a sphere. They can be expressed as time scalar functions $P(t) = P(u(t)) \in \mathbb{R}$, being $u(t) = (\Psi_l^m(t,r_j), \Phi_l^m(t,r_j), \Theta_l^m(t,r_j))$ a solution vector of Eqs. (4.7)-(4.9) in Sec. 4.2, containing the values of the spherical harmonic coefficients of the potentials, and the temperature perturbation at the radial collocation points r_j and time instant t. The global data shown in the following sections are defined next.

The heat transfer by convection is measured by the ratio of the average of the total radial heat flux to the conductive heat flux, both through the outer surface, namely the Nusselt number is defined by

$$Nu = \frac{< J_T(r_o,\theta,\varphi) >}{< J_c(r_o) >},$$

where $<>$ means the surface integral evaluated at $r = r_o$. It follows that

$$Nu - 1 = -(\sqrt{2}\sigma/2\eta Ra)\partial_r \Theta_0^0(t,r_o),$$

where Θ_0^0 is the zero degree and order amplitude of the spherical harmonic coefficient of the temperature perturbation.

The volume-averaged kinetic energy density, from now on kinetic energy density (KED), is given by

$$K = \frac{1}{2\mathcal{V}} \int_{\mathcal{V}} \mathbf{v}\cdot\mathbf{v} dv = (3\sqrt{2}/4(r_o^3 - r_i^3)) \int_{r_i}^{r_o} r^2 [\mathbf{v}\cdot\mathbf{v}]_0^0(t,r) dr, \tag{5.1}$$

where $\mathcal{V}$ refers to the volume of the fluid shell. The previous volume integral can also be computed either for the toroidal component $\nabla \times (\Psi \mathbf{r})$ or for the poloidal component $\nabla \times \nabla \times (\Phi \mathbf{r})$ of the velocity field, giving rise to either the toroidal K_t or the poloidal K_p kinetic energy density. From Eq. (5.1) the axisymmetric and the non-axisymmetric kinetic energy densities can be defined. They retain, respectively, the $m = 0$ or the $m \neq 0$ modes of the spherical harmonic expansion of the potentials Ψ and Φ. From now on we will call zonal KED, K_z to the axisymmetric part of the energy. In fact it also contains radial and colatitudinal poloidal components, but we have checked (in agreement with [106]) that the poloidal part is at least one order of magnitude smaller than the toroidal azimuthal one, so K_z basically comes from the axisymmetric toroidal flow which is only zonal. According to [29] we will call non-zonal KED to the non-axisymmetric KED, K_{nz}.

From the kinetic energy densities defined above, the Reynolds number is obtained as $Re_* = \sqrt{2K_*}$, and the Rossby number as $Ro_* = Re_* E$. The former measures the ratio of inertial to viscous forces, and the latter measures the ratio of inertial to Coriolis forces.

Symbol	Definition
Ψ, Φ, Θ	Toroidal potential, poloidal potential and temperature perturbation.
$X = (\Psi, \Phi, \Theta)$	Spherical harmonic series, $X = \sum_{l=0}^{L} \sum_{m=-l}^{l} X_l^m(r,t) Y_l^m(\theta, \varphi)$, where X_l^m are the complex amplitudes.
$\|\|u\|\|$	Norm of the vector of the amplitudes X_l^m.
$\|\|u_k\|\|$	Norm of the vector of the amplitudes X_l^m with $m = kn$, $n \in \mathbb{N}$.
$\mathbf{T}$	Toroidal field, $\mathbf{T} = \nabla \times (\Psi \mathbf{r})$.
$\mathbf{P}$	Poloidal field, $\mathbf{P} = \nabla \times \nabla \times (\Phi \mathbf{r})$.
$\mathbf{v}$	Velocity field, $\mathbf{v} = \mathbf{T} + \mathbf{P}$.
v_φ	Azimuthal component of the velocity field.
$[v_\varphi]$	Azimuthal average of v_φ or zonal flow, $[v_\varphi](t,r,\theta) = \frac{1}{2\pi} \int_0^{2\pi} v_\varphi d\varphi$.
$[\overline{v_\varphi}]$	Time average of $[v_\varphi]$ or mean zonal flow.
K	Kinetic energy density (K.E.D), $K = \frac{1}{2\mathcal{V}} \int_\mathcal{V} \mathbf{v} \cdot \mathbf{v} \, dv$.
K_z	Zonal K.E.D, $K_z = \frac{1}{2\mathcal{V}} \int_\mathcal{V} \mathbf{v}_{m=0} \cdot \mathbf{v}_{m=0} \, dv$.
K_{nz}	Non-zonal K.E.D, $K_{nz} = \frac{1}{2\mathcal{V}} \int_\mathcal{V} \mathbf{v}_{m\neq 0} \cdot \mathbf{v}_{m\neq 0} \, dv$.
K_t	Toroidal K.E.D, $K_t = \frac{1}{2\mathcal{V}} \int_\mathcal{V} \mathbf{T} \cdot \mathbf{T} \, dv$.
K_p	Poloidal K.E.D, $K_p = \frac{1}{2\mathcal{V}} \int_\mathcal{V} \mathbf{P} \cdot \mathbf{P} \, dv$.
Re	Reynolds number, $Re = \sqrt{2K}$.
Ro	Rossby number, $Ro = ReE$.
U	Dimensional velocity, $U = \nu Re / d$.
σ_{d_s}	Relative variance of a time series d_s, $\sigma_{d_s} = \sqrt{\overline{(d_s - \overline{d_s})^2}} \; / \; \overline{d_s}$.

Table 5.1: Summary of symbols and definitions for the output data used along this section. The parameters E, σ, η, Ra, and the constants ν and d are defined in Sec. 4.2 of Chapter 4.

The symbols and the definition of the physical properties that will be studied along this chapter are summarised in Table 5.1. Notice that the word *mean* is used along the work only to indicate time-averaged quantities. For further details on the definition of the dimensionless parameters and the physical constants see Sec. 4.2 of Chapter 4.

Whatever the data d_s be local or global, a time series of the form $(t_i, d_s(t_i))$, $i = 1, \ldots, N$ is obtained, and its average $\overline{d_s}$ and relative variance can be computed. The relative variance σ_{d_s} is defined as

$$\sigma_{d_s} = \frac{\sqrt{\overline{(d_s - \overline{d_s})^2}}}{\overline{d_s}}.$$

In addition to these statistical quantities, the desired $f_1, \ldots, f_{N_f}$ frequencies of maximum amplitude of the time series d_s are obtained with enough accuracy by means of the Laskar's Numerical Analysis of Fundamental Frequencies (NAFF) package [71] implemented by [12]. Although there exist more accurate procedures, such as [47] and references therein, that of [71] has been found sufficient to identify periodic, quasiperiodic, resonant, and chaotic motions within our numerical integration errors (see Appendix A).

5.3 Route to chaos

One of the purposes of this section is to extend previous studies [129, 3, 114, 29, 106] by using non-slip boundary conditions. The changes on the structure, and on the physical properties of the flow, that occur when the Rayleigh number Ra is increased from its critical value up to $Ra = 2 \times 10^6$, while the other parameters $E = 10^{-4}$, $\sigma = 0.1$ and $\eta = 0.35$ are kept constant, unless otherwise stated, will be described. Of course, the path followed to find the solutions may change depending on the sequence of Ra, and on the initial conditions chosen. Our procedure to obtain the solutions is described in Appendix A.

Aside from the use of non-slip boundary conditions, another goal of this study is to try to explain the different oscillatory solutions in the context of the Dynamical System theory. Periodic orbits, attracting 2-tori, and even attracting 3-tori as well as chaotic attractors will be described.

Other studies such as [84], or [109], describe also attracting 3-tori in their routes to chaos using a dynamical system derived from a system of ordinary differential equations. The characterisation of the route is performed by means of the largest Lyapunov exponents and the Kaplan-Yorke dimension of the attractors. Because of the numerical effort of computing Lyapunov exponents in a very high-dimensional system, the route to chaos described in this section is characterised by computing directly the frequency spectrum of the solutions as a first step. So, the chaotic behaviour of the solutions will not be quantified. This will be done in the near future.

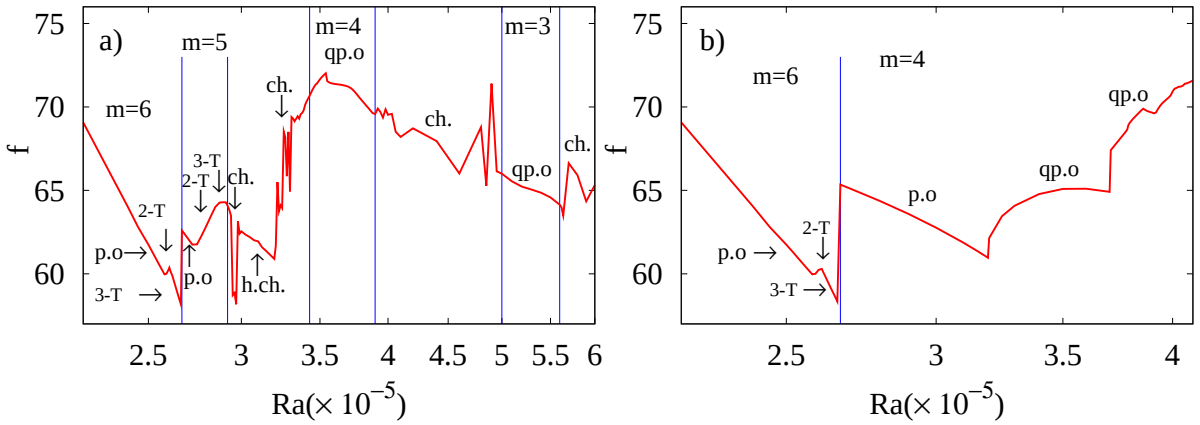

Figure 5.1: Main frequency of the time series of the temperature perturbation Θ at the point $(r, \varphi, \theta) = (r_i + (r_i - r_o)/7, 0, 3\pi/8)$, plotted versus the Rayleigh number in logarithmic scale. The frequency is obtained using Laskar's algorithm. (a) Solutions computed without symmetry assumptions ($m_d = 1$), (b) computed with two-fold azimuthal symmetry ($m_d = 2$).

In Fig. 5.1(a) the frequency with maximum amplitude of the frequency spectrum of the time series of the temperature perturbation Θ at the point $(r, \varphi, \theta) = (r_i + (r_o - r_i)/7, 0, 3\pi/8)$ is plotted versus the Rayleigh number. The same representation is used in Fig. 5.1(b), but solutions are computed by imposing two-fold azimuthal symmetry. These figures help to identify Ra intervals (separated by vertical lines) of different dynamics, which will be studied in detail in the next subsections. The labels $m = 3, 4, 5, 6$ which appear on the figure indicate the azimuthal wave number m that dominates the dynamics, the labels p.o, 2-T, and 3-T, indicate periodic orbits, 2-tori, and 3-tori, respectively, and the labels ch., qp.o., and h.ch. indicate chaotic, quasiperiodic and heteroclinic chain orbits, respectively. It is worth noticing that the position of the vertical lines may change depending on the path followed for increasing Ra. For instance, due to hysteresis, at $Ra = 2.65 \times 10^5$ at which a 3-T $m = 6$ solution is obtained, an $m = 5$ p.o can also be found if the initial condition is the $m = 5$ p.o corresponding to $Ra = 2.66 \times 10^5$.

Figs. 5.2, and 5.3 show the average and the normalised variance, respectively, of the time series of (a) the Rossby number $\overline{Ro} = E\overline{Re}$, being $\overline{Re} = \overline{\sqrt{2K}}$ the mean Reynolds number, (b) the ratio of the total to the non-zonal kinetic energy densities $\overline{K/K_{nz}}$, (c) the poloidal Rossby number $\overline{Ro_p} = E\overline{Re_p}$, being $\overline{Re_p}$ the mean poloidal Reynolds number, and (d) the Nusselt number $\overline{Nu}$, plotted versus Ra. The changes in the dynamics are best reflected in the ratio $\overline{K/K_{nz}}$ and in the relative variance plots.

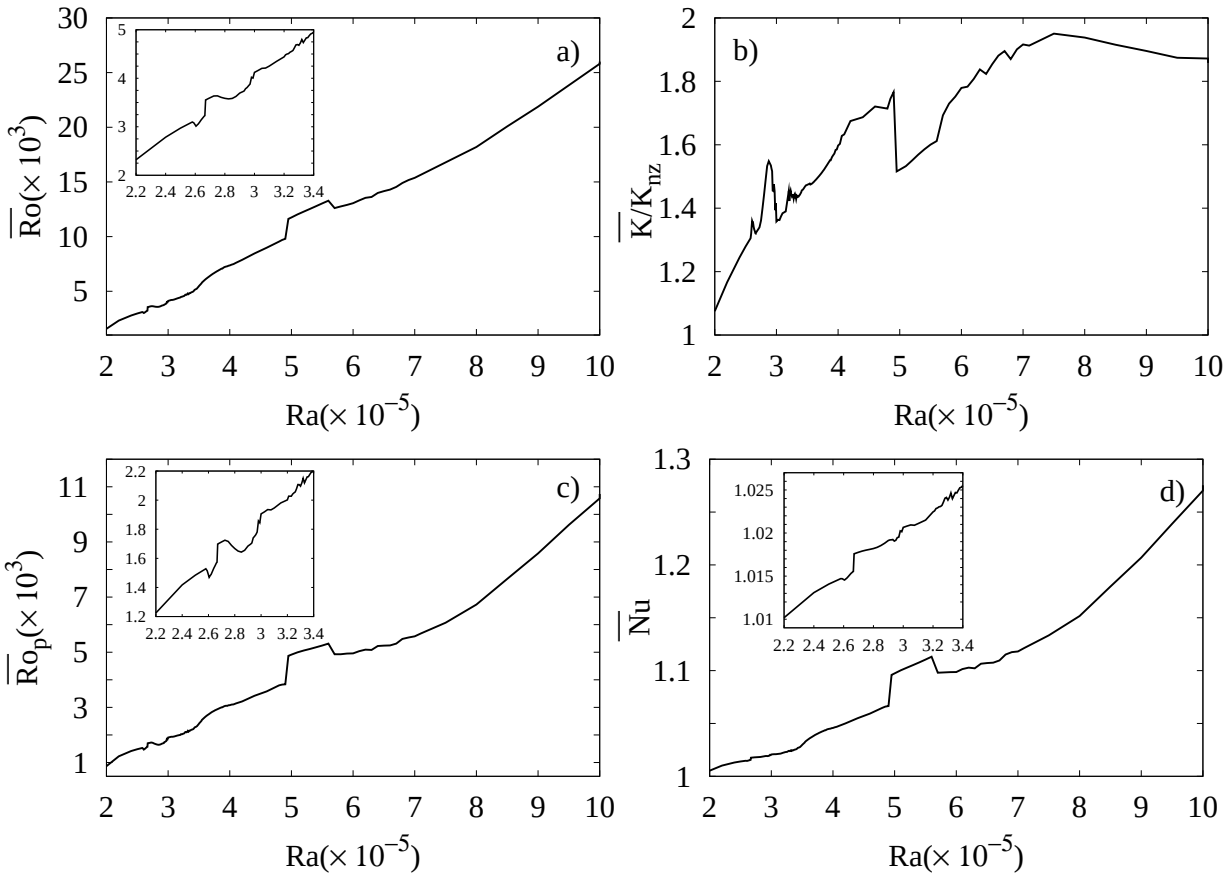

Figure 5.2: Time averages of some physical properties plotted versus the Rayleigh number, Ra. (a) Rossby number, $\overline{Ro}$, (b) ratio of the total to the non-zonal kinetic energy densities, $\overline{K/K_{nz}}$, (c) poloidal Rossby number, $\overline{Ro_p}$, and (d) the Nusselt number $\overline{Nu}$.

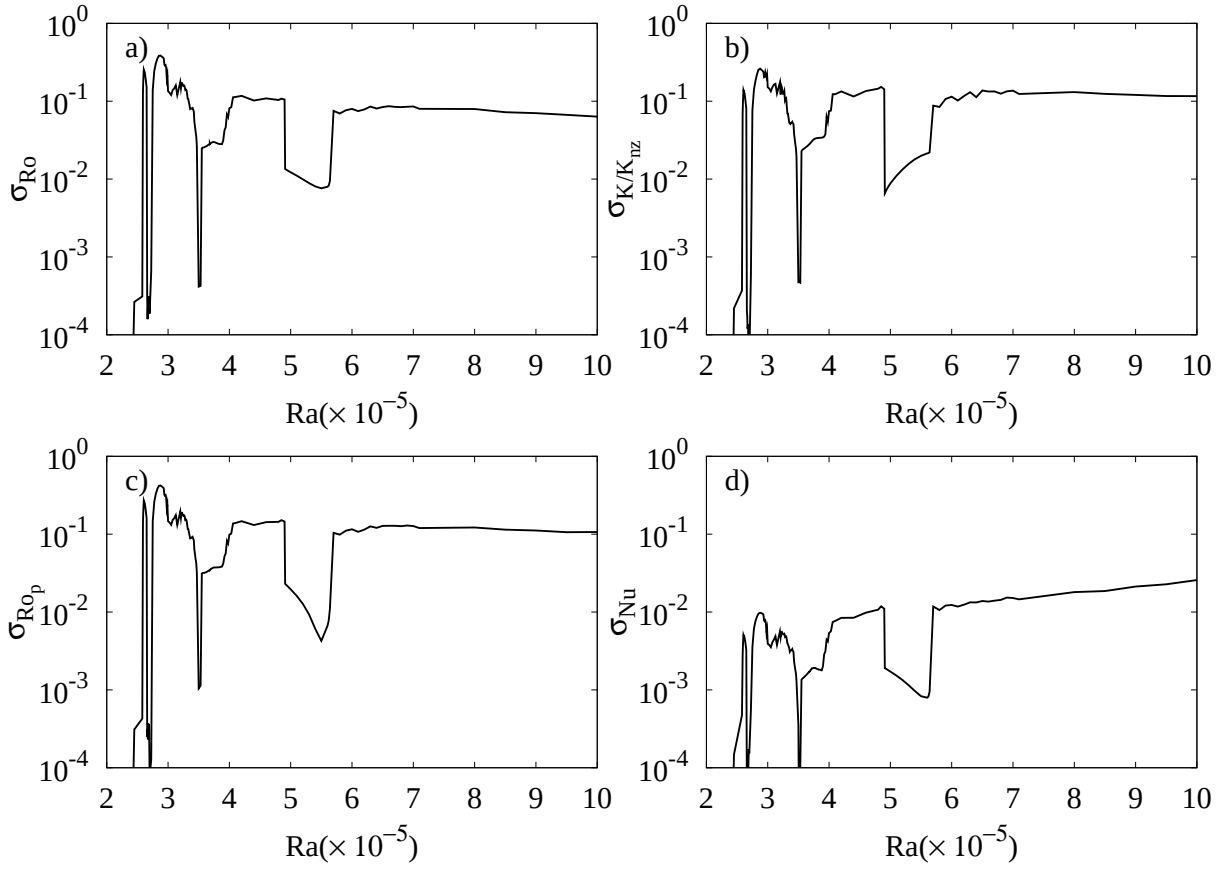

Figure 5.3: Normalised variance for the physical properties of Fig. 5.2 plotted versus the Rayleigh number, Ra.

In each of the following subsections the information provided by Figs. 5.1, 5.2, and 5.3 is interpreted and related to the flow patterns shown in the contour plots presented. Different sets of solutions are found and the relative contribution of the relevant azimuthal wave numbers to the convection is quantified for each set. Finally, Poincaré sections and frequency spectra are used to visualise the differences between the solutions.

5.3.1 $m = 6$ and $m = 5$ branches of solutions

5.3.1.1 Physical description of the waves

In this subsection the physical properties and the flow patterns of the solutions obtained for $Ra < 2.91 \times 10^5$ are studied. When Ra is increased from 2×10^5 to 2.58×10^5 the frequency of the $m = 6$ solutions decreases monotonically (see Fig. 5.1(a)), because of the action of the Reynolds stress due to the spiralling of the travelling waves [106]. In addition the convection remains confined in a cylinder whose critical radius r_c becomes larger, and the heat transfer through the outer boundary also increases, as it is reflected in the Nusselt number in Fig. 5.2(d). The increase of the spiralling nature of the flow also favours the zonal circulation, which increases monotonically with the Rayleigh number as can be seen in the ratio $\overline{K/K_{nz}}$ in Fig. 5.2(b). Notice that in the latter figure the zonal flow of the travelling waves, only carries less than 20% of the kinetic energy density. This is a characteristic of the non-slip boundary conditions (see [29] and references therein). As can be seen in Fig. 5.3 the relative variance of the properties is nearly zero, which correspond to the fact that the global physical properties are time independent since the flow pattern is steady (aside from its azimuthal drift).

At approximately $Ra_1 = 2.59 \times 10^5$ the $m = 6$ travelling wave starts to oscillate in several ways labelled as 2-T and 3-T in Fig. 5.1(a), until a critical value $Ra_2 = 2.65 \times 10^5$ is achieved. From this value, there is a jump to the $m = 5$ travelling wave indicated by the first vertical line in Fig. 5.1(a). Its large spatial scale is the responsible of its large heat transport (see detail of Fig. 5.2(d)) and drifting rate (see Fig. 5.1(a)). The $m = 5$ travelling waves can also be identified in Fig. 5.3, where there is a small range near $Ra = 2.7 \times 10^5$ in which the relative variance vanishes. From there, as the Rayleigh number is further increased, the oscillations on the $m = 5$ branch become noticeable until $Ra_3 \approx 2.9 \times 10^5$ is achieved.

Figure 5.4 shows, from left to right, a snapshot of the contour plots of a $m = 6$ travelling wave at $Ra = 2.45 \times 10^5$ and an $m = 6$ amplitude oscillating flow at $Ra = 2.6 \times 10^5$. Three projections of Θ are displayed for each solution (see figure caption). The projections on the left are taken on spheres, whose radii correspond approximately to the maximum of the temperature perturbation. They have radii $r = r_i + 0.25d$, although they are represented with the size of the other sections. The middle projections are taken on the equatorial plane, and those on the right on a meridional section at $\varphi = 0$. The scale of colours is the same for the contour plots corresponding to each solution, with red meaning

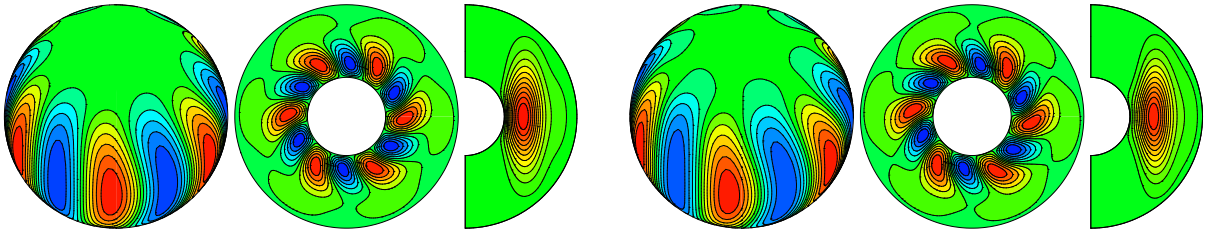

Figure 5.4: Contour plots of the temperature perturbation on a sphere, on the equatorial plane, and on a meridional section. At left travelling wave at $Ra = 2.45 \times 10^5$. At right solution corresponding to an amplitude oscillation at $Ra = 2.6 \times 10^5$.

hot fluid. Unless otherwise stated from now on all the contour plots will be represented on spherical and equatorial sections crossing the maximum of one cell or vortex, and those meridional will be taken at $\varphi = 0$. Fig. 5.5 at $Ra = 2.78302 \times 10^5$ shows a sequence of six snapshots corresponding nearly to a half period of an amplitude oscillation of an $m = 5$ amplitude oscillating wave (AOW).

The amplitude oscillations consist of very weak expansions and contractions of the convective cells without breaking the azimuthal symmetry. This can be observed in the snapshots of Fig. 5.5. As a consequence of the expansions the convective cells connect at high latitudes, favouring the zonal circulation of the fluid. In this case, the zonal flow carries about 30% of the kinetic energy density. The increase of the zonal circulation is more pronounced in the $m = 5$ AOW, as shown in Figs. 5.2(b) and 5.3(b), because its azimuthal and radial scale are larger, and then zonal circulations take place on a wider region of the shell. The connection of the convective cells, diminishes the action of the Reynolds stresses and then the drift rate is increased (see Fig. 5.1(a)). In contrast, the effect of the oscillations is to reduce the time-averaged poloidal, as well as the total Rossby numbers, and to reduce the slope of the $\overline{Nu}$ dependence on Ra (see Figs. 5.2(a, c, d)). Accordingly to the oscillatory behaviour of these solutions, the relative variance of the physical properties increases with the Rayleigh number (see Fig. 5.3). Notice in this figure, and also in Fig. 5.1, that the AOW (2-T) with $m = 5$ persist in a large interval of Rayleigh numbers.

After the regime of quasiperiodic AOW, either with $m = 6$ or $m = 5$, irregular amplitude oscillations of the cells occur due to the nonlinear interaction of the neighbouring modes. When the convection is generated by the interaction of at least m_1 and m_2 modes verifying $m_1 \neq km_2, \forall\ k\ \in \mathbb{Z}$ the azimuthal symmetry of the solution is broken giving rise to cells of different shape, which change in time. These type of solutions will be named, from now on, irregular amplitude oscillating waves (IAOW). Secondary and tertiary instabilities for fluids in spherical shells with infinite σ were studied in detail in [129], and where interpreted in [127] as the simplest transition from the travelling waves. These instabilities are caused by Ekhaus-type mechanisms.

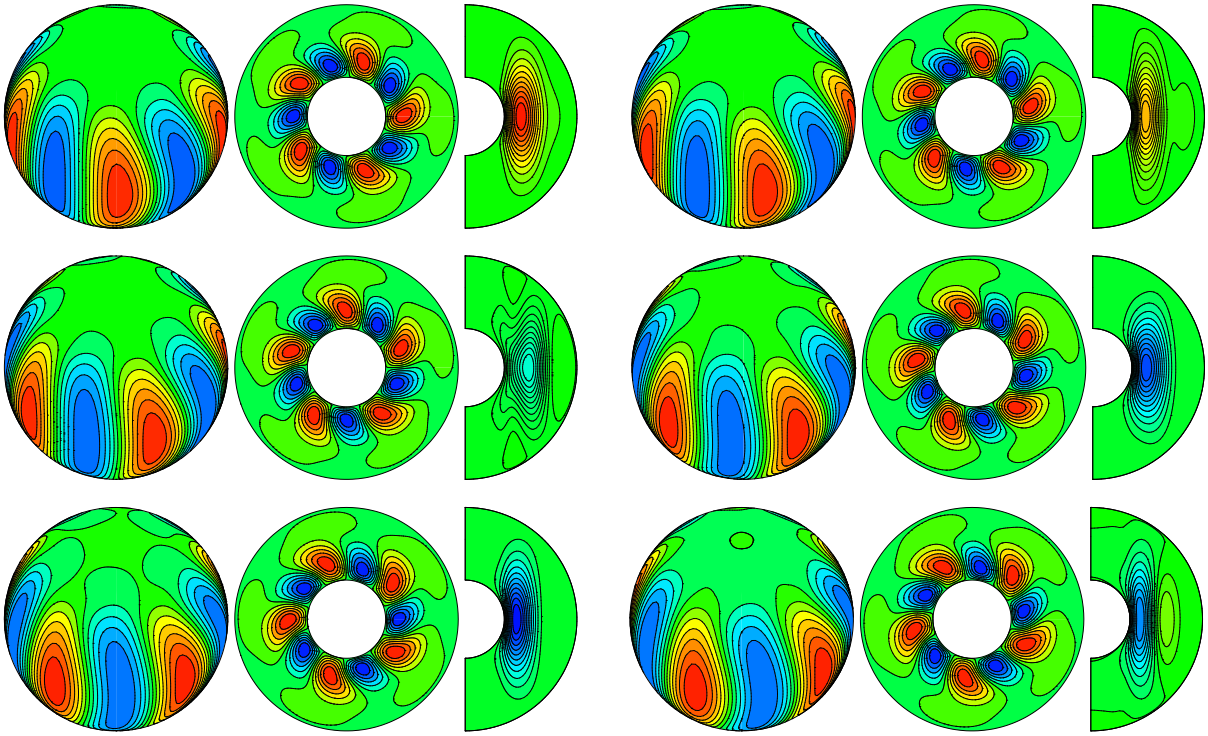

Figure 5.5: Same contour plots as in Fig. 5.4 for six snapshots corresponding nearly to a half period of an amplitude oscillation of an amplitude oscillating wave. From top to bottom, and from left to right, the snapshots are taken at $t = 0$, $t = 0.002$, $t = 0.004$, $t = 0.006$, $t = 0.008$, and $t = 0.01$. The Rayleigh number is $Ra = 2.78302 \times 10^5$.

To study in detail the different types of interactions between the neighbouring modes $m = 4, 5, 6$, the norm of the vector containing the amplitudes of the potentials and the temperature perturbation $||u_m||$ with $m = 6n$ (red), $m = 5n$ (green), and $m = 4n$ (blue), $n \in \mathbb{N}$, is plotted versus time in Figs. 5.6(a, c), and 5.7(a, c), for a selected set of solutions. Notice that in Fig. 5.6(a) $||u_4||$ and $||u_5||$ are not negligible because they contain the common multiples of 6 and 4, and 6 and 5, respectively, i.e, $||u_4|| = ||u_{12}||$ and $||u_5|| = ||u_{30}||$. In the other figures the $m = 6$ azimuthal symmetry is broken and consequently $||u_4||$ and $||u_5||$ contain other multiples. The norm $||u_m||$, with $m \neq 4n, 5n$ (red), $m \neq 4n, 6n$ (green), and $m \neq 5n, 6n$ (blue), is also plotted versus time in Figs. 5.6(b, d) and 5.7(b, d). Figs. 5.6(a, b) correspond to a $m = 6$ AOW at $Ra = 2.6 \times 10^5$, Figs. 5.6(c, d) and 5.7(a, b) to IAOW with preferred $m = 6$ azimuthal structure at $Ra = 2.61 \times 10^5$ and $Ra = 2.65 \times 10^5$, respectively, and finally, Figs. 5.7(c, d) to IAOW with preferred $m = 5$ azimuthal structure at $Ra = 2.875 \times 10^5$. In Fig. 5.8, the ratio of the norm of the vector containing the amplitudes of the potentials and the temperature perturbation with $m = 6n$, $n \in \mathbb{N}$ (red), with $m = 5n$ (green), and with $m = 4n$ (blue) to that containing

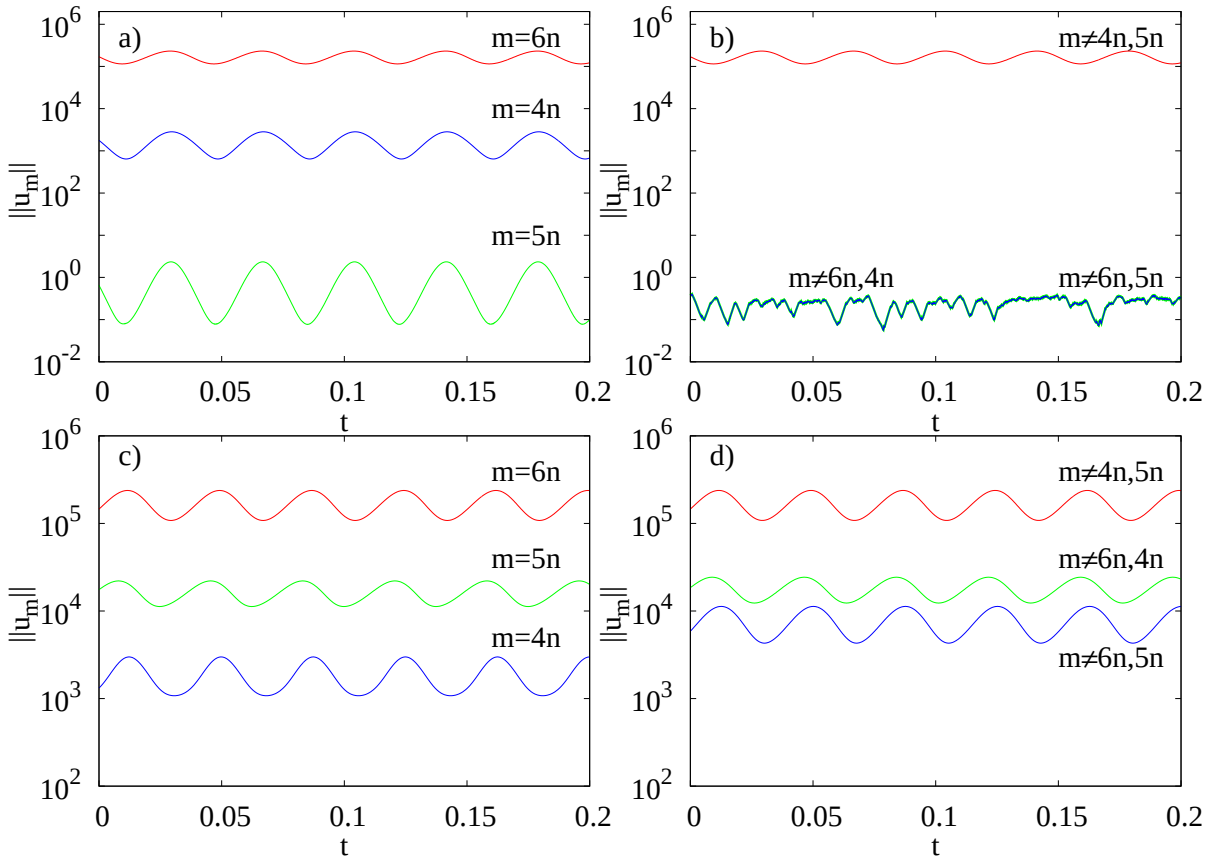

Figure 5.6: (a, c) Norms of the vectors of the amplitudes of the potentials and the temperature perturbation with $m = 6n$, $n \in \mathbb{N}$ (red), $m = 5n$ (green), and $m = 4n$ (blue), plotted versus time. (b, d) Same as (a, c) but with $m \neq 4n, 5n$ (red), $m \neq 6n, 4n$ (green), and $m \neq 6n, 5n$ (blue). The Rayleigh numbers are (a, b) $Ra = 2.6 \times 10^5$ (AOW), and (c, d) $Ra = 2.61 \times 10^5$ (IAOW).

all the amplitudes, is plotted versus time, for the four previous solutions.

In the AOW, one mode and their multiples of the expansion in spherical harmonics contribute to the solution. This is shown in Fig. 5.8(a), in which the norm $||u_6||$ retains more than 99% of the norm of the solution vector $||u||$. Notice that in Fig. 5.6(b) $||u_m||$ with $m \neq 6n, 4n$ and with $m \neq 6n, 5n$ are negligible. A consequence of having common multiples is that the sum of the ratios in Fig. 5.8 is slightly greater than 1.

Two different types of IAOW are found with preferred $m = 6$ azimuthal structure in a third Hopf bifurcation. The first one is shown in Figs 5.6(c, d), and 5.8(b), at $Ra = 2.61 \times 10^5$. For this solution the interactions are between the $m = 6$ and $m = 5$ modes. The norm $||u_6||$ retains more than 95% of the norm of the solution vector $||u||$, and the rest is supplied mainly by $||u_5||$ indicating that the modulation is weak. The fact

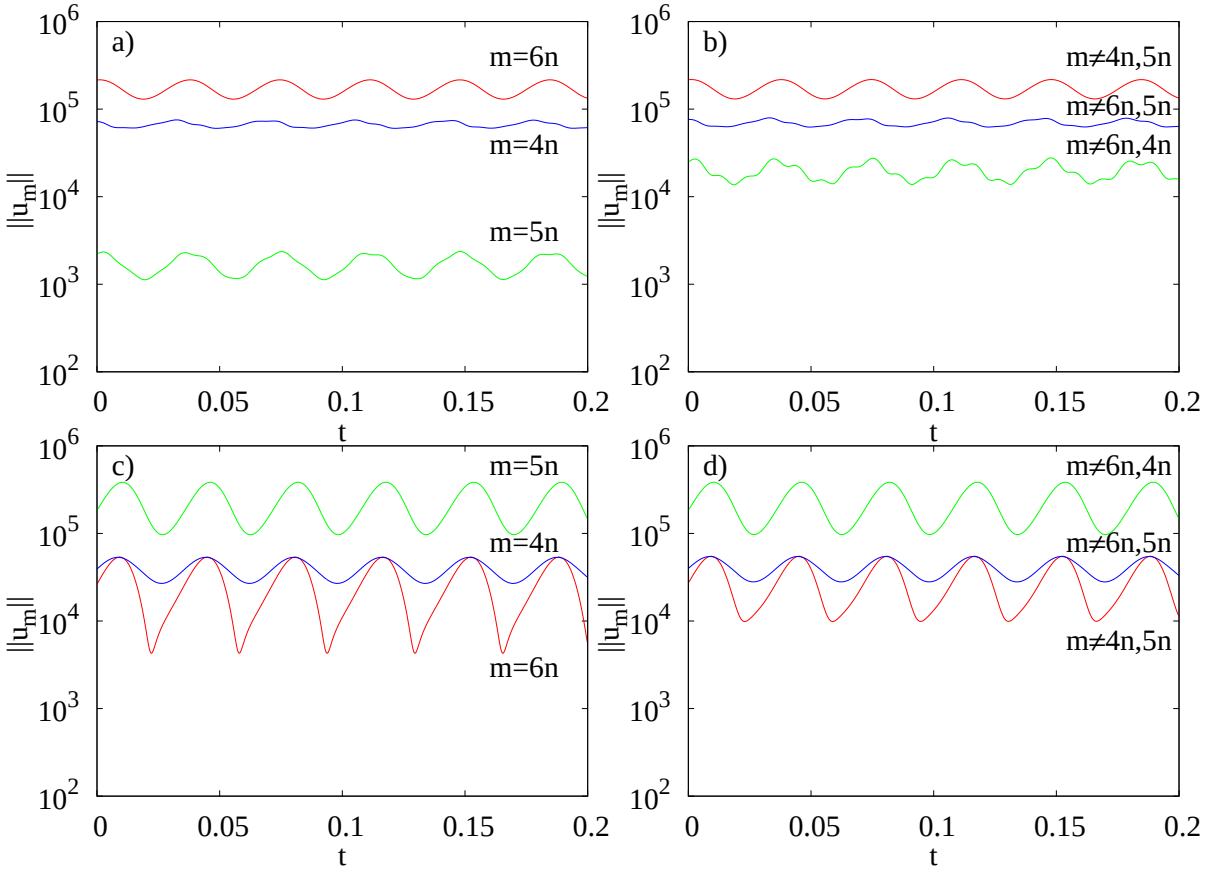

Figure 5.7: (a, c) Norms of the vectors of the amplitudes of the potentials and the temperature perturbation with $m = 6n$, $n \in \mathbb{N}$ (red), $m = 5n$ (green), and $m = 4n$ (blue), plotted versus time. (b, d) Same as (a, c) but with $m \neq 4n, 5n$ (red), $m \neq 6n, 4n$ (green), and $m \neq 6n, 5n$ (blue). The Rayleigh numbers are (a, b) $Ra = 2.65 \times 10^5$ (IAOW), and (c, d) $Ra = 2.875 \times 10^5$ (IAOW).

that $||u_4|| < ||u_m||$ with $m \neq 6n, 5n$ indicates that modes with $m \neq 6n, 5n, 4n$, grown also by the nonlinear interaction between $m = 6$ and $m = 5$, are nearly of the same order as $m = 4n$. The modes with $m \neq 6n, 5n$ contribute less than 1% to the total norm as shows Fig. 5.8(b).

In the second type of irregular oscillations shown in Figs 5.7(a, b), and 5.8(c), found at $Ra = 2.65 \times 10^5$, the interactions are between the $m = 6$ and $m = 4$ modes, which are stronger than the $m = 6, 5$ interactions, giving rise to $m = 2$ subharmonic patterns. Nevertheless $||u_6||$ still retains more than 90% of the norm of the solution vector $||u||$. We have checked that all the odd modes are zero by comparing this solution with one obtained by imposing the two-fold azimuthal symmetry.

Contrarily to the previous cases in which mainly two modes $m = 6, 5$ or $m = 6, 4$

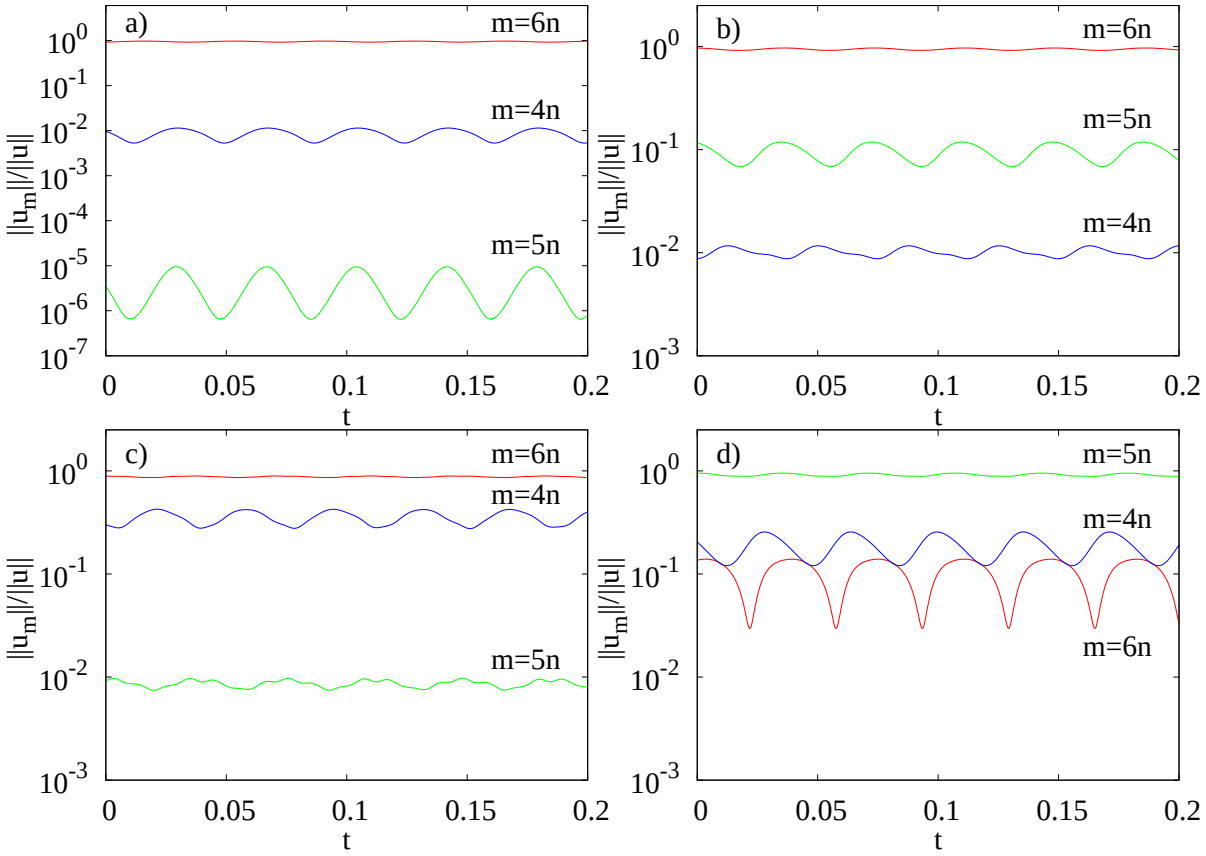

Figure 5.8: Ratios of the norms of the vectors of amplitudes of the potentials and the temperature perturbation with $m = 6n$, $n \in \mathbb{N}$ (red), with $m = 5n$ (green), and with $m = 4n$ (blue) to that containing all the amplitudes, plotted versus time. The Rayleigh numbers are (a) $Ra = 2.6 \times 10^5$, (b) $Ra = 2.61 \times 10^5$, (c) $Ra = 2.65 \times 10^5$, and (d) $Ra = 2.875 \times 10^5$.

contribute to the convection, the IAOW shown in Figs 5.7(c, d), and 5.8(d), at $Ra = 2.875 \times 10^5$, are generated by the interaction of the modes $m = 5, 4, 6$. In this case $||u_4||$, $||u_6||$ and $||u_m||$ with $m \neq 5n, 6n$, and with $m \neq 5n, 4n$, are nearly of the same order. The norm $||u_5||$ retains more than 95% of the norm of the solution vector $||u||$, indicating, as for $Ra = 2.61 \times 10^5$, that the modulations are weak. In contrast to the case of AOW, this $m = 5, 4, 6$ IAOW survive in a small interval of Rayleigh numbers.

Figures 5.9 and 5.10 show a sequence of snapshots of two IAOW illustrating the evolution of the amplitude of the cells. The left group of three columns contains the temperature perturbation and the right the kinetic energy density. The projections for Θ are the same as in Fig. 5.4, and for the kinetic energy density the spherical projections are taken close to the outer boundary, at $r = r_i + 0.975d$ with a polar point of view. The

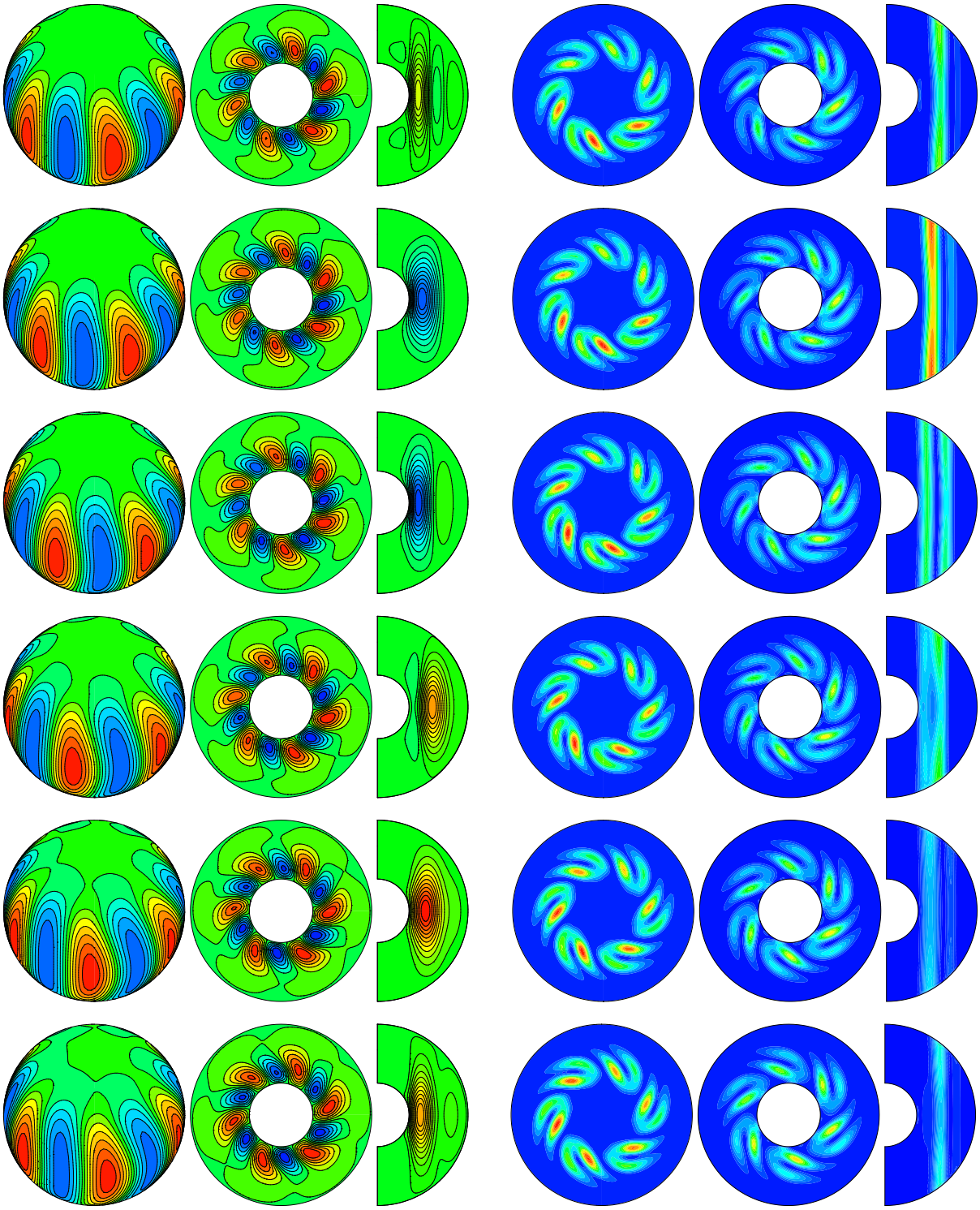

Figure 5.9: At left same contour plots as in Fig. 5.4 for six snapshots corresponding nearly to a half period of an amplitude oscillation of a $m = 6, 5$ IAOW, and at right contour plots of the kinetic energy density, on polar, equatorial and meridional projections. From top to bottom, the snapshots are taken at $t = 0$, $t = 0.003$, $t = 0.006$, $t = 0.009$, $t = 0.012$, and $t = 0.015$. The Rayleigh number is $Ra = 2.62 \times 10^5$.

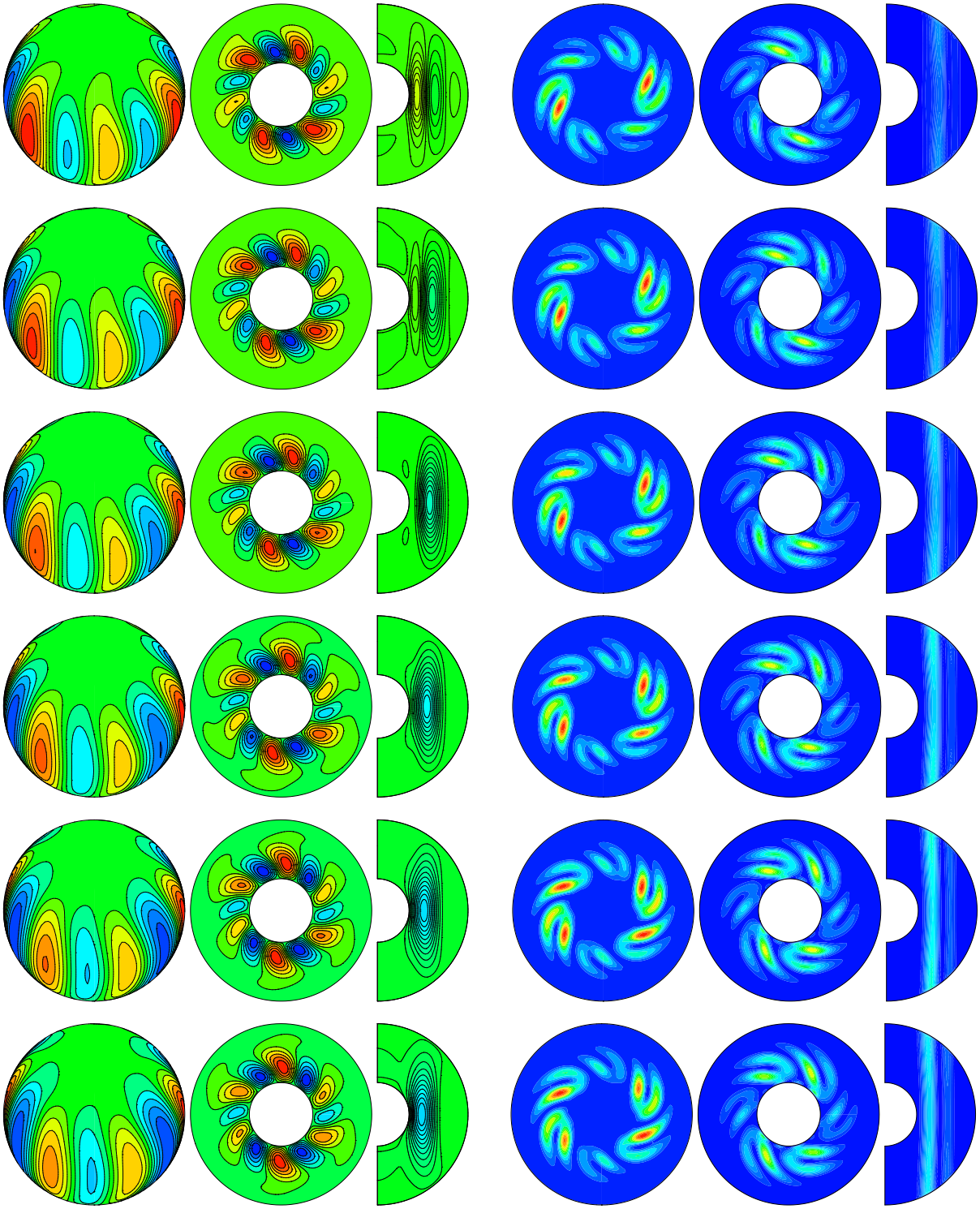

Figure 5.10: Same contour plots as in Fig. 5.9 for six snapshots corresponding to the evolution of the amplitude oscillation of a $m = 6, 4$ IAOW. From top to bottom, the snapshots are taken at $t = 0$, $t = 0.001$, $t = 0.002$, $t = 0.003$, $t = 0.004$, and $t = 0.005$. The Rayleigh number is $Ra = 2.65 \times 10^5$.

first figure corresponds to $Ra = 2.62 \times 10^5$ for a $m = 6, 5$ interaction, and the second to $Ra = 2.65 \times 10^5$ for a $m = 6, 4$ interaction as a sample of IAOW flows.

During a temporal evolution, the IAOW, in contrast to the AOW, involves a non-synchronous stretching and widening of the different convective cells. In the case of the interaction $m = 6, 4$, the flow is invariant under an azimuthal π-rotation (see Fig. 5.10). However, in the $m = 6, 5$ interaction no azimuthal symmetries are kept. Despite this fact almost the same physical pattern of convection is observed during the time evolution. If the convective columns $c_1, \ldots, c_6$, appearing in the spherical or equatorial sections of $\mathbf{v}^2$ in Fig. 5.9, are ordered by an increasing value of $\mathbf{v}^2$, namely if $\mathbf{v}^2_{c_1} > \mathbf{v}^2_{c_2} > \ldots > \mathbf{v}^2_{c_5} > \mathbf{v}^2_{c_6}$ then c_6 is diametrically opposed to c_1. The same holds for c_5 and c_2 and for c_4 and c_3.

As a consequence of the inhomogeneous pumping of the columns only some of them are connected simultaneously. Thus zonal circulations are less favoured (see Fig. 5.2(b)), then the drifting of the wave diminishes (see Fig. 5.1(a)) probably because the shear in the fluid is larger than in the AOW. In contrast to what happened to the AOW, the nonlinear interaction between modes of the IAOW favours the increasing of $\overline{Ro}$, $\overline{Ro_p}$ and $\overline{Nu}$ with Ra (see Fig. 5.2(a, c, d)), while the variance of the physical properties shown in Fig. 5.3 diminishes.

5.3.1.2 Dynamical description of the waves

A description of the travelling, amplitude oscillating, and irregular amplitude oscillating waves in terms of their frequency spectra and Poincaré sections is presented in this section. They are identified as periodic, two-frequency quasiperiodic and three-frequency quasiperiodic flows. As in Fig. 5.1(a), the frequency spectrum is obtained from the time series of the temperature perturbation Θ at the point $(r, \varphi, \theta) = (r_i + (r_o - r_i)/7, 0, 3\pi/8)$.

In Table 5.2 the independent frequencies f_1, f_2 and f_3 are listed for a selected set of solutions. The term independent means that the other frequencies f_i of the spectrum are $f_i = k_1 f_1 + k_2 f_2 + k_3 f_3$, with $k_1, k_2, k_3 \in \mathbb{Z}$. This has been checked for all the solutions studied (see Appendix A). It is worth noticing that f_1 always corresponds to the frequency of the drifting of the pattern, and f_2 is the frequency of the amplitude oscillations. Although f_1 is always the frequency of largest amplitude given by the Laskar's algorithm, f_2 is never the second. Notice that Table 5.2 contains frequencies corresponding to different branches of solutions.

The AOW, with two independent frequencies f_1 and f_2, is an orbit in the phase space which lies on a two dimensional torus. If the frequencies satisfy the relation $f_2/f_1 = R = p/q$, $R \in \mathbb{Q}$ the orbit closes, and the flow is periodic (resonant). Otherwise the orbit fills the whole torus and the flow is quasiperiodic. The latter case is represented by a closed curve on a surface determined by a Poincaré section, and the former by a set of q points. In the two branches $m = 6$ and $m = 5$ of invariant 2-tori the rotation number R has been computed from Table 5.2 as a function of Ra. A periodic solution of $R = 4/9$, and a nearly periodic solution of $R \approx 4/9$, respectively, are identified. The procedure used to

Branch	Ra	Ra/Ra_c	f_1	f_2	f_3
	2.5×10^5	1.347	61.749		
	2.52×10^5	1.358	61.301		
	2.55×10^5	1.374	60.634		
	2.58×10^5	1.39	59.973	27.356	
	2.59×10^5	1.395	59.999	27.181	
$m = 6$	2.6×10^5	1.4015	60.237	26.727	
	2.61×10^5	1.406	60.184	26.634	0.456
	2.61337×10^5	1.408	60.083	26.703	0.614
	2.62×10^5	1.412	59.890	26.838	1.748
	2.63×10^5	1.417	59.502	26.861	3.044
	2.65×10^5	1.428	58.727	27.263	4.202
	2.67×10^5	1.439	62.608		
	2.725×10^5	1.468	61.751		
	2.75×10^5	1.482	61.770	28.168	
$m = 5$	2.8×10^5	1.509	62.856	27.606	
	2.85×10^5	1.536	63.998	27.572	
	2.875×10^5	1.549	64.274	27.926	1.819
	2.91×10^5	1.562	64.285	28.689	1.577

Table 5.2: The three independent frequencies of the time series of the temperature perturbation Θ at the point $(r, \varphi, \theta) = (r_i + (r_o - r_i)/7, 0, 3\pi/8)$.

find resonant motions is outlined in the Appendix A.

In Fig. 5.11(a) the plots of the Poincaré section at $\Theta(r_i + (r_o - r_i)/7, 0, 3\pi/8) = 0$ of the azimuthal component of the velocity field $\mathbf{v}_\varphi((r_i + r_o)/2, 0, 3\pi/8)$ versus Θ at the same point are shown. They correspond to an $m = 6$ AOW. In this figure the set of 9 points corresponding to the resonance $R = 4/9$ can be identified, and also three closed curves corresponding to the quasiperiodic AOW. The same is shown in Fig. 5.11(b) but for the $m = 5$ AOW. The solution close to resonance can also be appreciated.

In Figs. 5.12 and 5.13 the frequency spectra for a selected set of solutions are shown. The former corresponds to solutions on the $m = 6$ branch and the latter to solutions on the $m = 5$ branch. Looking at both figures the growing of f_2, f_3 and the dependent frequencies can be clearly identified. Figure 5.12(a) shows the typical spectrum of a travelling wave at low $Ra = 2.52 \times 10^5$. At somewhat higher $Ra = 2.58 \times 10^5$ (Fig. 5.12(b)) a small peak, corresponding to f_2, appears. For $Ra = 2.59 \times 10^5$ the spectrum displays f_1 and f_2 together with their combinations $n_1 f_1 + n_2 f_2$, $n_1, n_2 \in \mathbb{Z}$ (see Fig. 5.12(c) and its detail (d)). Finally at higher Ra, f_3 is born being substantially lower than f_1 or f_2 (see Figs. 5.12(e) and (f)). In these figures the labels which contain the term kf_3 mean that

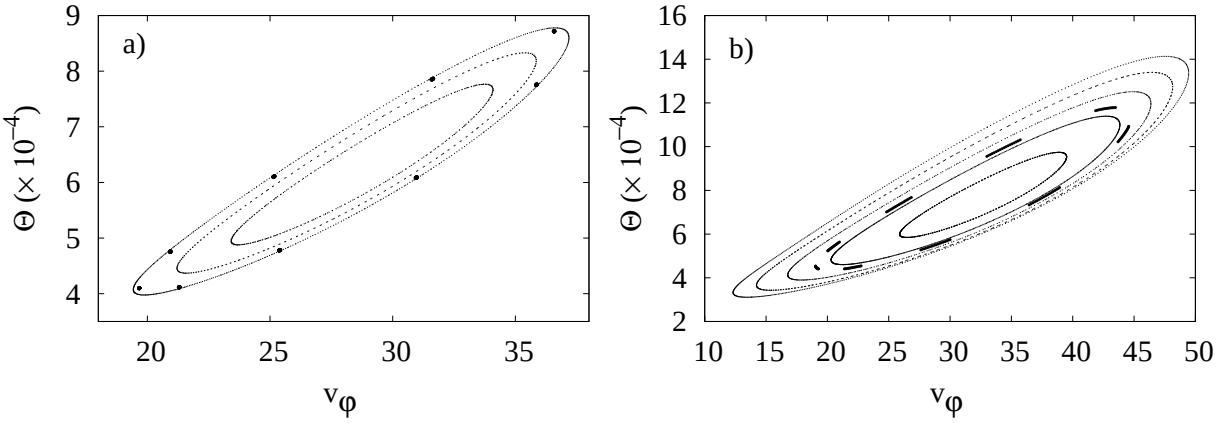

Figure 5.11: (a) Poincaré section at $\Theta(r_i + (r_o - r_i)/7, 0, 3\pi/8) = 0$ of the azimuthal component of the velocity field $\mathbf{v}_\varphi((r_i + r_o)/2, 0, 3\pi/8)$, plotted versus Θ at the same point. The Rayleigh numbers from the inner to the outer sections are $Ra = 2.59 \times 10^5$, $Ra = 2.595 \times 10^5$, $Ra = 2.59929964 \times 10^5$ and $Ra = 2.6 \times 10^5$. (b) Same as in (a), but for $Ra = 2.75 \times 10^5$, $Ra = 2.775 \times 10^5$, $Ra = 2.78302 \times 10^5$, $Ra = 2.8 \times 10^5$, $Ra = 2.825 \times 10^5$ and $Ra = 2.85 \times 10^5$.

the value of the frequency of each peak in the group and its neighbours are obtained by substituting k by some integer. A similar behaviour as in Fig. 5.12 is observed in Fig. 5.13 for the $m = 5$ branch. Notice that for the $m = 5$ IAOW there are more peaks involving f_3 (see Figs. 5.13(e, f)), probably indicating that the ratio Ra/Ra_c^3 for this type of IAOW is higher than for the IAOW of the $m = 6$ branch, with Ra_c^3 meaning the Rayleigh number of the bifurcation where f_3 is born.

When IAOW solutions start to appear, the closed curve of the Poincaré section corresponding to the AOW starts to expand, and becomes a band. The same representation as in Fig. 5.11 is shown in Fig. 5.14, but for several IAOW. They are quasiperiodic solutions with three independent frequencies as their frequency spectra show, Figs. 5.12 and 5.13 and Table 5.2.

There is a noticeable difference between the Poincaré sections of the $m = 6, 5$ IAOW (Fig. 5.14(a)), and that of the $m = 6, 4$ IAOW (Fig. 5.14(b)), indicating that they come from different branches of invariant tori. It can also be seen in the contour plots of Figs 5.9 and 5.10, where the $m = 6$ azimuthal pattern remains nearly unaltered in the $m = 6, 5$ solutions. Figure 5.14(c) corresponds to a $m = 5, 4, 6$ IAOW bifurcated from the $m = 5$ AOW, and resembles that of the $m = 6, 5$ IAOW, but in this case the tori is nearly resonant as it is indicated by the small continuous segments of points. Again, depending on the value of Ra, the ratio of two of the three frequencies f_1, f_2, and f_3 could be rational. For instance if $R = f_2/f_1 = p/q$ the Poincaré section becomes a set of

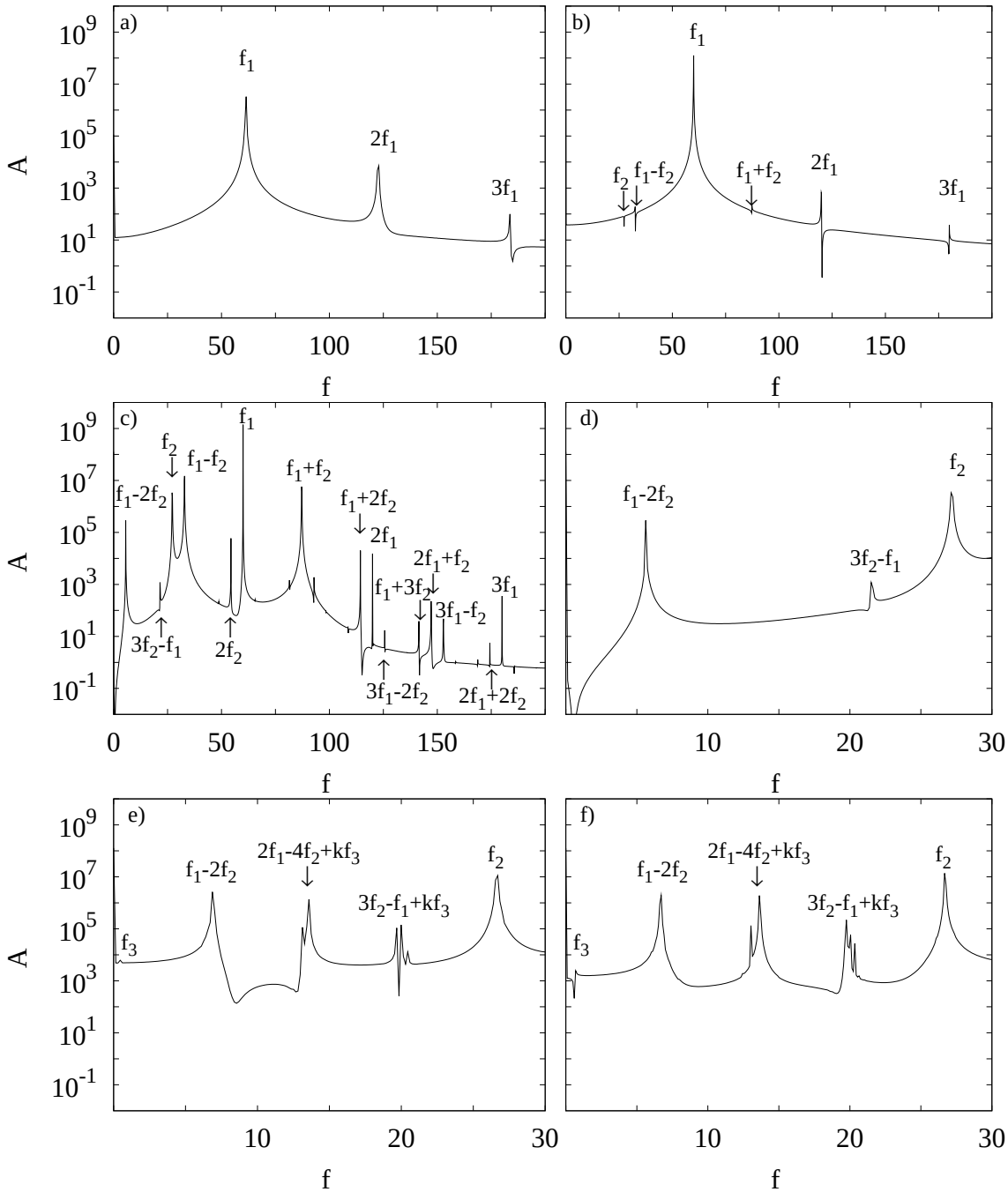

Figure 5.12: Frequency spectrum of the time series of $\Theta(r_i + (r_o - r_i)/7, 0, 3\pi/8)$. (a) $Ra = 2.52 \times 10^5$, (b) $Ra = 2.58 \times 10^5$, (c) $Ra = 2.59 \times 10^5$, (d) detail of (c) for the very low frequencies, (e) $Ra = 2.61 \times 10^5$, and (f) $Ra = 2.61337 \times 10^5$.

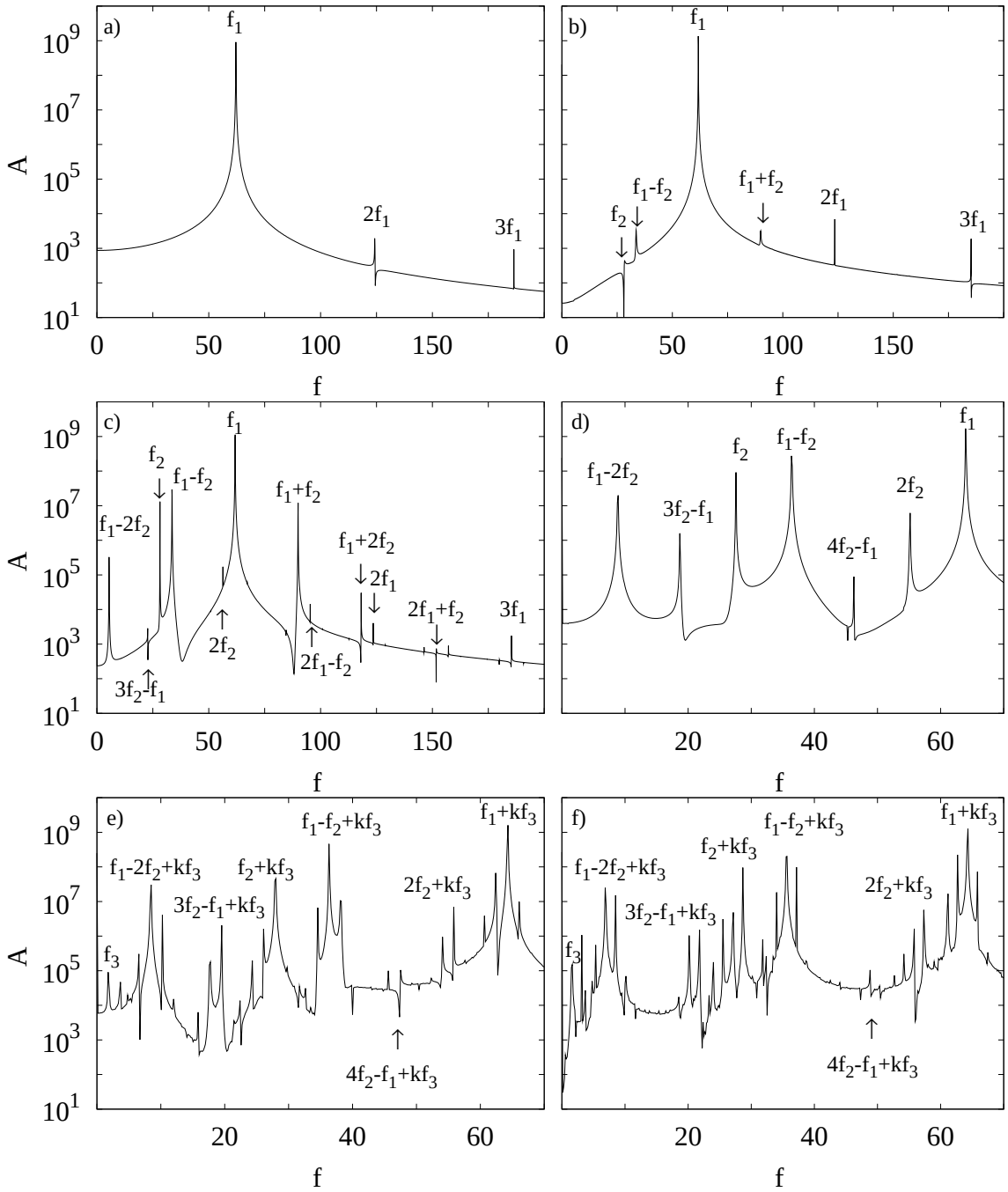

Figure 5.13: Frequency spectrum of the time series of $\Theta(r_i + (r_o - r_i)/7, 0, 3\pi/8)$. (a) $Ra = 2.7 \times 10^5$, (b) $Ra = 2.725 \times 10^5$, (c) $Ra = 2.75 \times 10^5$, (d) $Ra = 2.85 \times 10^5$, (e) $Ra = 2.875 \times 10^5$, and (f) $Ra = 2.91 \times 10^5$.

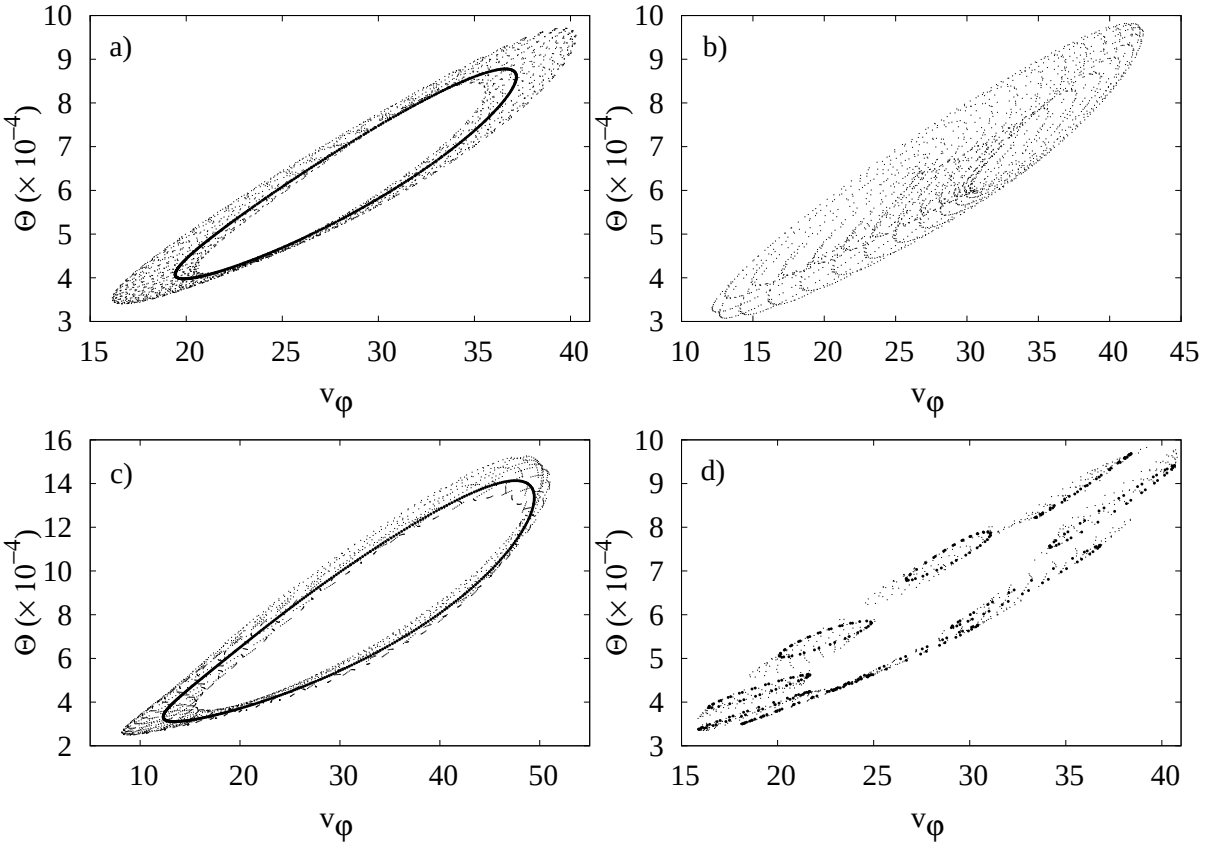

Figure 5.14: (a-d) Poincaré sections as in Fig. 5.11. (a) $Ra = 2.6 \times 10^5$ (closed curve) and $Ra = 2.61 \times 10^5$ (band). (b) $Ra = 2.65 \times 10^5$ (band). (c) $Ra = 2.75 \times 10^5$ (closed curve) and $Ra = 2.875 \times 10^5$ (band). (d) $Ra = 2.61337 \times 10^5$ (set of 9 rings), and $Ra = 2.61347 \times 10^5$ (band).

q closed curves on the surface. This is shown in Fig. 5.14(d), again for $R = f_2/f_1 = 4/9$. This figure also shows a section of a nearly resonant orbit $R = f_2/f_1 \approx 4/9$.

Notice that for all the AOW, with frequencies f_1 and f_2, the time series of the global properties, such as the kinetic energy density or the zonal flow, are periodic functions of frequency f_2 (see Table 5.2). For the IAOW the volume-averaged properties have two frequencies, although the second is very weak. The frequency f_2 does not vary a lot with the Rayleigh number, as can be seen in the frequency spectra shown before and in Table 5.2. This result differs from that obtained for the shape vacillating convection studied in [106] with stress-free boundary conditions and similar parameters (see for instance their Fig. 4).

5.3.2 Transition between the $m = 5$ and $m = 4$ branches: Connecting orbits

Taking as initial condition a $m = 5$ IAOW and increasing slightly the Rayleigh number beyond $Ra = 2.91 \times 10^5$ (see second vertical line of Fig. 5.1(a)) the temporal evolution leads to a set of solutions with chaotic complex time dependence, but which share certain regularity in the patterns of convection. For these type of solutions the azimuthal symmetry is broken, with only the modes $m = 5$ and $m = 4$ playing an important role.

In Fig. 5.15 the norm of the vector of the amplitudes of the potentials and the temperature perturbation with $m = 4n$, $n \in \mathbb{N}$ (red), $m = 5n$ (green) and $m \neq 4n, 5n$ (blue), is plotted versus time for an increasing sequence of Rayleigh numbers, $Ra \in [2.91 \times 10^5, 3.33 \times 10^5]$. When Ra is increased the norm of the $m = 4$ mode increases while the $m \neq 4n, 5n$ modes remain with small amplitude. In some figures (e-i) an intermittence can be clearly distinguished with intervals in which the norm of the $m = 4n$ modes is almost constant, and the norm of the other modes $m \neq 4n$ nearly vanishes, and intervals in which the norm of the $m = 5n$ modes oscillate reaching its maximum value, while the norm of the other $m \neq 5n$ modes nearly vanishes. This implies a change between the $m = 4$ and $m = 5$ azimuthal symmetry. In the range $Ra \in [2.99 \times 10^5, 3.075 \times 10^5]$ this change takes place in an almost periodic way.

In Fig. 5.16 the frequency spectra of the temperature perturbation, corresponding to the solutions of Fig. 5.15, are displayed. Despite the complex time dependence of the solutions, their spectra roughly remind those of the solutions found before $Ra = 2.91 \times 10^5$. For instance, the profile, and the position of the tallest peak which is located near $f = 60$, and indicates that the drift of the pattern is maintained.

In order to understand what is going on at $Ra = 3 \times 10^5$, the unstable solutions with imposed two- and five-fold azimuthal symmetry were also computed. They are a $m = 4$ travelling wave (see Fig. 5.1(b)), and a $m = 5$ AOW. By perturbing these unstable solutions with randomly small perturbations, an orbit which almost connect them is obtained suggesting that this behaviour could be related with an existence of a heteroclinic chain as occurs in [28, 27]. In Fig. 5.17, some plots are shown to give some support to this idea. In Fig. 5.17(a) a detail of the same norms displayed in Fig. 5.15 are shown for $Ra = 3 \times 10^5$. The detail shows two peaks of the residual modes $m \neq 4n, 5n$, which appear just when the norms of the modes $m = 4n$ and $m = 5n$ become comparable. These are the time instants at which the stable heteroclinic chain changes from an unstable orbit to the other. Notice that it spends more time close to the unstable $m = 4$ orbit, so its time-averaged properties are closer to those of the orbit, and the same occurs for the first fundamental frequency (compare the linear behaviour of the curves in Figs. 5.1(a, b) in the range $Ra \in [3 \times 10^5, 3.2 \times 10^5]$).

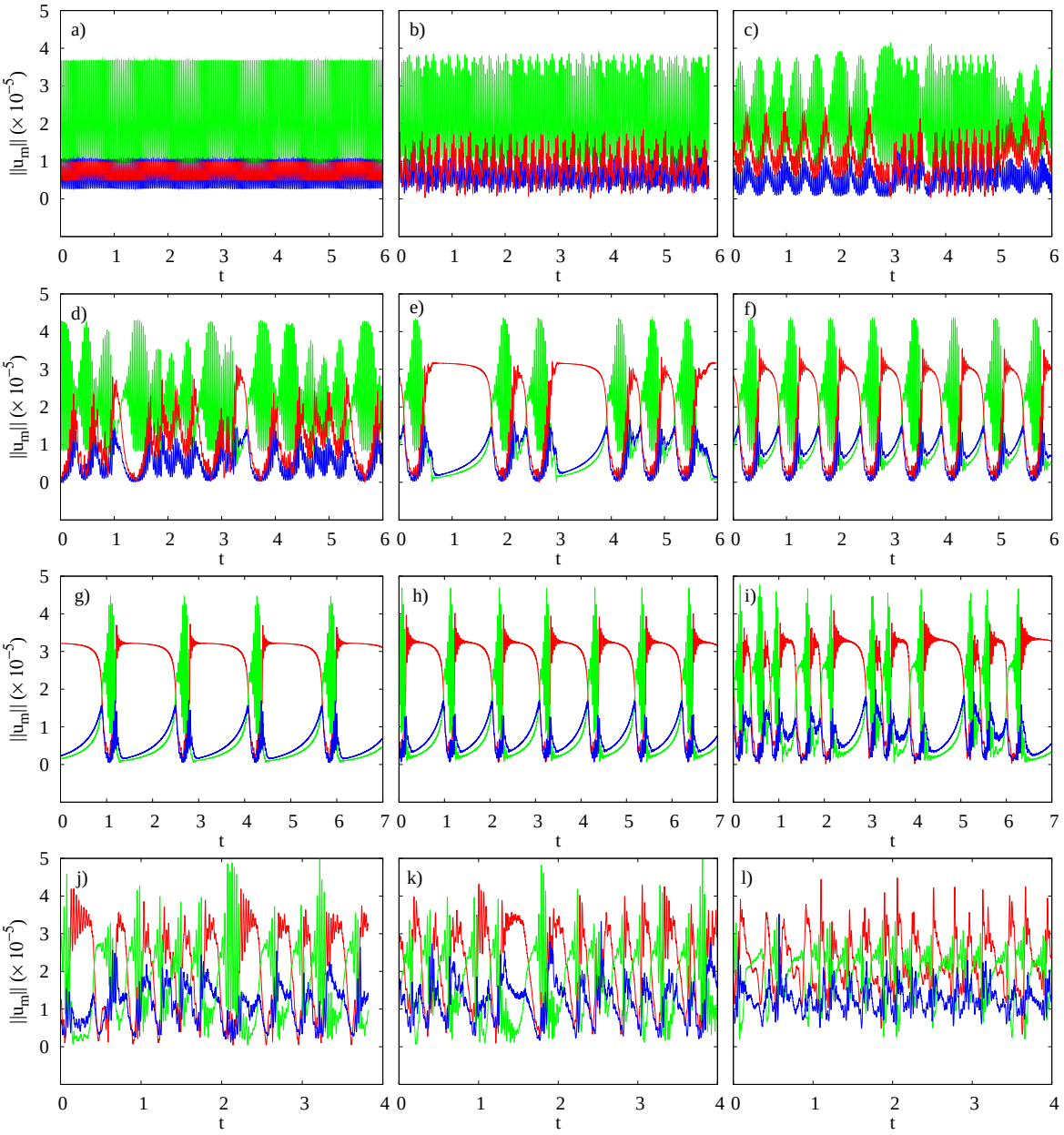

Figure 5.15: Norms of the vectors of the amplitudes of the potentials and the temperature perturbation with $m = 4n$, $n \in \mathbb{N}$ (red), with $m = 5n$ (green), and with $m \neq 4n, 5n$ (blue), plotted versus time. The Rayleigh numbers are (a) $Ra = 2.91 \times 10^5$, (b) $Ra = 2.93 \times 10^5$, (c) $Ra = 2.94 \times 10^5$, (d) $Ra = 2.96 \times 10^5$, (e) $Ra = 2.98 \times 10^5$, (f) $Ra = 2.99 \times 10^5$, (g) $Ra = 3.025 \times 10^5$, (h) $Ra = 3.075 \times 10^5$, (i) $Ra = 3.125 \times 10^5$, (j) $Ra = 3.22 \times 10^5$, (k) $Ra = 3.27 \times 10^5$, and (l) $Ra = 3.33 \times 10^5$.

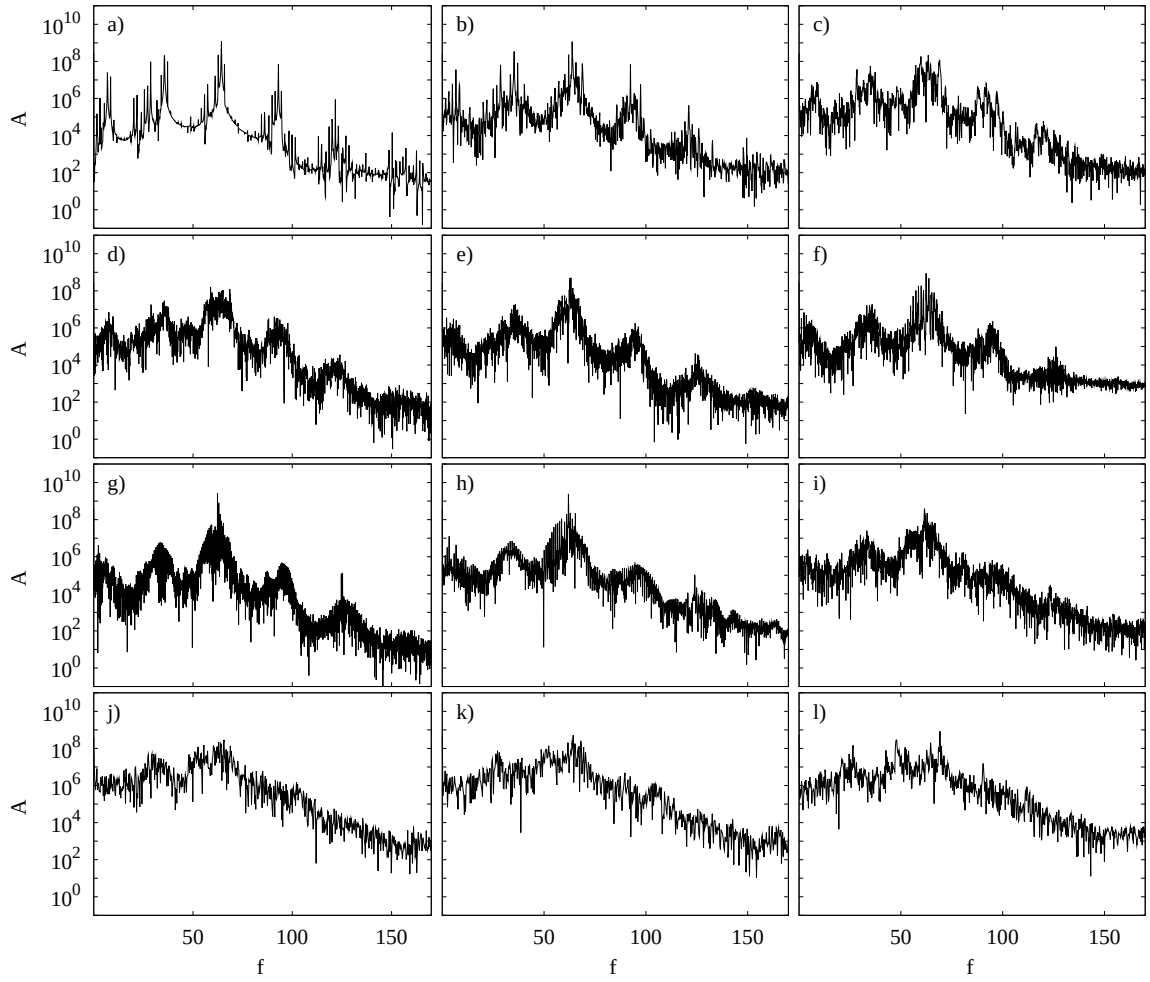

Figure 5.16: (a-l) Frequency spectra of the time series of $\Theta(r, \varphi, \theta) = (r_i + (r_o - r_i)/7, 0, 3\pi/8)$. The parameters are as in Fig. 5.15.

In Fig. 5.17(b) same Poincaré sections as in Fig. 5.11 are shown for the two unstable and the stable orbits. The red point corresponds to the unstable $m = 4$ periodic orbit and the green curve to the unstable $m = 5$ 2-torus. In blue the points of the stable orbit are represented. They are highly concentrated near the red point meaning that the stable orbit spends most time near the periodic orbit. Some of them also lie near the closed curve of the torus. The points near the origin correspond to the transition between the periodic orbit and the torus because the norm of the amplitudes is minimal.

Finally, in Figs. 5.17(c, d), the ratio of the total to the non-zonal kinetic energy densities, plotted versus time is shown. In the latter the ratios for the unstable orbits are also included. As expected, the ratio for the stable orbit is, intermittently, nearly constant close to that of the $m = 4$ unstable orbit, and it is strongly oscillatory as that

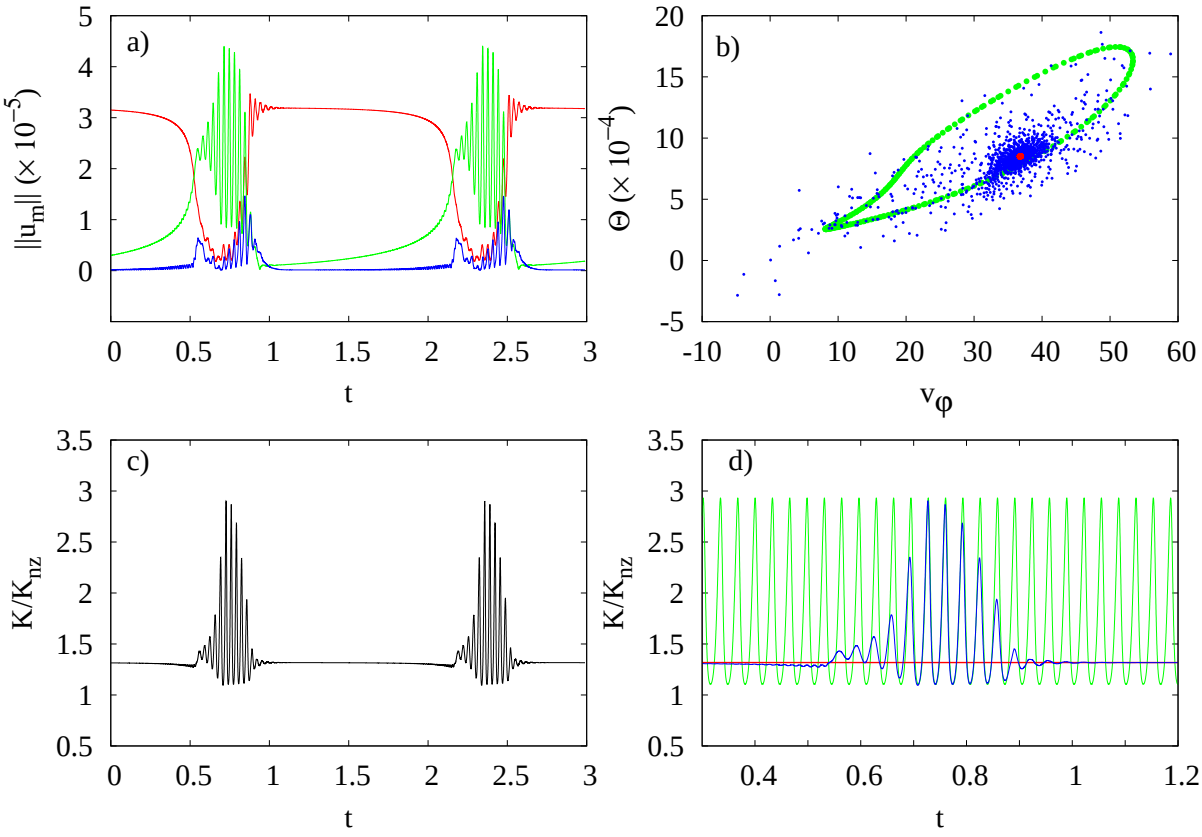

Figure 5.17: (a) Norms of the vectors of the amplitudes of the potentials and the temperature perturbation with $m = 4n$, $n \in \mathbb{N}$ (red), $m = 5n$ (green), and $m \neq 4n, 5n$ (blue), plotted versus time. (b) Poincaré sections as in Fig. 5.11. The colours mean: unstable $m = 4$ periodic orbit (red), unstable $m = 5$ 2-torus (green), and the stable heteroclinic chain (blue). (c) Ratio of the total to the non-zonal kinetic energy densities, plotted versus time. (d) In blue detail of (c), including also the energy ratios of the unstable $m = 4$ periodic orbit (red) and the unstable $m = 5$ 2-torus (green). The Rayleigh number is $Ra = 3.0 \times 10^5$.

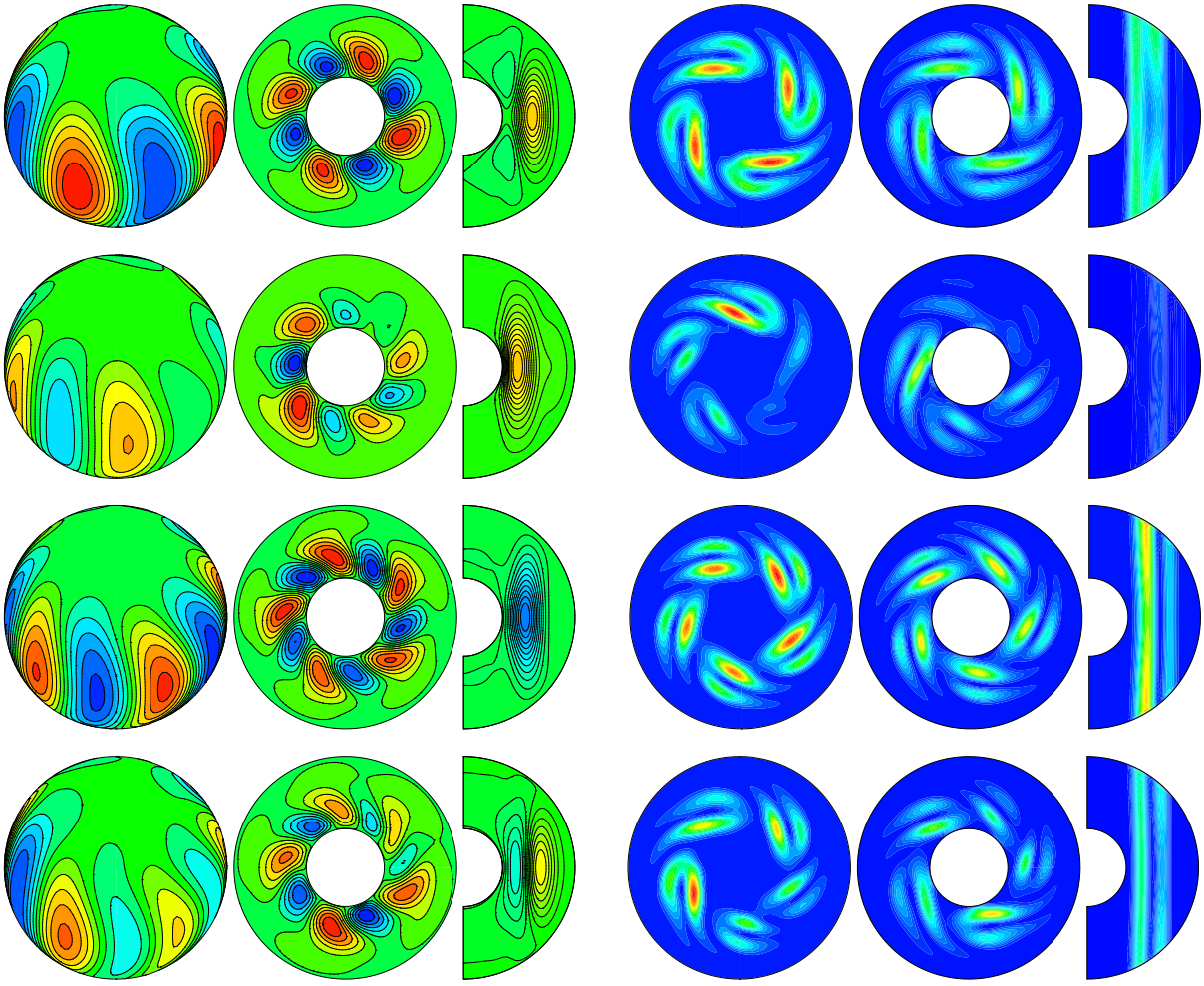

Figure 5.18: Same contour plots as in Fig. 5.9 for four snapshots at different stages in the evolution of the heteroclinic chain. From top to bottom, the snapshots are taken when the orbit is close to the unstable $m = 4$ periodic orbit, when the orbit is approaching the unstable $m = 5$ 2-torus (when $||u_4|| \approx ||u_5||$, and $||u_4|| \to 0$), when the orbit is close to the unstable $m = 5$ 2-torus, and finally when the orbit is approaching again the unstable $m = 4$ periodic orbit (when $||u_5|| \approx ||u_4||$ and $||u_5|| \to 0$). The Rayleigh number is $Ra = 3.025 \times 10^5$.

of the $m = 5$ unstable orbit. In the oscillatory interval strong zonal circulations carrying about 65% of the kinetic energy density are generated due to the connection of the amplitude oscillating columns as it has been described in the previous section. This type of intermittent behaviour of the physical properties is very similar to the one described in [29], with stress-free boundary conditions and $\sigma = 1$, at intermediate Ra numbers.

As Ra increases far away from $Ra = 2.91 \times 10^5$ in the chaotic region, the time-averaged

physical properties vary randomly, but as can be observed in Fig. 5.2 they increase in the whole range. The relative variance of the physical properties is smaller than that of the quasiperiodic motion at lower Ra. The first fundamental frequency f_1 shown in Fig. 5.1(a) varies sharply if $Ra < 3 \times 10^5$ or $Ra > 3.2 \times 10^5$, but decreases smoothly if $Ra \in [3 \times 10^5, 3.2 \times 10^5]$. These features can be explained by the fact that most of the solutions spend most of the time close to the unstable $m = 4$ travelling wave, and thus the time dependence of the physical properties, their variances, and the fundamental frequency are similar to that of a travelling wave.

Finally, in order to visualise the patterns of convection, the same contour plots as in Fig. 5.9, are shown in Fig. 5.18, but at $Ra = 3.025 \times 10^5$ for a heteroclinic chain. The first row corresponds to a snapshot taken when the orbit is close to the unstable $m = 4$ periodic orbit. The second row is a snapshot taken when the orbit is approaching the unstable $m = 5$ 2-torus, when $||u_4|| \approx ||u_5||$, and $||u_4|| \to 0$. In the third row the snapshot is taken when the orbit is close to the unstable $m = 5$ 2-torus. Finally, in the fourth row the snapshot is taken when the orbit is approaching again the unstable $m = 4$ periodic orbit, when $||u_5|| \approx ||u_4||$ and $||u_5|| \to 0$. Notice that in the second row of the figure, one of the four cold cells is being divided in two cold cells, and in the fourth row of the figure, two of the five hot cells are connected and merging into one, while one the cold cells in the middle is disappearing.

5.3.3 $m = 4$ branch of solutions

At about $Ra = 3.43 \times 10^5$, beyond the region of the orbits close to heteroclinic chains, a window of quasiperiodic motion appears up to $Ra = 3.9 \times 10^5$ (see Fig. 5.1(a)). All the solutions computed in this window have a dominant $m = 4$ mode. This is shown, for a set of four solutions, in Figs. 5.19, and 5.20, where the norm $||u_m||$, and the ratio $||u_m||/||u||$, with $m = 6n$, $n \in \mathbb{N}$ (red), $m = 5n$ (green), and $m = 4n$ (blue), is plotted versus time. In this case there is a stronger competition between the modes than in the quasiperiodic $m = 6$ or $m = 5$ branches of solutions (compare Figs. 5.20 and 5.8). Thus more pronounced differences are expected between the cells. Now, the norm of the non-dominant modes $m = 5n$ or $m = 6n$ contribute at least a 20% of the total norm (see Fig. 5.20). Moreover, Fig. 5.19 shows very small temporal scale variations.

An analysis performed using the largest-amplitude independent frequencies given by the Laskar's algorithm allows to identify two and three-frequency quasiperiodic and resonant motions in both cases. An exhaustive analysis must be performed in order to identify the physical meaning of the frequencies, and the origin of the quasiperiodic window. However only the dynamic behaviour of the solutions will be depicted in this section, and the analysis will be undertaken in a near future.

Poincaré sections similar to those of Fig. 5.11, are shown in Fig. 5.21, as examples of three-frequency solutions ($Ra = 3.47 \times 10^5$ and $Ra = 3.55 \times 10^5$), a resonant two-frequency solution ($Ra = 3.5038741 \times 10^5$), and a two-frequency solution ($Ra = 3.53 \times 10^5$). The

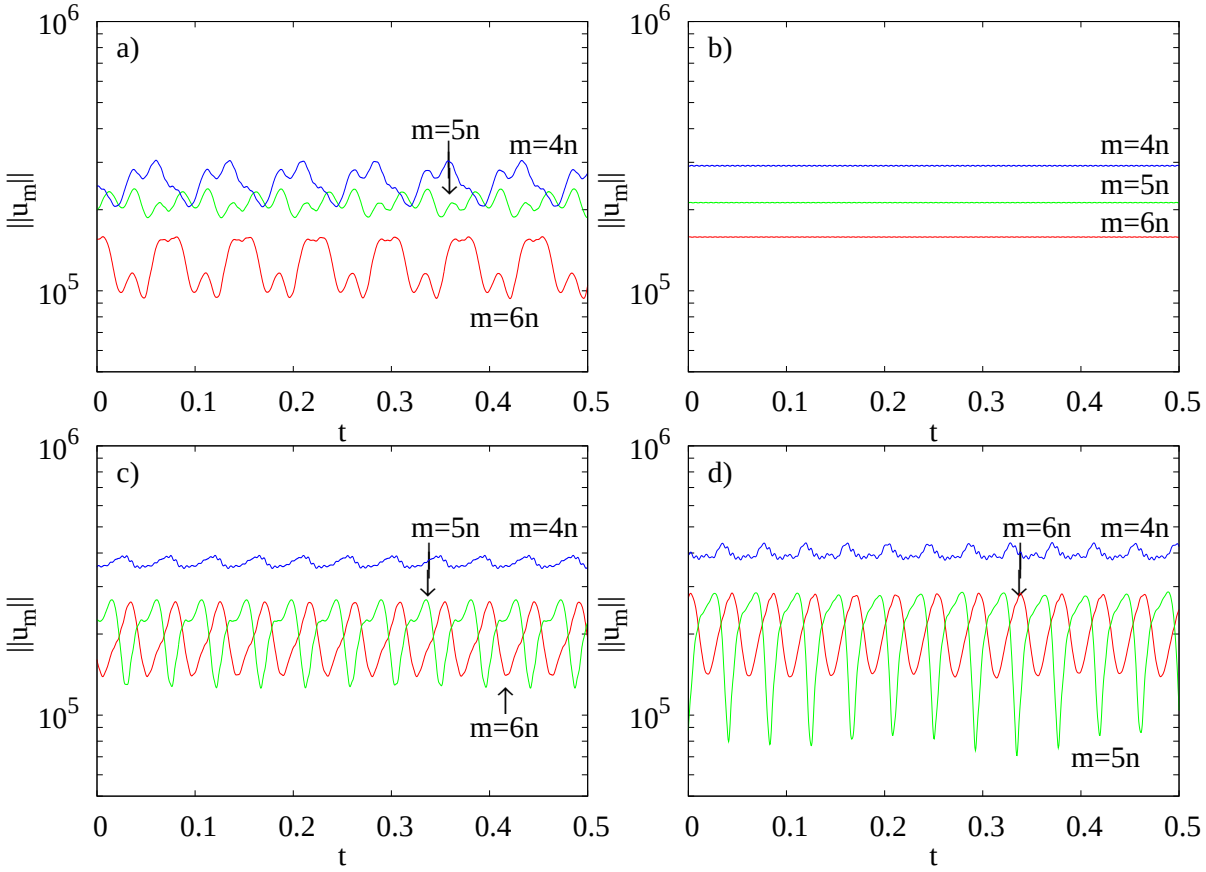

Figure 5.19: (a-d) Norms of the vectors of the amplitudes of the potentials and the temperature perturbation with $m = 6n$, $n \in \mathbb{N}$ (red), $m = 5n$ (green), and $m = 4n$ (blue), plotted versus time. The Rayleigh numbers are (a) $Ra = 3.43 \times 10^5$, (b) $Ra = 3.53 \times 10^5$, (c) $Ra = 3.75 \times 10^5$, and (d) $Ra = 3.88 \times 10^5$.

corresponding frequency spectra are shown in the same figure (right column). They clearly exhibit the quasiperiodic behaviour of the solutions. The degree of complexity of the spectra denotes the richness in spherical harmonics of the tori. Notice that contrarily to the flows of the $m = 6$ or $m = 5$ solutions (Figs. 5.11 or 5.14), two intersections on the Poincaré section are shown in Fig. 5.21. We have proceed in this way because the hypersurface $\Theta(r_i + (r_o - r_i)/7, 0, 3\pi/8) = 0$ cuts the 2-tori in such a way that it gives an unclosed curve if only one change of sign is taken into account.

Other examples of these complex quasiperiodic motions are given in Fig. 5.22, where similar Poincaré sections as in Fig. 5.21 are shown. They are examples of three-frequency solutions ($Ra = 3.56 \times 10^5$ and $Ra = 3.680827 \times 10^5$), of a nearly resonant three-frequency solution ($Ra = 3.681303 \times 10^5$), and of a resonant three-frequency solution ($Ra = 3.73 \times 10^5$). Notice that different types of Poincaré sections corresponds to different types of

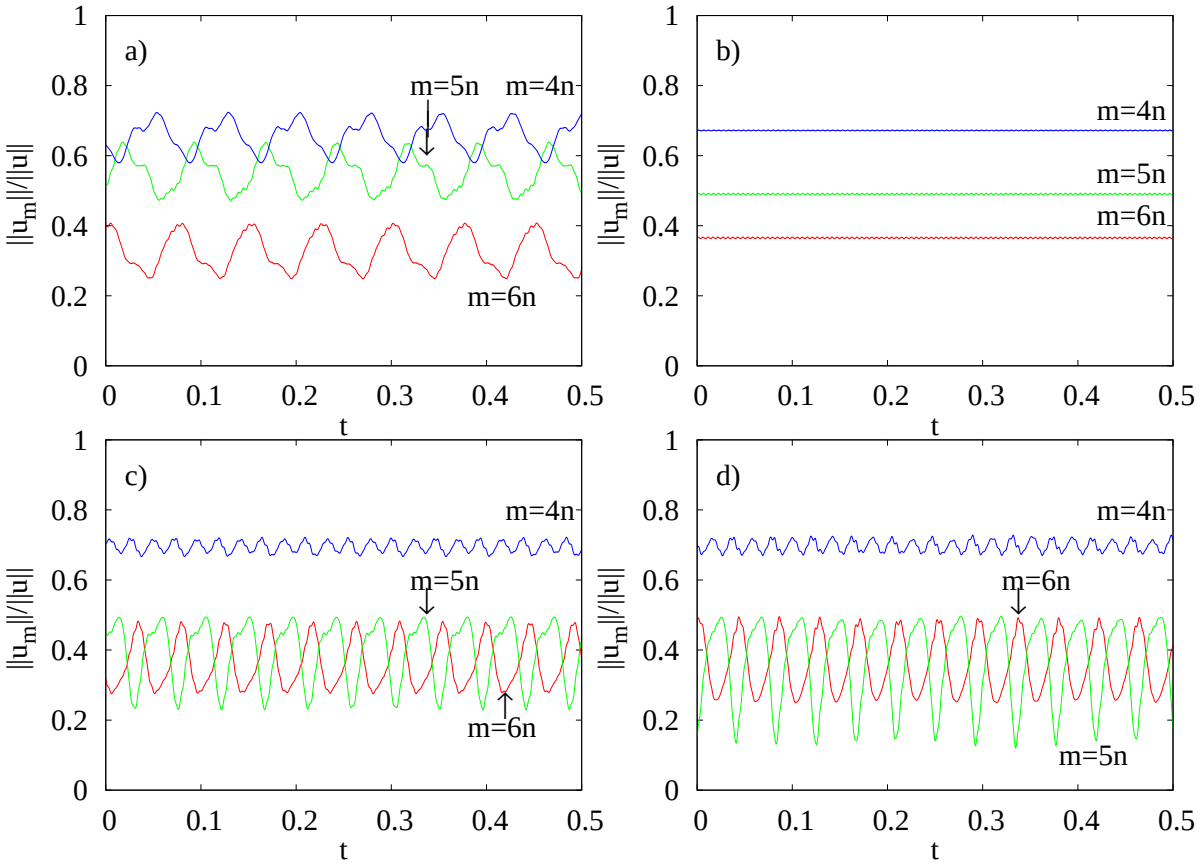

Figure 5.20: Ratios of the norms of the vectors of the amplitudes of the potentials and the temperature perturbation with $m = 6n$, $n \in \mathbb{N}$ (red), $m = 5n$ (green), and $m = 4n$ (blue) to the norm of the vector of all the amplitudes, plotted versus time. The Rayleigh numbers are (a) $Ra = 3.43 \times 10^5$, (b) $Ra = 3.53 \times 10^5$, (c) $Ra = 3.75 \times 10^5$, and (d) $Ra = 3.88 \times 10^5$.

resonances. As for the $m = 6$ and $m = 5$ solutions, the resonant three-frequency torus in Fig. 5.22(c) consists of a set of closed curves in the $\Theta(r_i + (r_o - r_i)/7, 0, 3\pi/8) = 0$ hyper-plane. The resonance of Fig. 5.22(d) consist of a complicated looped closed curve.

The existence of resonances could favour the possibility of large temporal scale solutions, since in nearly resonant solutions, there exist combinations of the frequencies of largest amplitudes which are close to zero. This is the case of the solution computed at $Ra = 3.680827 \times 10^5$ for which the frequency 3.452×10^{-2} gives long-scale variation of period $T = 28.97$. To illustrate this, the time series of $\Theta(r_i + (r_o - r_i)/7, 0, 3\pi/8)$, and their frequency spectra, at $Ra = 3.680827 \times 10^5$, and $Ra = 3.73 \times 10^5$, are plotted in Figs. 5.23(a, b), and (c, d), respectively. Notice the period $T = 28.97$, and the location and relative high amplitude of the corresponding peak in Figs. 5.23(a), and (b),

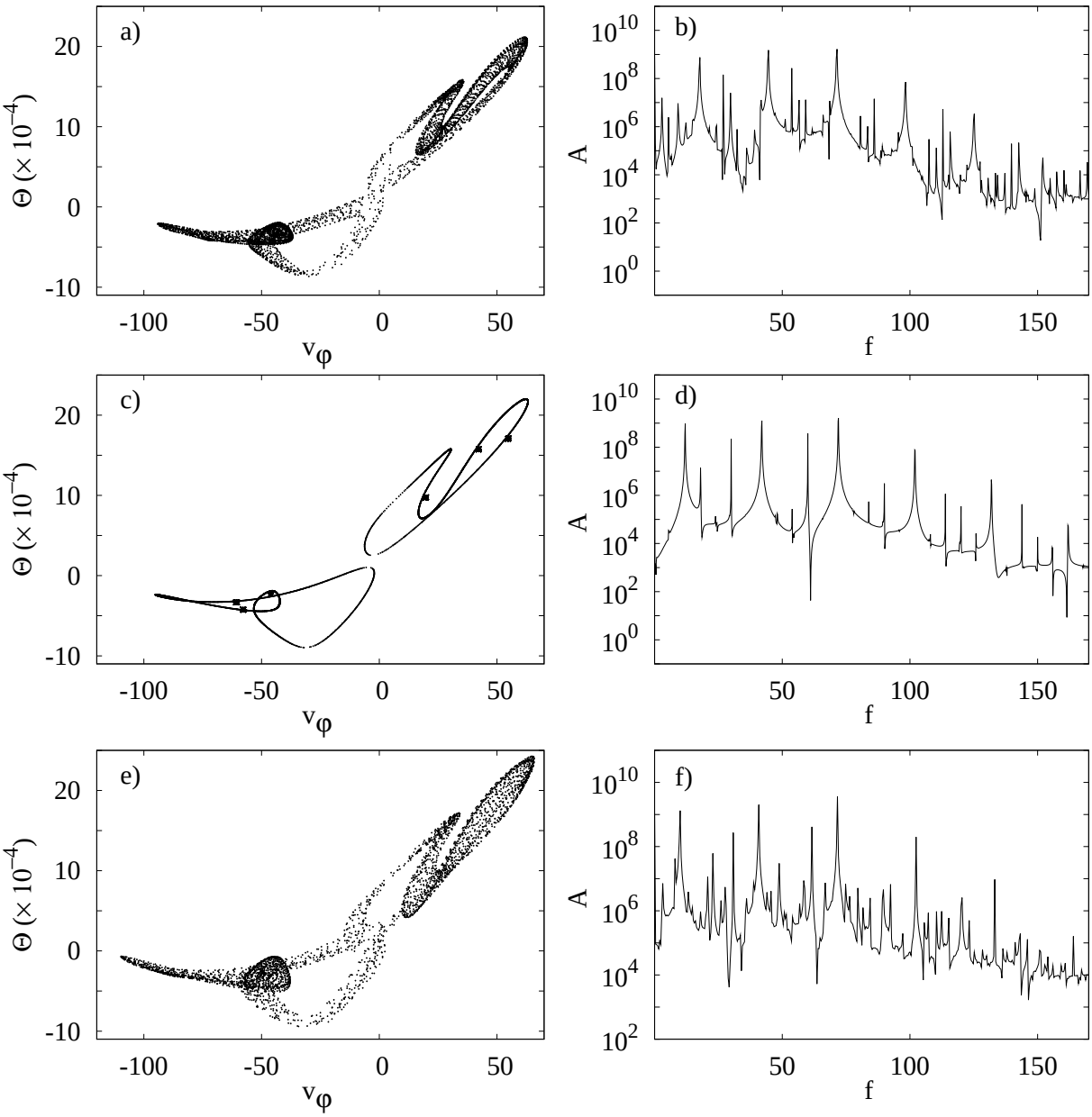

Figure 5.21: Same (a,c,e) Poincaré sections as in Fig. 5.11 for: (a) $Ra = 3.47 \times 10^5$ (band). (c) $Ra = 3.5038741 \times 10^5$ (set of points), and $Ra = 3.53 \times 10^5$ (closed curve). (e) $Ra = 3.55 \times 10^5$ (band). Same (b,d,f) frequency spectra as in Fig. 5.11 for $Ra = 3.47 \times 10^5$, $Ra = 3.53 \times 10^5$ and $Ra = 3.55 \times 10^5$, respectively.

respectively. The left peak of the frequency spectrum of Fig. 5.23(d) is not so close to zero and then lower temporal scales are expected as it is reflected in the time series of Fig. 5.23(c). The large temporal scale solution found here contrast with the results of [29] (with stress-free boundary conditions and $\sigma = 1$) in which no long temporal scales were found.

Contrarily to the $m = 6$ and $m = 5$ stable branch of 2-tori, the unstable $m = 4$ branch of 2-tori of Fig. 5.1(b) extends over a larger range, $Ra \in [3.2\times10^5, 3.7\times10^5]$. Again, several resonances are found. Some of them are shown in Fig. 5.24, where $\Theta((r_i+r_o)/2, 0, 3\pi/8)$, is plotted versus $\Theta((r_i + r_o)/4, 0, 3\pi/8)$. In this type of plots, the resonances on a 2-tori

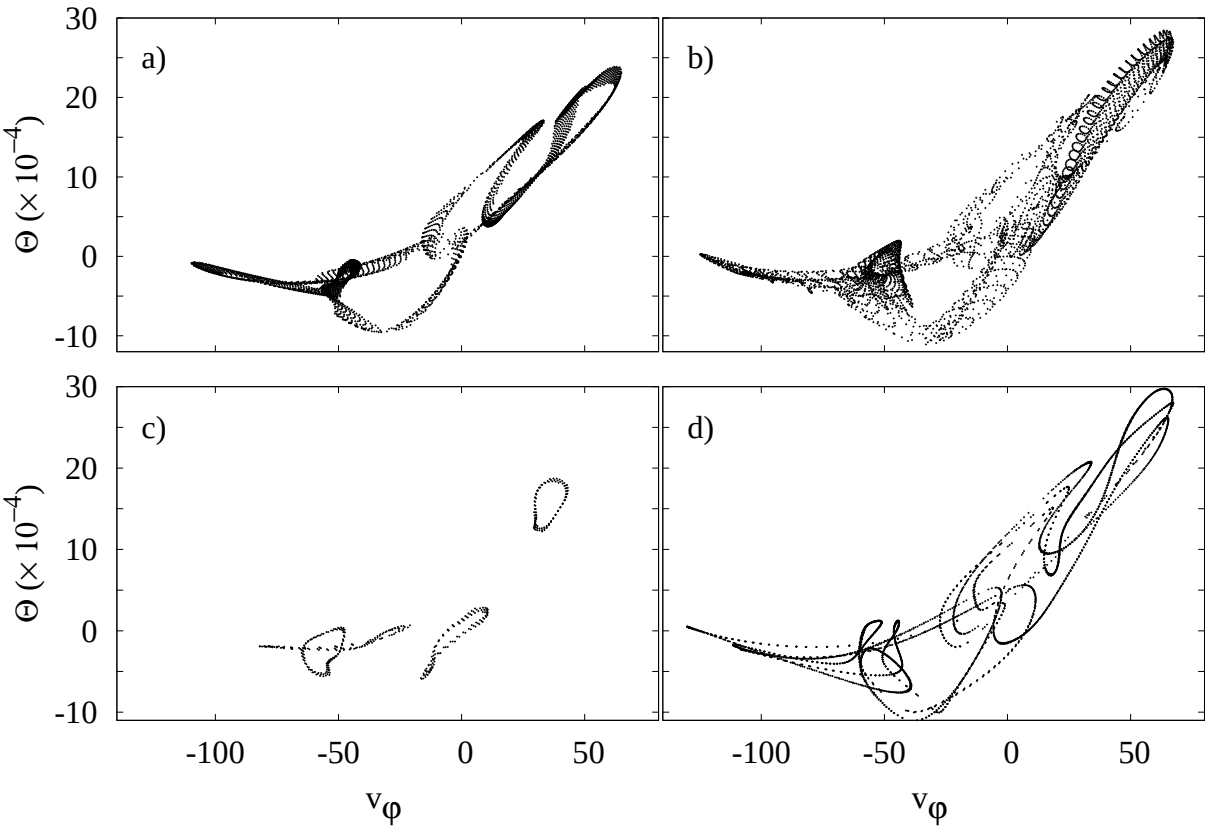

Figure 5.22: Same Poincaré sections as in Fig. 5.11. (a) $Ra = 3.56 \times 10^5$ (surface), (b) $Ra = 3.680827 \times 10^5$ (surface), (c) $Ra = 3.681303 \times 10^5$ (closed curve) and (d) $Ra = 3.73 \times 10^5$ (closed curve).

are identified as a closed curves with loops. In Fig. 5.24(a-f) the number of loops before closing are 5, 3, 5, 6, 7 and 9, respectively.

All the mean physical properties on the stable $m = 4$ window increase monotonically (see Fig. 5.2), and with bigger slope than those of the $m = 6$ and $m = 5$ branches, except

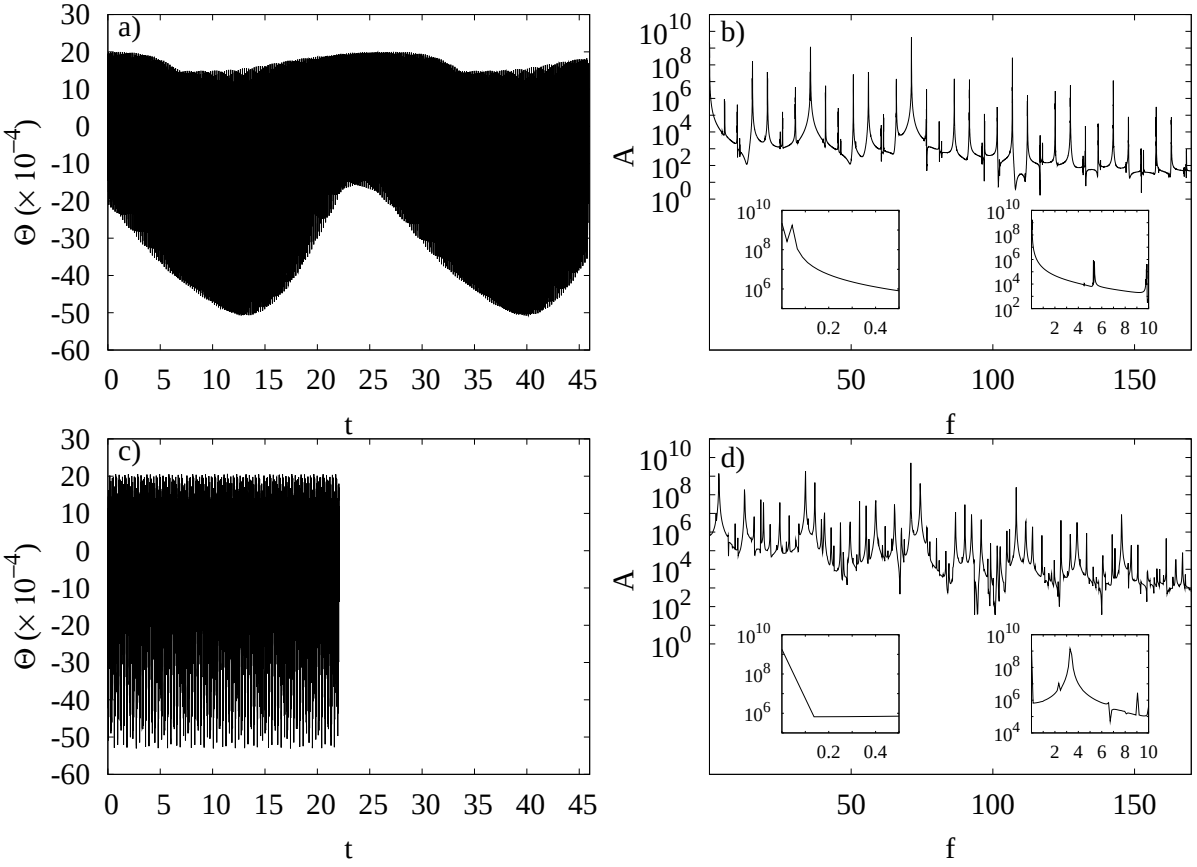

Figure 5.23: (a, c) Temperature perturbation $\Theta(r_i + (r_o - r_i)/7, 0, 3\pi/8)$, plotted versus time at $Ra = 3.680827 \times 10^5$ and $Ra = 3.73 \times 10^5$, respectively. (b, d) Same frequency spectra as in Fig. 5.11 at $Ra = 3.680827 \times 10^5$ and $Ra = 3.73 \times 10^5$, respectively.

for the ratio $\overline{K/K_{nz}}$ of Fig. 5.2(b). Although the interactions between the modes are stronger, the oscillations of these properties are substantially lower as it is reflected in the relative variance of Fig. 5.3. In fact when the solutions have two frequencies, the relative variance nearly vanishes, and the norms $||u_m||$ of Fig. 5.19(b) are nearly constant. Another remarkable difference is that the frequency of largest amplitude of the oscillation of these physical properties is considerably larger than in the $m = 6$ or $m = 5$ branches. Quasiperiodic solutions with very different periods in the kinetic energy density were found in [106] at low Prandtl number and with stress-free boundary conditions.

The same contour plots of Θ and $\mathbf{v}^2$ as in Fig. 5.9, are shown in Fig. 5.25 for $Ra = 3.53 \times 10^5$ as an example of the patterns of convection along the $m = 4$ branch. During a temporal evolution, the contour plots of Θ always keep five convective cells, which can be ordered by increasing intensity. The same happens with the kinetic energy density, although in the latter contour plots a connection between two convective cells can be

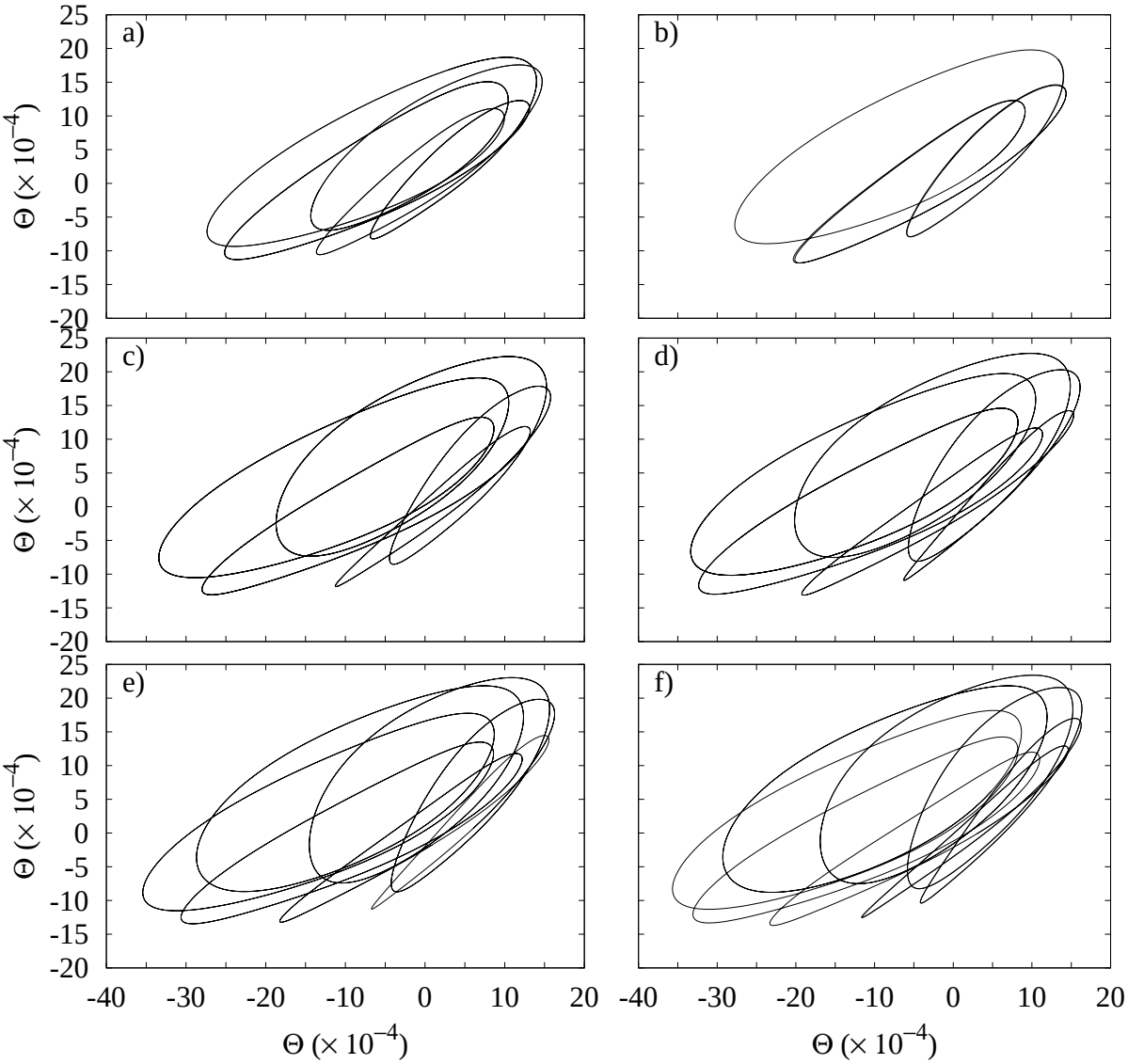

Figure 5.24: Temperature perturbation $\Theta((r_i + r_o)/2, 0, 3\pi/8)$, plotted versus $\Theta((r_i + r_o)/4, 0, 3\pi/8)$. The Rayleigh numbers are (a) $Ra = 3.274479 \times 10^5$, (b) $Ra = 3.3335 \times 10^5$, (c) $Ra = 3.457103 \times 10^5$, (d) $Ra = 3.489475 \times 10^5$, (e) $Ra = 3.51281 \times 10^5$, and (f) $Ra = 3.5304 \times 10^5$. The solutions are obtained by imposing two-fold azimuthal symmetry ($m_d = 2$).

observed. The relative magnitudes between the cells change during the time evolution, each cell reaching a minimum and maximum. The snapshots of the figure illustrate the variation of the intensity of the vortices of Θ on the equatorial plane. From $t = 0$ to

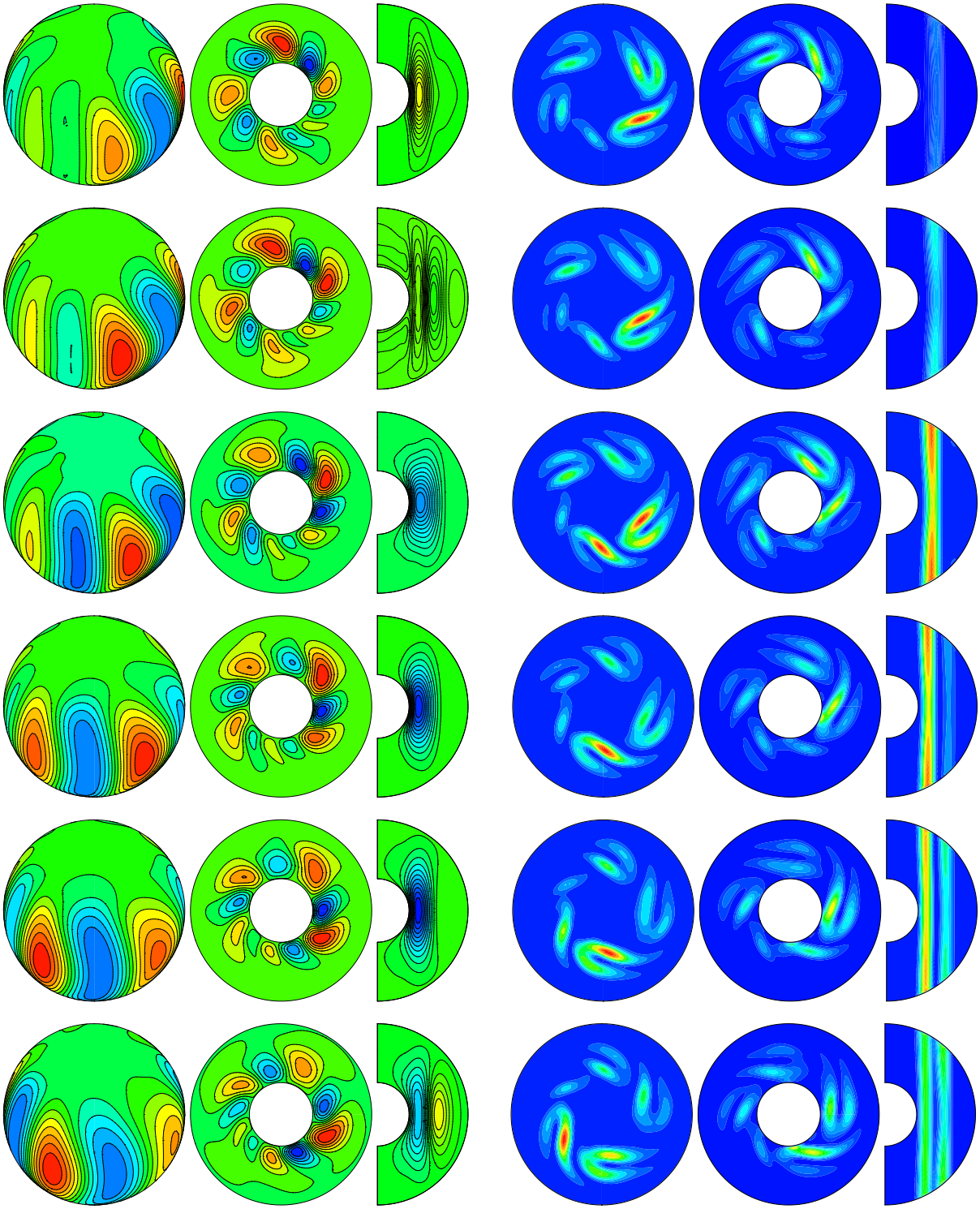

Figure 5.25: Same contour plots as in Fig. 5.9 for six snapshots corresponding to the evolution of a two-frequency solution on the $m = 4$ branch. From top to bottom, the snapshots are taken at $t = 0$, $t = 0.002$, $t = 0.004$, $t = 0.006$, $t = 0.008$, and $t = 0.01$. The Rayleigh number is $Ra = 3.53 \times 10^5$.

$t = 0.01$ the weakest vortex becomes the strongest. Another remarkable feature which exhibit these solutions is that the drifting of the cells is not at constant rate. Due to the strong interaction among the modes shown in Figs. 5.19 and 5.20, five convective cells can be identified in Fig. 5.25, although the dominant mode is $m = 4$. This contrasts with what occurred with the quasiperiodic motion on the $m = 6$ or $m = 5$ branches, in which the number of cells is equal to the dominant wave number.

5.3.4 Transition between $m = 4$ and $m = 3$ branches

After the quasiperiodic patterns of the stable $m = 4$ branch, a complex time dependence starts to grow beyond $Ra = 3.9 \times 10^5$ until $Ra = 5 \times 10^5$. In Fig. 5.26 similar frequency spectra as in Fig. 5.16, are shown. Despite their chaotic appearance, the highest amplitude peaks are located near $f = 70$, which is close to the frequency of largest amplitude of the previous solutions belonging to the stable $m = 4$ branch.

In Fig. 5.27 the norms of the vectors containing the amplitudes of the potentials and the temperature perturbation with $m = 3n$, $n \in \mathbb{N}$ (red), $m = 4n$ (green) and $m = 5n$ (blue), are plotted versus time. This complex time dependence roughly remembers that shown in Fig. 5.15 of section 5.3.2, in which, alternately, the norm $||u_m||$ of a certain mode with azimuthal wave number m is maximal and the norm $||u_p||$ of another mode with azimuthal wave number p is minimal. This is more clear in Figs. 5.27(e) and (f). For the former, plotted in the range $t \in (0.5, 1)$, the norm $||u_m||$, $m = 3n$ is maximal and the norms with $m = 4n$ or $m = 5n$ are minimal.

As in section 5.3.2, the stable solution at a given Ra could be related with unstable solutions computed, in this case, by imposing two-fold or three-fold azimuthal symmetry. This is shown in Fig. 5.28(a, b), for solutions at $Ra = 4 \times 10^5$ and $Ra = 4.8 \times 10^5$, respectively. In these figures, the Poincaré sections of the stable (blue) and the two unstable solutions are plotted. The latter are a two-frequency solution with $m = 3$ (red), and a three-frequency solution with $m = 4$ (green). The points of the stable section are scattered around to the points of the unstable sections, meaning that the dynamics of the three solutions share some features. Moreover, the physical quantities also reflect the relation between the stable and the two unstable solutions. To depict these, in Fig. 5.28(c, d) the ratios K/K_{nz} are plotted versus time. When the modes with $m = 3n$, $n \in \mathbb{N}$, have maximal norm and the norm of the modes with $m = 4n$ is minimal (see Fig. 5.28(e, f)), the energy ratio of the stable solution approaches that of the unstable $m = 3$, and viceversa. These features are better observed in Fig. 5.28(d). Nevertheless, they are not so clear as in section 5.3.2.

All the mean physical properties over this branch increase monotonically with Ra (see Fig. 5.2), except for the ratio $\overline{K/K_{nz}}$ of Fig. 5.2(b) in which the increase is less regular. However, the relative variance of these physical properties, shown in Fig. 5.3, is nearly constant.

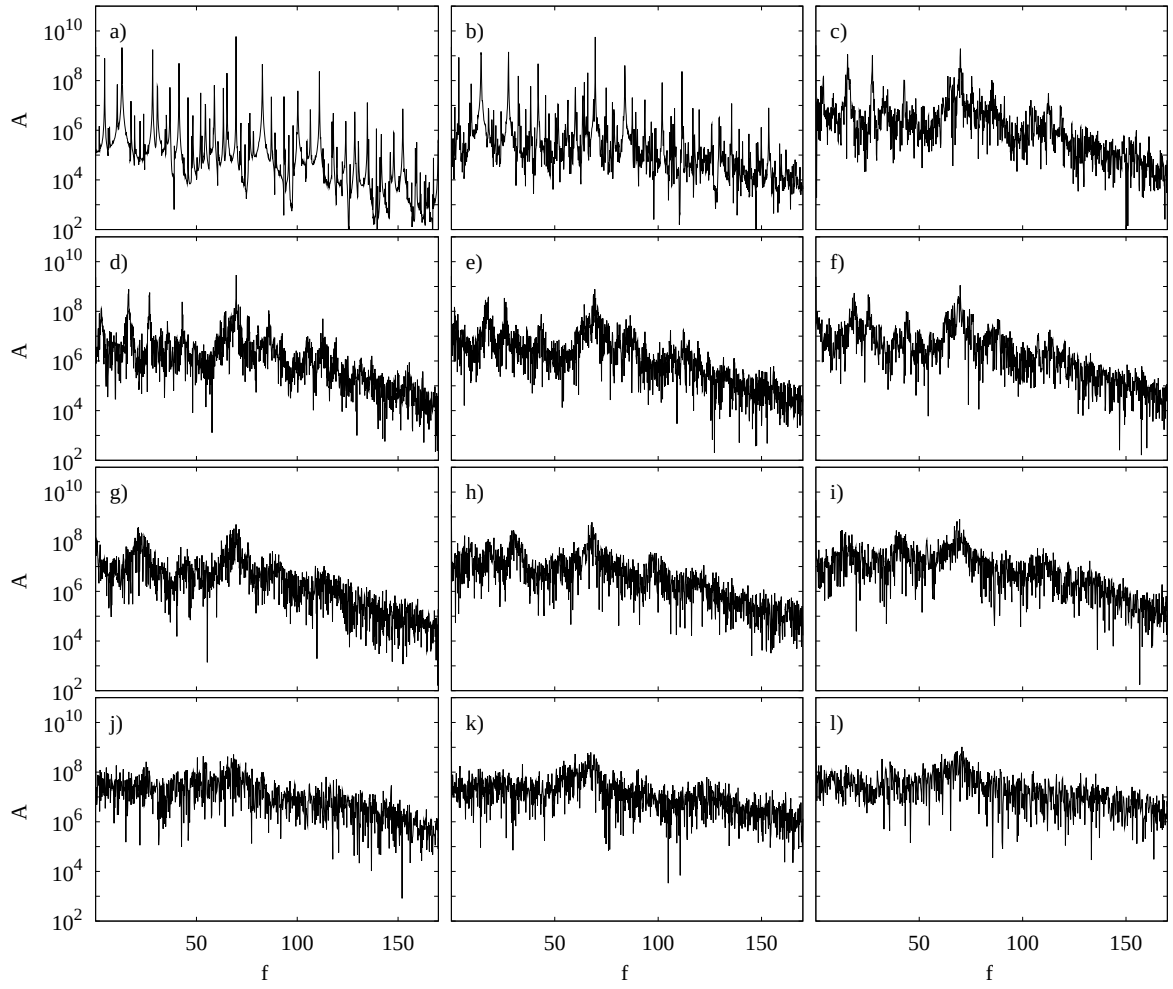

Figure 5.26: (a-l) Frequency spectrum of the time series of $\Theta(r_i + (r_o - r_i)/7, 0, 3\pi/8)$. The Rayleigh numbers are (a) $Ra = 3.88 \times 10^5$, (b) $Ra = 3.9 \times 10^5$, (c) $Ra = 3.92 \times 10^5$, (d) $Ra = 3.94 \times 10^5$, (e) $Ra = 3.96 \times 10^5$, (f) $Ra = 3.98 \times 10^5$, (g) $Ra = 4.0 \times 10^5$, (h) $Ra = 4.2 \times 10^5$, (i) $Ra = 4.4 \times 10^5$, (j) $Ra = 4.6 \times 10^5$, (k) $Ra = 4.8 \times 10^5$, and (l) $Ra = 4.9 \times 10^5$.

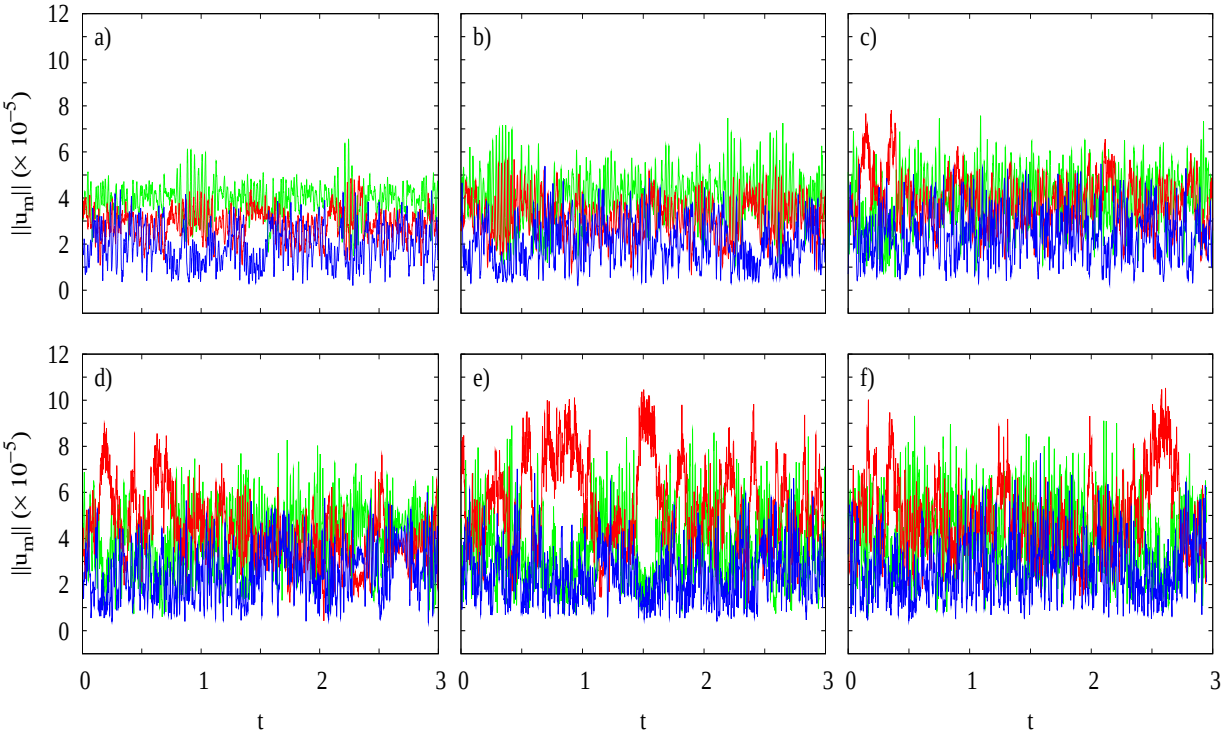

Figure 5.27: Norms of the vectors of the amplitudes of the potentials and the temperature perturbation with $m = 3n$, $n \in \mathbb{N}$ (red), $m = 4n$ (green) and $m = 5n$ (blue), plotted versus time. The Rayleigh numbers are (a) $Ra = 4.0 \times 10^5$, (b) $Ra = 4.2 \times 10^5$, (c) $Ra = 4.4 \times 10^5$, (d) $Ra = 4.6 \times 10^5$, (e) $Ra = 4.8 \times 10^5$, and (f) $Ra = 4.9 \times 10^5$.

The patterns of convection remain similar along this branch. Six snapshots of the contour plots of the temperature perturbation and of the kinetic energy density at $Ra = 4.8 \times 10^5$ are shown in Fig. 5.29. The snapshot on the first row visualises the flow at $t = 0$ when the solution is close to the $m = 3$ unstable solution, the successive rows taken at $t = 0.003$, $t = 0.006$, $t = 0.009$, $t = 0.012$ and $t = 0.015$, exhibit the evolution of the stable solution approaching the $m = 4$ unstable solution. In the last row the $m = 4$ pattern can be clearly distinguished. Notice, in the contour plots of the kinetic energy density notice that the most energetic cell can be located either near the outer boundary at high latitudes (see spherical section of first row) or close to the inner boundary at equatorial regions (see equatorial section of second row). This contrasts with what occurs for the solutions studied in previous sections in which the maximum is always located near the outer boundary.

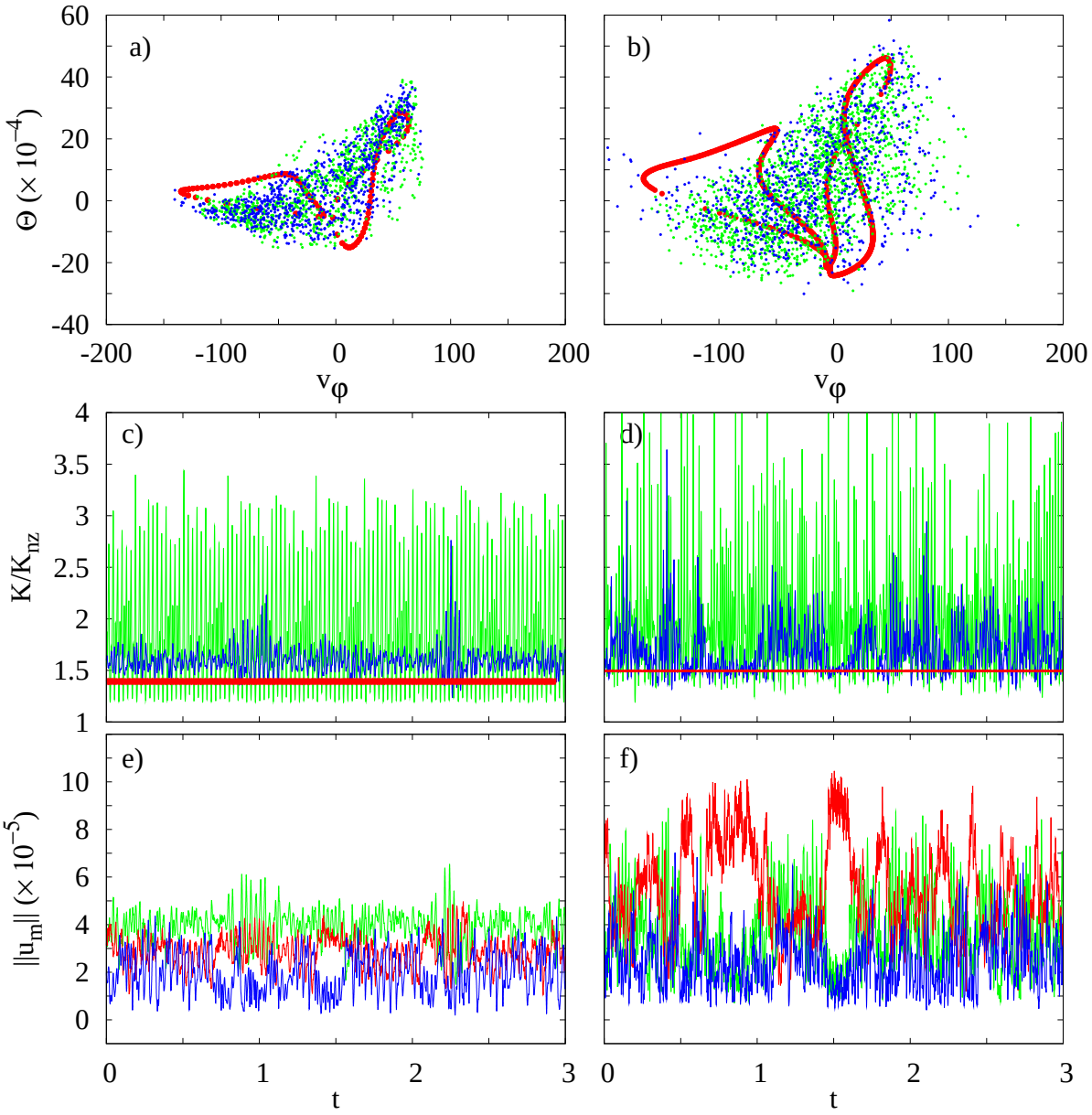

Figure 5.28: (a, b) Same Poincaré sections as in Fig. 5.11. The colours mean: $m = 3$ unstable two-frequency solutions (red), $m = 4$ unstable three-frequency solutions (green), and the chaotic orbit (blue). (c, d) Ratio of the total to the non-zonal kinetic energy densities of the stable solution (blue), of the $m = 3$ unstable solution (red) and of the $m = 4$ unstable solution (green), plotted versus time. (e, f) Norms of the vectors of the amplitudes of the potentials and the temperature perturbation with $m = 3n$, $n \in \mathbb{N}$ (red), $m = 4n$ (green) and with (blue), plotted versus time. The plots (a, c, e) are for $Ra = 4.0 \times 10^5$ and (b, d, f) for $Ra = 4.8 \times 10^5$.

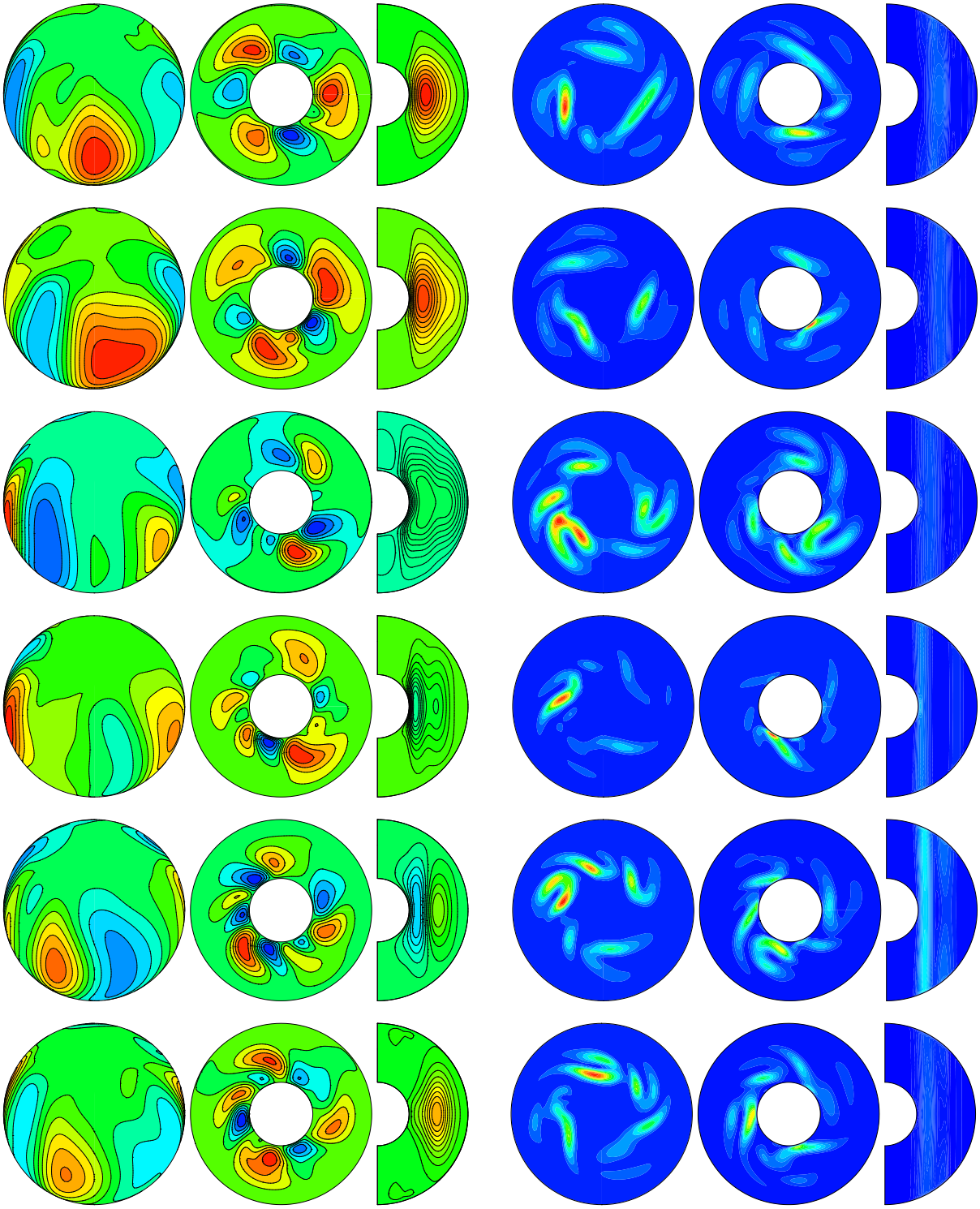

Figure 5.29: Same contour plots as in Fig. 5.9 for six snapshots corresponding to the evolution of chaotic solution. From top to bottom, the snapshots are taken at $t = 0$, $t = 0.003$, $t = 0.006$, $t = 0.009$, $t = 0.012$, and $t = 0.015$. The Rayleigh number is $Ra = 4.8 \times 10^5$.

5.3.5 $m = 3$ branch of solutions

At approximately $Ra = 5 \times 10^5$, a new interval of regular stable solutions begins (see Fig. 5.1(a)). For these solutions, the dominant mode is $m = 3$. This is shown in Fig. 5.30, where the norms of the vectors of the amplitudes of the potentials and the temperature perturbation with $m = 3n$ (red), $m = 4n$ (green), $m = 5n$ (blue), and $m = 6n$ (magenta) with $n \in \mathbb{N}$, and the ratios of these norms to the norm of the vector of all the amplitudes, are plotted versus time for two selected solutions, computed at $Ra = 5.1 \times 10^5$ and $Ra = 5.62 \times 10^5$.

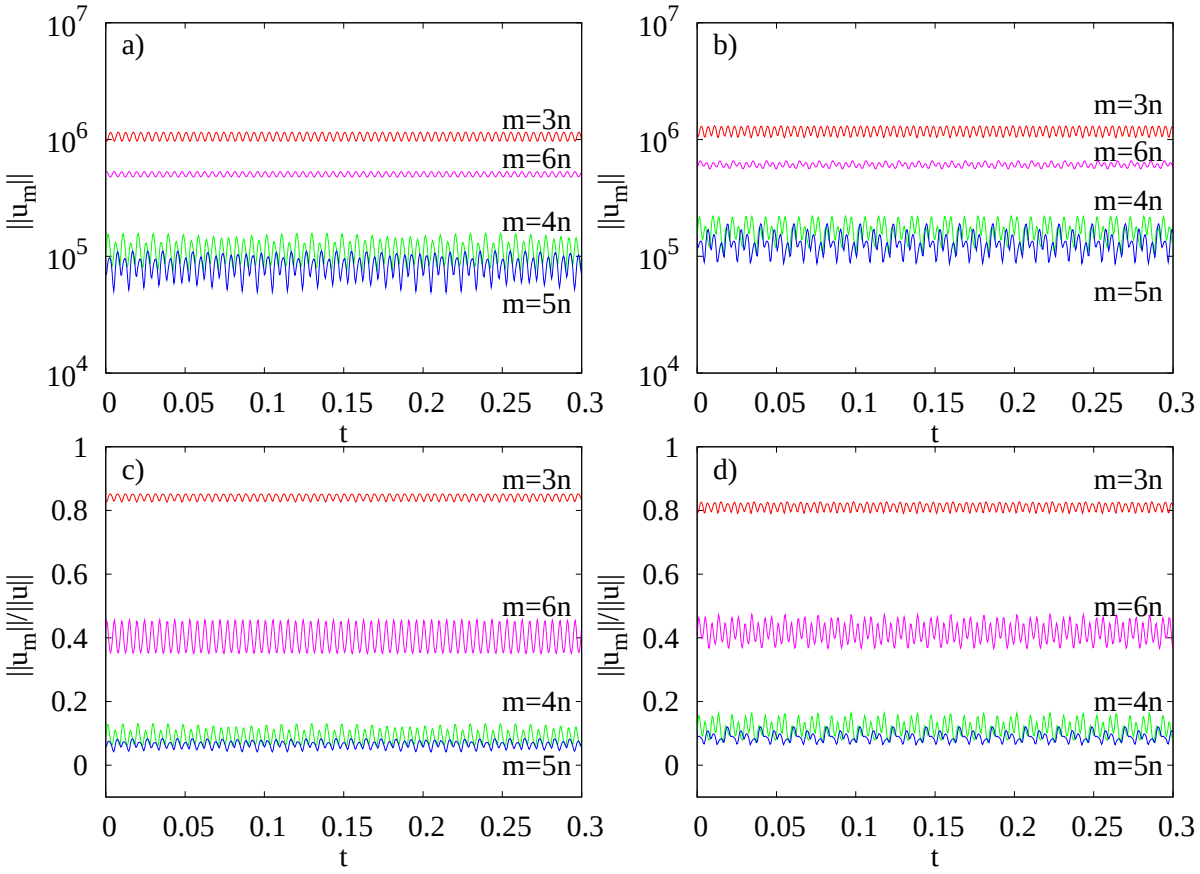

Figure 5.30: (a, b) Norms of the vectors of the amplitudes of the potentials and the temperature perturbation with $m = 3n$, (red), $m = 4n$ (green), $m = 5n$ (blue), and $m = 6n$ (magenta), $n \in \mathbb{N}$, plotted versus time. (c, d) Ratio of the norms of the vectors of the former amplitudes to the norm of the vector of all of them, plotted versus time. The Rayleigh numbers are (a, c) $Ra = 5.1 \times 10^5$, and (b, d) $Ra = 5.62 \times 10^5$.

The norm of the modes labelled $m = 3n$ is about 80% of the total norm, in contrast to what happened in the $m = 5$ and $m = 6$ branch, in which the dominant mode retains

more than 90% of the total norm (see Fig. 5.8). The ratio is bigger than in the $m = 4$ branch, where for the modes $m = 4n$ it was about 70% (see Fig. 5.20), and the ratios for other modes $m = 5n$ or $m = 6n$ were larger than 40%. Notice that in Fig. 5.30 most of the norm of the total vector is provided by the $m = 3n$ modes, being the amplitudes of the $m = 3$ and $m = 6$ modes of the same order of magnitude.

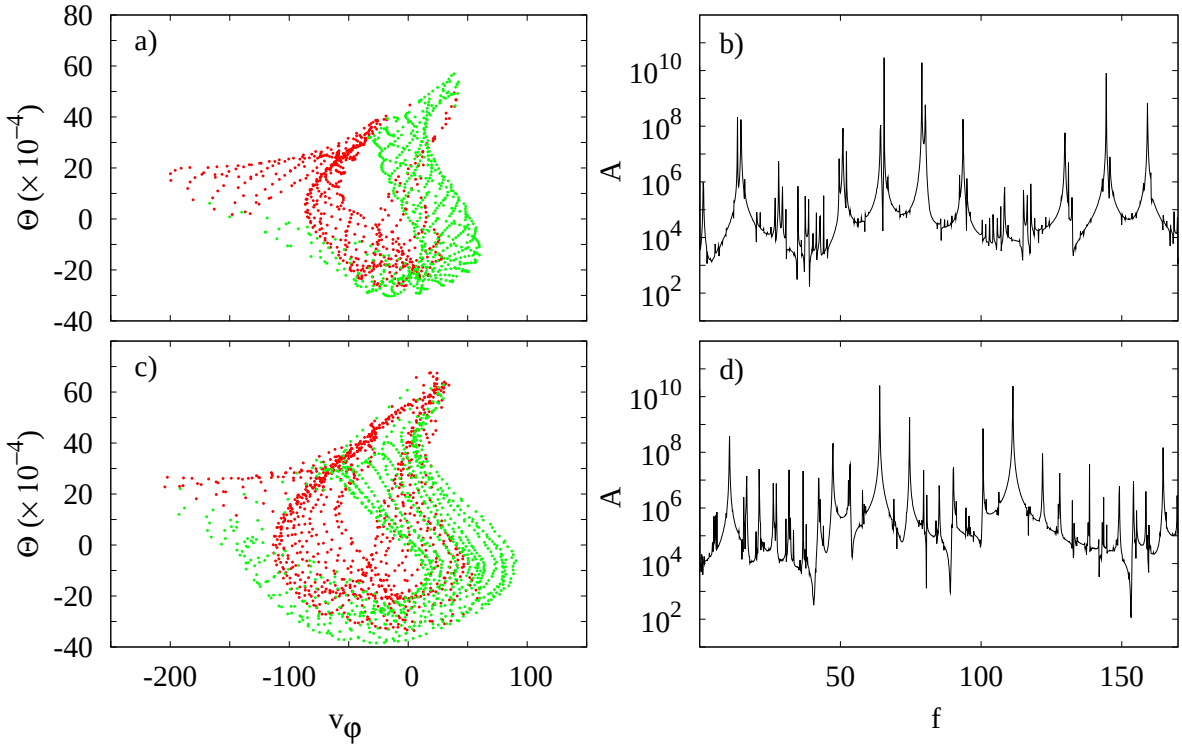

Figure 5.31: Same (a, c) Poincaré sections and (b, d) frequency spectra as in Fig. 5.11 for $Ra = 5.1 \times 10^5$, and $Ra = 5.62 \times 10^5$, respectively.

As in section 5.3.3 the quasiperiodic character of the solutions belonging to this window is identified by means of three independent Laskar frequencies of largest magnitude. Further analysis has to be performed in order to identify the origin of this motions and the physical meaning of the frequencies.

Similar Poincaré sections to those of Fig. 5.11 are shown in Fig. 5.31 as an example of a three-frequency solutions at $Ra = 5.1 \times 10^5$ and $Ra = 5.62 \times 10^5$. It also includes their frequency spectra. Contrarily to the $m = 6$, $m = 5$ or $m = 4$ branches, the surfaces on these Poincaré sections extend over a wider region in the $(\mathbf{v}_\varphi((r_i + r_o)/2, 0, 3\pi/8), \Theta((r_i + r_o)/2, 0, 3\pi/8)$ plane. This is because the amplitudes of $\mathbf{v}_\varphi$ and Θ increase with Ra. On the other hand, each frequency spectrum shows that the two highest peaks are of similar magnitude. This situation is similar to what happens in the $m = 4$ branch, but differs of

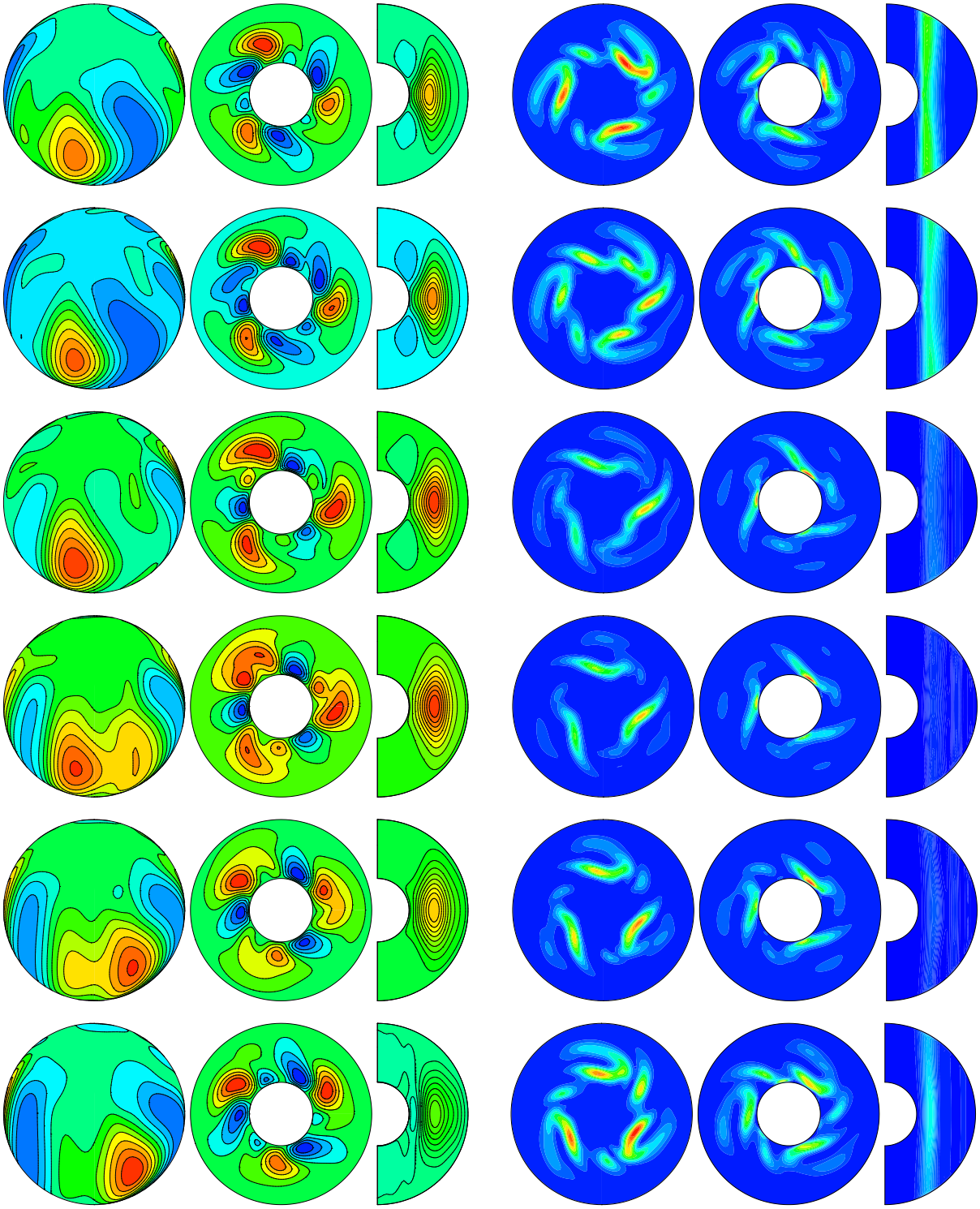

Figure 5.32: Same contour plots as in Fig. 5.9 for six snapshots corresponding to the evolution of a solution on the $m = 3$ branch. From top to bottom, the snapshots are taken at $t = 0$, $t = 0.001$, $t = 0.002$, $t = 0.003$, $t = 0.0004$, and $t = 0.005$. The Rayleigh number is $Ra = 5.1 \times 10^5$.

what occurs in the $m = 6$ or $m = 5$ branches in which the amplitude of the highest peak is considerably larger than the others.

At the beginning of this branch, all the physical properties rise, except for the ratio $\overline{K/K_{nz}}$ which falls substantially, and then increases monotonically with Ra (see Fig. 5.2). The abrupt change is also related with an abrupt fall of the relative variance of the physical properties of Fig. 5.3). This falling of the relative variance was also found in the quasiperiodic motions of the $m = 4$ branch.

Contrarily to the solutions of the previous chaotic branch, the oscillations along this branch are weak and then zonal circulations are less favoured. At the end of the branch, the ratio $\overline{K/K_{nz}}$ rises while the other mean physical properties fall. The abrupt changes on the mean physical properties and their low relative variation identify clearly this window of quasiperiodic motion. As in the $m = 4$ branch the time oscillations of the volume-averaged physical properties are fast than those found for the solutions on the $m = 6$ or $m = 5$ branches.

The contour plots of the temperature perturbation and of the kinetic energy density are shown in Fig. 5.32. They are representative of the patterns of convection of the solutions described in this section, and have been obtained with $Ra = 5.1 \times 10^5$. The first row corresponds to the snapshot taken at $t = 0$. From top to bottom, the successive rows are snapshots taken at times $t = 0.001, 0.002, 0.003, 0.004, 0.005$.

During the evolution of Θ, significative differences exist between the size of both cold and hot cells. There are always three hot and three cold big cells which are rotating counter-clockwise, but there are also intermittent periods in which three small cold cells, which connect with the big ones, appear, and periods in which the same occurs for the hot cells. This produces the effect as if the cells were advancing like a caterpillar (see in Fig. 5.32 the successive rows of the left column). The evolution of the kinetic energy density cells looks similar. Comparing the time evolution of the polar and equatorial contour plots of $\mathbf{v}^2$, it is observed, as in the previous section, that its maximum changes drastically its position between a point near the inner boundary at equatorial level, and a point near the outer at a high latitude. This effect does not occur in the quasiperiodic solutions described in previous sections where the maximum of $\mathbf{v}^2$ always remains near the outer boundary. Notice also that the vortices of $\mathbf{v}^2$ are more thiner and tilted than those of the previous regular motions.

5.3.6 Transition from the $m = 3$ branch to spatiotemporal chaos

For $Ra > 5.6 \times 10^5$ no more regular solutions are obtained. The dynamics at high Ra is strongly chaotic in space and time, and is progressively dominated by the even modes. In Fig. 5.33 the norms of the vectors of the amplitudes of the potentials and the temperature perturbation with $m = 3n$, $n \in \mathbb{N}$ (red), $m = 2n$ (green) and $m = 5n$ (blue), is plotted versus time, for $Ra = 5.8 \times 10^5$, $Ra = 6 \times 10^5$, $Ra = 7.5 \times 10^5$, $Ra = 10^6$, and $Ra = 2 \times 10^6$.

Close to the $m = 3$ branch (Figs. 5.33(a, b)), $||u_3||$ is still dominant, except in some

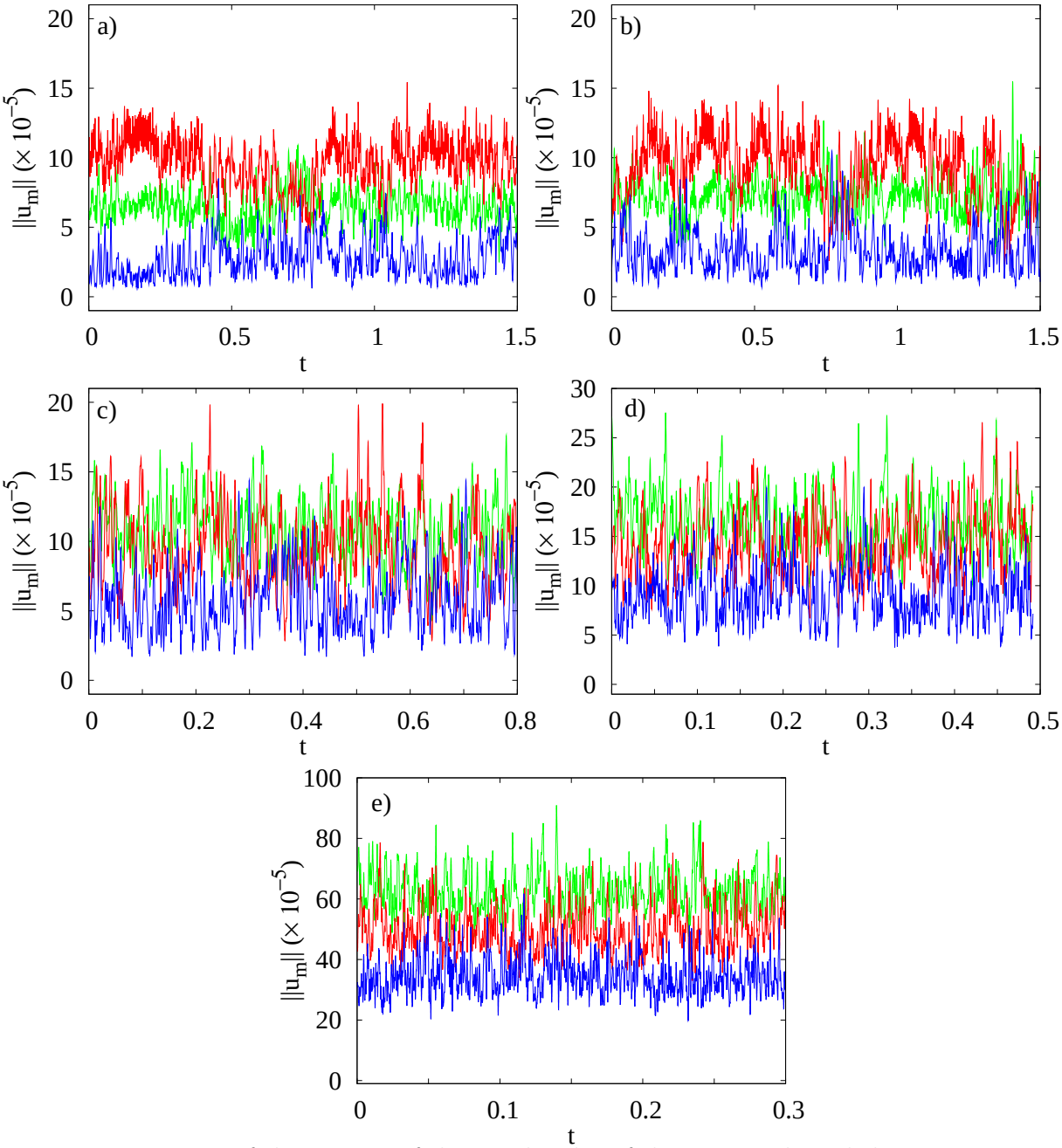

Figure 5.33: Norms of the vectors of the amplitudes of the potentials and the temperature perturbation with $m = 3n$, $n \in \mathbb{N}$ (red), $m = 2n$ (green), and $m = 5n$ (blue) plotted versus time. The Rayleigh numbers are (a) $Ra = 5.8 \times 10^5$, (b) $Ra = 6 \times 10^5$, (c) $Ra = 7.5 \times 10^5$, (d) $Ra = 10^6$, and (e) $Ra = 2 \times 10^6$.

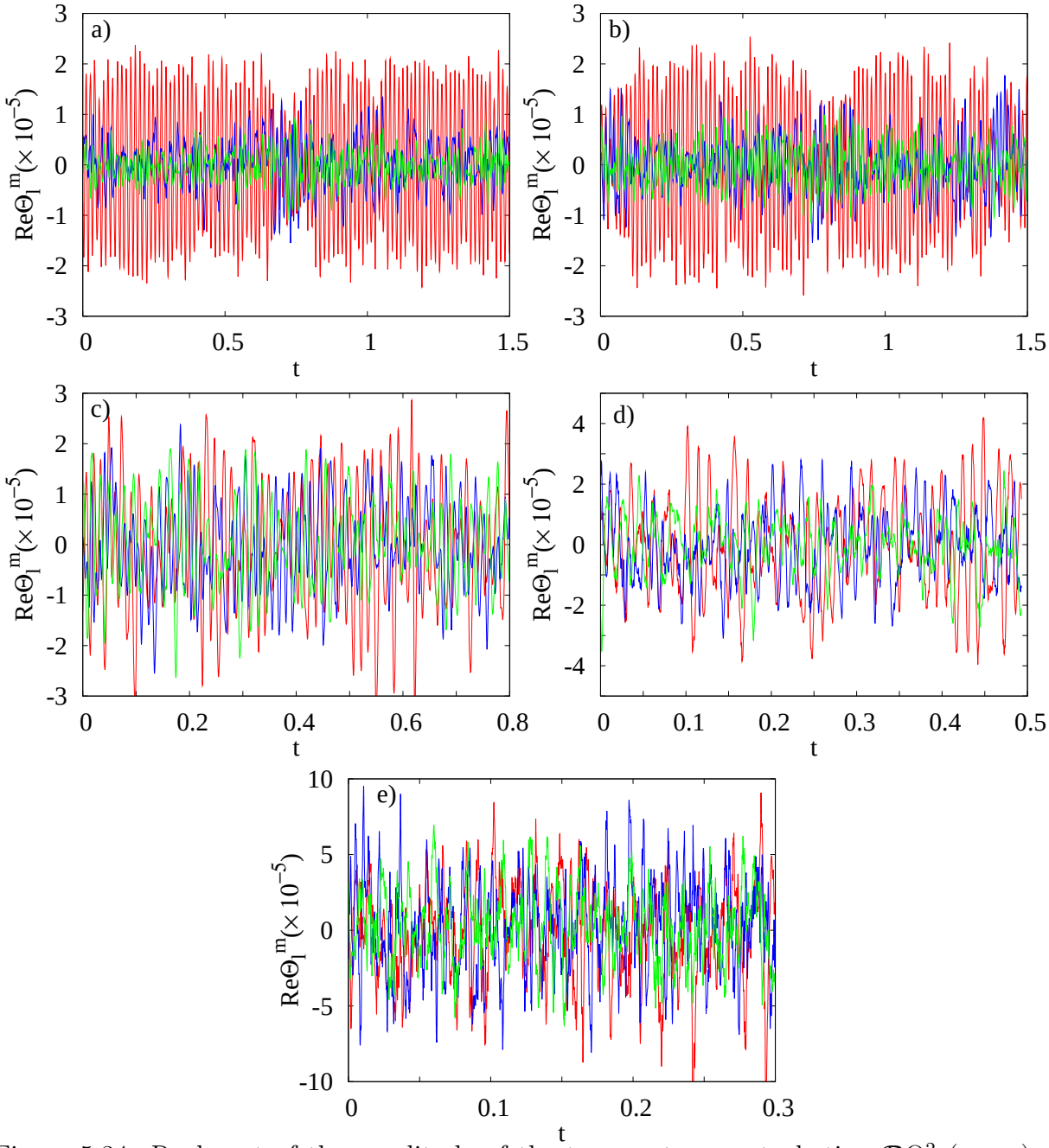

Figure 5.34: Real part of the amplitude of the temperature perturbation $\mathcal{R}\Theta_2^2$ (green), of $\mathcal{R}\Theta_3^3$ (red), and of $\mathcal{R}\Theta_4^4$ (blue), at the point $((r_i + r_o)/2, 0, 3\pi/8)$, plotted versus time. The Rayleigh numbers are (a) $Ra = 5.8 \times 10^5$, (b) $Ra = 6 \times 10^5$, (c) $Ra = 7.5 \times 10^5$, (d) $Ra = 10^6$, and (e) $Ra = 2 \times 10^6$.

small time intervals where $||u_2||$ becomes of larger norm. The norm of other modes as $||u_5||$ is smaller but not negligible. Perhaps, as in sections 5.3.2 or 5.3.4, the dynamics of this intermittent motion is dominated by unstable orbits with two and three-fold azimuthal symmetry, but in this case we have not checked this point. At about $Ra = 7.5 \times 10^5$ $||u_2||$ is comparable to $||u_3||$ (see Fig. 5.33(c)), and for $Ra \geq 10^6$ the former becomes more and more dominant (see Figs. 5.33(d, e)).

In Fig. 5.34 the real part of the amplitude of the temperature perturbation $\mathcal{R}\Theta_2^2$ (green), $\mathcal{R}\Theta_3^3$ (red), and $\mathcal{R}\Theta_4^4$ (blue), at the point $((r_i + r_o)/2, 0, 3\pi/8)$, are plotted versus time at the same Rayleigh numbers of Fig. 5.33. This figure shows the same chaotic behaviour as in Fig. 5.33, but allows to distinguish between the roles of the $m = 2$ and $m = 4$ modes. Close to $Ra = 5.8 \times 10^5$, the oscillations of $\mathcal{R}\Theta_3^3$ are clearly stronger than those of $\mathcal{R}\Theta_2^2$, or $\mathcal{R}\Theta_4^4$ (see Figs. 5.34(a, b)), but at high Rayleigh number $\mathcal{R}\Theta_m^m$ are similar for all the three m's indicating that nonlinear effects strongly dominate the dynamics.

Similar Poincaré sections as in Fig. 5.11 are shown in Fig. 5.35 for three different solutions at $Ra = 7.5 \times 10^5$, $Ra = 10^6$), and $Ra = 2 \times 10^6$. The corresponding frequency spectra are also shown. The two Poincaré sections depicted exhibit a clear chaotic behaviour and no trace of regularity can be distinguished. The frequency spectrum at $Ra = 7.5 \times 10^5$ still retain the largest amplitude peak close to the value of the frequency of largest amplitude of the solutions of the $m = 3$ branch of the previous section. For $Ra > 10^6$ the frequency spectra correspond to that of a fully chaotic time series.

Concerning the dependence of the physical properties on the Rayleigh number, by increasing Ra until 7.5×10^5 all the properties shown in Fig. 5.2 increase. Beyond this value, the ratio $\overline{K/K_{nz}}$ starts to decrease and the slopes of the other properties increase. Notice that the increase of $\overline{Ro_p}$ is more pronounced than that of $\overline{Ro}$, which agree with the fact that $\overline{K/K_{nz}}$ decreases, indicating that zonal circulations are unlikely. On the other hand, the relative variances of the properties shown in Fig. 5.3 are nearly constant and equal to 10%, except for the relative variance of the Nusselt number which increases very slowly.

The corresponding contour plots are shown in Fig. 5.36. The spherical sections for Θ are taken at $r = r_i + 0.325d$ and those for $\mathbf{v}^2$ at $r = r_i + 0.975d$. The rows, from top to bottom, correspond to the snapshots taken at times $t = 0, 0.0001$ and 0.0002. In the contour plots of chaotic solutions the time intervals are selected in order to see the breakings and mergings of the cells and vortices. Despite the complex time dependence of the solution at $Ra = 7.5 \times 10^5$ (see Fig. 5.31(a, b)), the contour plots retain remainders of regular patterns. As all the solutions described in the preceding sections, the z-dependence of the flow shown in the meridional sections is weak, and the flow is also equatorially symmetric. Moreover it can be observed that near the inner boundary the convection takes place with a larger wave number than out of the mean radius $r \approx (r_i + r_o)/2$. A differential rotation is observed. While the outer part of the shell maintains the prograde

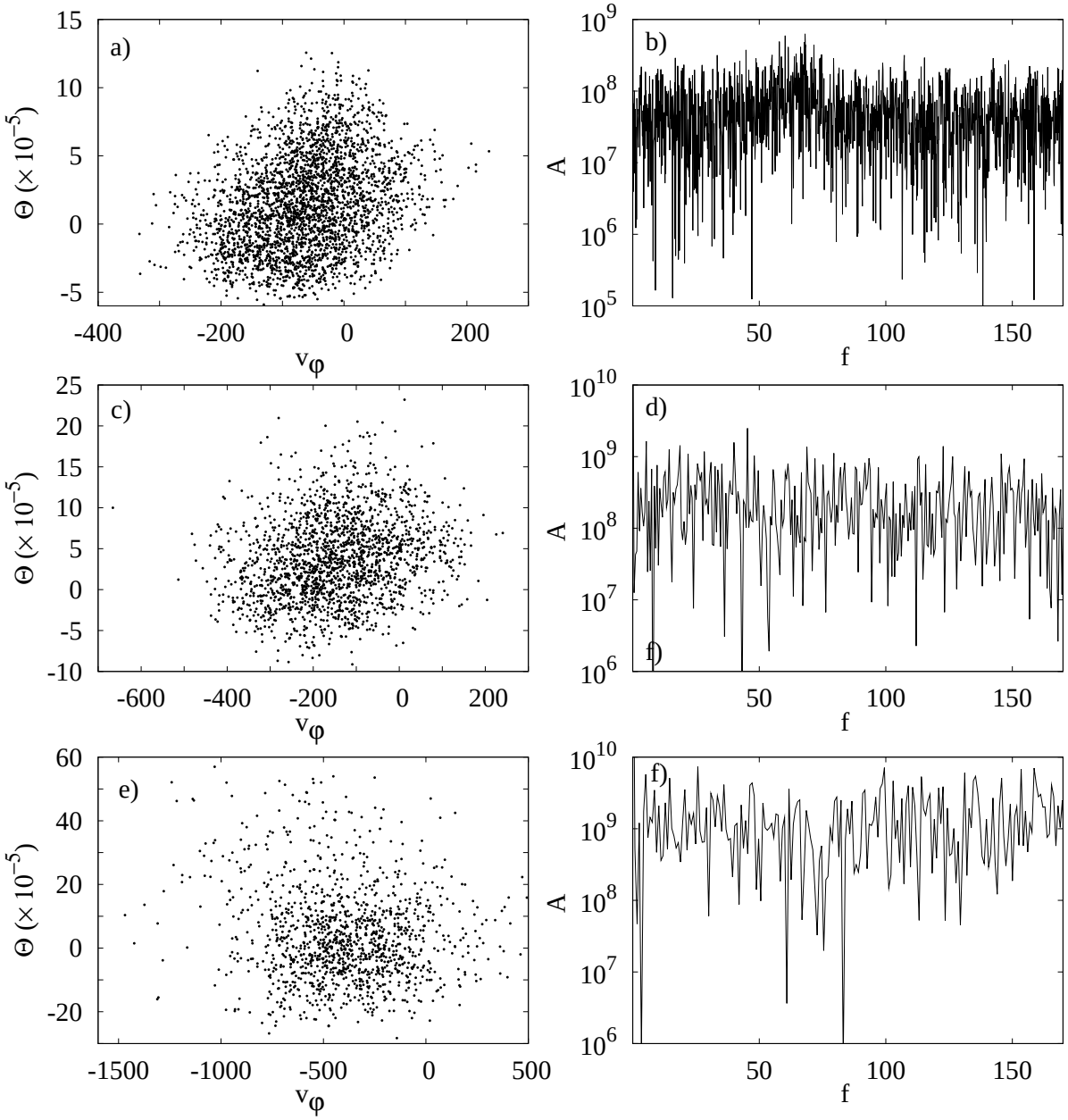

Figure 5.35: Same (a, c, e) Poincaré sections and (b, d, f) frequency spectra as in Fig. 5.11 for $Ra = 7.5 \times 10^5$, $Ra = 10^6$, and $Ra = 2. \times 10^6$, respectively.

drift the internal moves in the retrograde direction. As can be seen in the equatorial sections of Θ in Fig. 5.36 the largest cells merge with the smallest. Another remarkable feature of the contour plots of Θ, is that there is a clear difference in the size of the cold an hot cells, the latter extending far away from the inner boundary. On the other hand, in the contour plots of the kinetic energy density a two cylindrical layer structure with

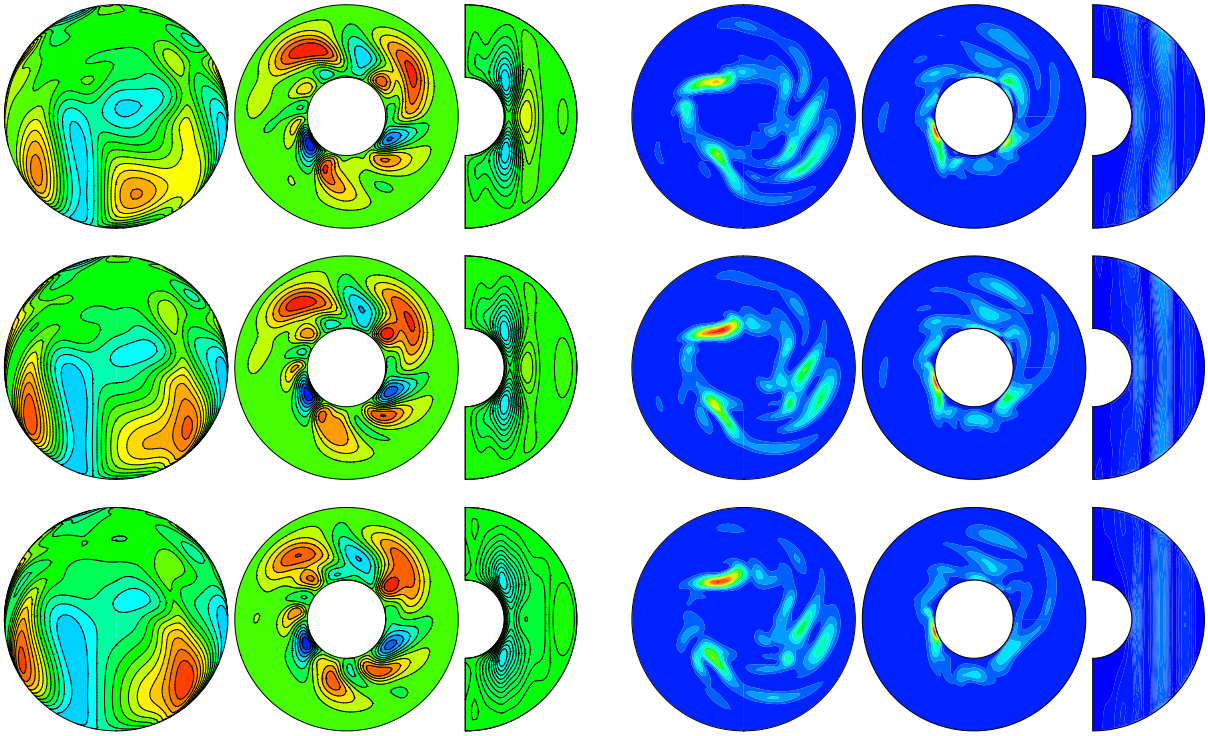

Figure 5.36: Same contour plots as in Fig. 5.9 for three snapshots corresponding to the evolution of a spatiotemporal chaotic solution. From top to bottom, the snapshots are taken at $t = 0$, $t = 0.0004$, and $t = 0.0008$. The Rayleigh number is $Ra = 7.5 \times 10^5$.

spiralling and connecting thin cells can be observed. As happened in the solutions of the $m = 3$ branch of section 5.3.5, the maximum of $\mathbf{v}^2$ travels from the equatorial inner to the nearly polar outer boundary (see the vortices of the spherical and equatorial sections in the right column of Fig. 5.36).

Similar patterns of convection as for $Ra = 7.5 \times 10^5$ are observed at $Ra = 10^6$ but in this case convection extends over a wider region, and the polar convection starts to be important (see spherical sections of the left column of Fig. 5.37). In this figure the spherical sections for Θ are taken at $r = r_i + 0.275d$ and those for $\mathbf{v}^2$ at $r = r_i + 0.975d$. At this Rayleigh number the number of smallest cells/vortices in the contour plots of $\Theta/\mathbf{v}^2$ increases, although there are also some bigger cells/vortices which are connected producing large-scale structures.

Finally, some snapshots of Θ and $\mathbf{v}^2$ are plotted in Fig. 5.38 for $Ra = 2 \times 10^6$. The spherical sections for Θ are taken at $r = r_i + 0.3625d$ and those for $\mathbf{v}^2$ at $r = r_i + 0.9625d$. As can be seen in the meridional sections, the equatorial symmetry is broken, and the z-dependence of the flow is enhanced, although a rough quasi-geostrophic structure still remains. During the time evolution small-scale cells are generated

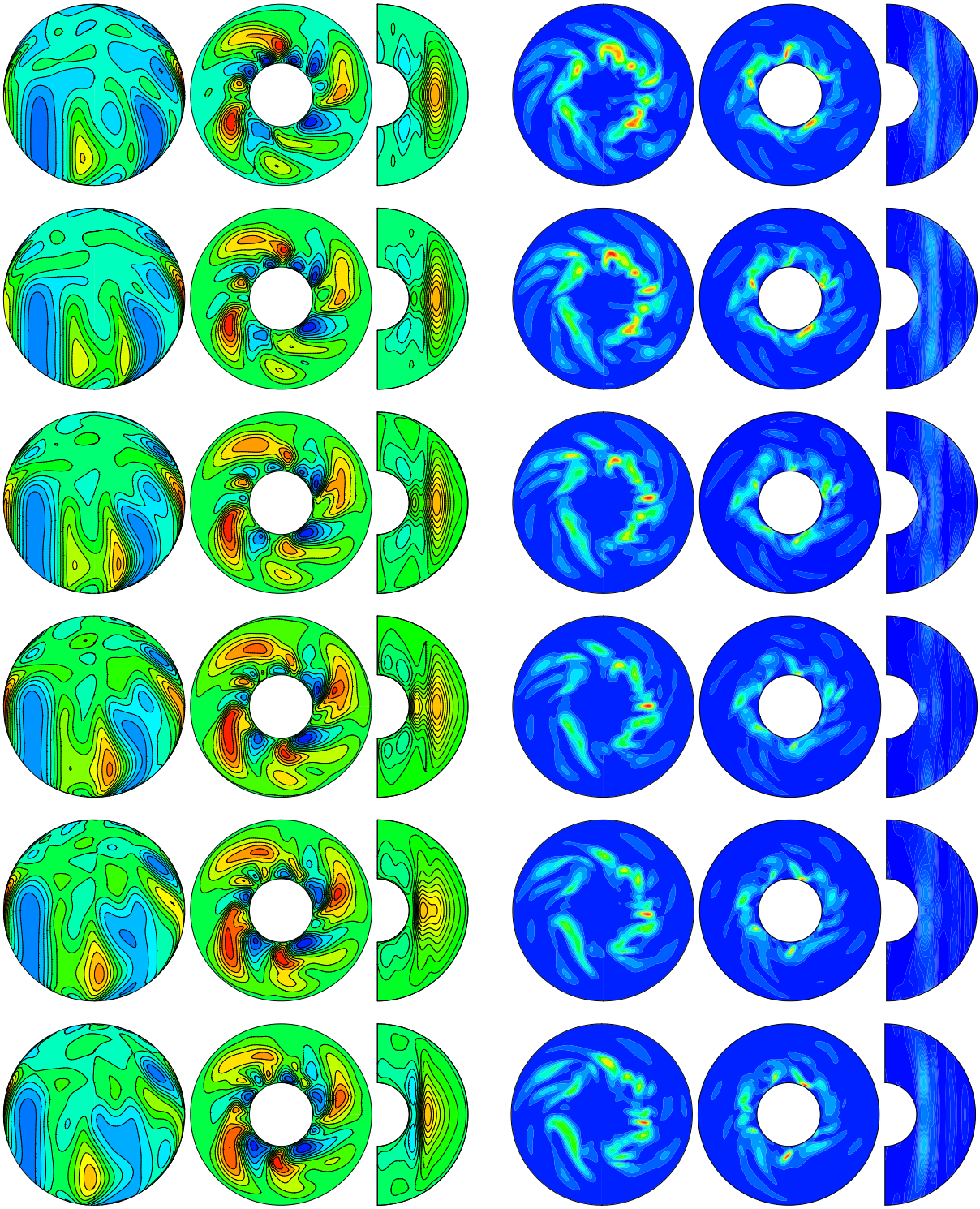

Figure 5.37: Same contour plots as in Fig. 5.9 for six snapshots corresponding to the evolution of a spatiotemporal chaotic solution. From top to bottom, the snapshots are taken at $t = 0$, $t = 0.0002$, $t = 0.0004$, $t = 0.0006$, $t = 0.0008$ and $t = 0.001$. The Rayleigh number is $Ra = 10^6$.

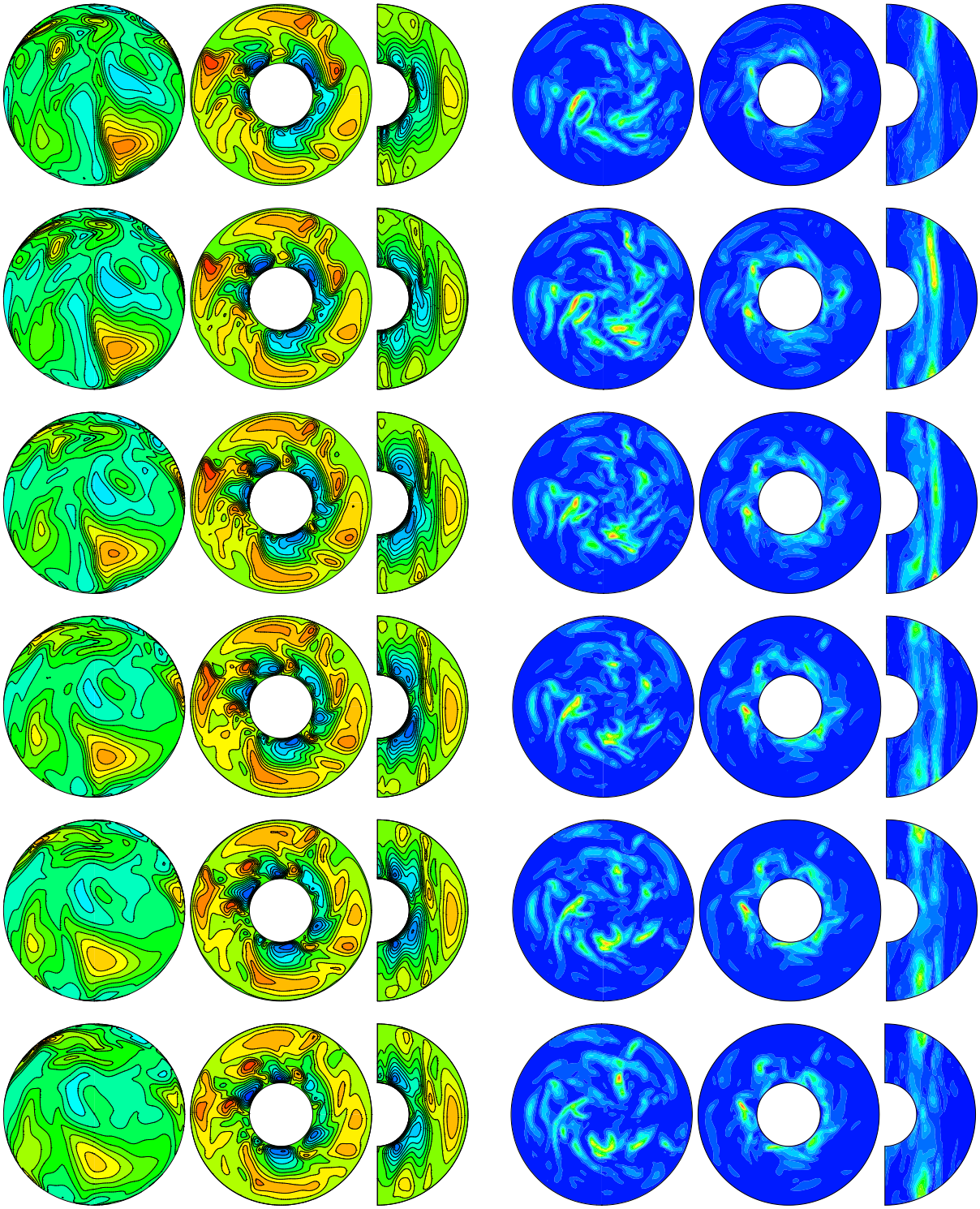

Figure 5.38: Same contour plots as in Fig. 5.9 for six snapshots corresponding to the evolution of a chaotic solution. From top to bottom, the snapshots are taken at $t = 0$, $t = 0.0001$, $t = 0.0002$, $t = 0.0003$, $t = 0.0004$, and $t = 0.0005$. The Rayleigh number is $Ra = 2 \times 10^6$.

and reconnected following the two layer cylindrical structure. As for $Ra = 7.5 \times 10^5$ or $Ra = 10^6$, the outer cylinder is clearly filled by hot connected cells, while in the inner most of the cells are cold. The boundary of the two regions is located around $r \approx r_i + (r_o - r_i)/3$, meaning that the hot cells extend over a wider region at this Rayleigh number (compare the equatorial sections of the second column in Fig. 5.38 with those of Figs. 5.36 and 5.37). On the other hand, the convection in the polar regions is now clearly developed as can be observed in the contour plots of the kinetic energy density, as well as in the Θ spherical sections.

5.4 Location of convection

In this section, the study of time-averaged local quantities, extracted from a sequence of solutions obtained by increasing Ra is shown to understand the variation of the location of convection with the Rayleigh number. The time-averaged quantities are obtained at representative collocation points. The position of the collocation points p_i, $i = 1, \ldots, 9$, is sketched in Fig. 5.39, and their spherical coordinates are given in the figure caption.

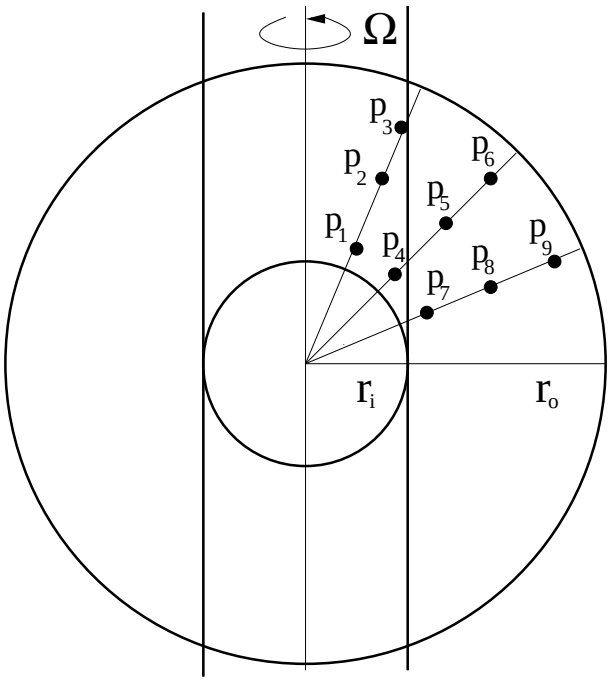

Figure 5.39: Meridional section at $\varphi = 0$ of the spherical shell showing the points p_i $i = 1, \ldots, 9$, where the time-averaged physical properties are monitored. Their colatitudinal coordinates are $\theta \approx \pi/8$, $\theta \approx \pi/4$, and $\theta \approx 3\pi/8$, and the radial $r = r_i + (r_o - r_i)/7$, $r = r_i + (r_o - r_i)/2$, and $r = r_i + 6(r_o - r_i)/7$.

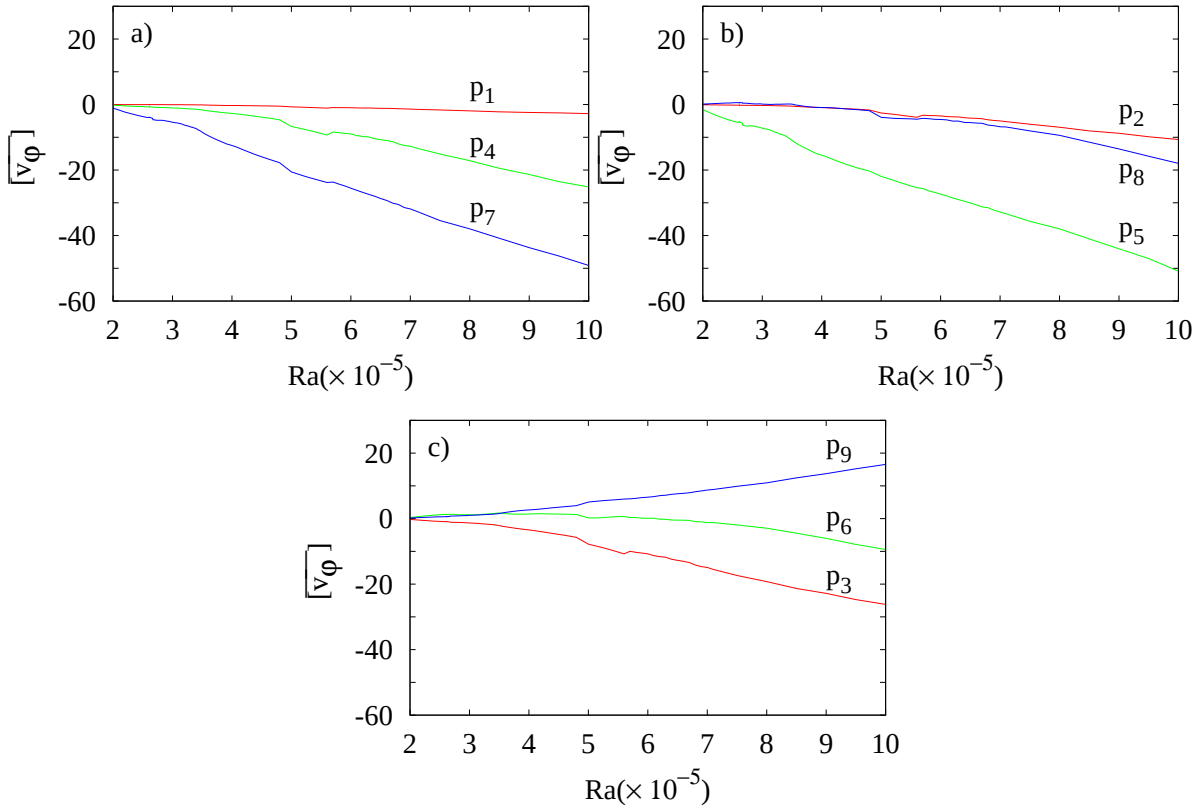

Figure 5.40: Time average of the azimuthally-averaged azimuthal component of the velocity field $[\overline{v_\varphi}]$, at different collocation points, plotted versus the Rayleigh number Ra. The spherical surfaces are taken at (a) $r = r_i + (r_o - r_i)/7$, (b) $r = r_i + (r_o - r_i)/2$, and (c) $r = r_i + 6(r_o - r_i)/7$. The colours mean: $\theta = \pi/8$ red, $\theta = \pi/4$ green, and $\theta = 3\pi/8$ blue. The labels on the curves denote the points of Fig. 5.39.

In Fig. 5.40, the time average of the azimuthally-averaged azimuthal component of the velocity field $[\overline{v_\varphi}]$ (mean zonal flow), at the collocation points p_i, $i = 1, \ldots, 9$, is plotted versus the Rayleigh number Ra. For $Ra < 5 \times 10^5$, only a weak negative mean zonal flow is created very close to the cylinder of Fig. 5.39. See the situation of points labelled as p_5 and p_7 and the values of the corresponding green and blue curves, respectively.

As the Rayleigh number is increased beyond $Ra = 5 \times 10^5$, the negative mean zonal flow increases and the retrograde mean zonal circulations spread affecting almost all the shell. This can be seen in Fig. 5.40 as a decrease of the mean zonal flow in the points p_2, p_3 and p_4 inside the tangent cylinder, and in the points p_5, p_6, p_7 and p_8 outside of it. In contrast, close to the outer boundary near the equator (point p_9), positive mean zonal flow starts to grow, becoming comparable to the negative circulations if the Rayleigh number is further increased. This prograde differential rotation near the equator at the outer

surface was also found in gallium experiments [6], or in numerical simulations [114] for Prandtl numbers $\sigma = 0.1, 1, 10$ and stress-free boundary conditions. It has been pointed out in [114] for $\sigma \leq 1$ that the mean zonal flow remains nearly constant along the axis of rotation as a consequence of the Taylor-Proudman constraint. This can be observed on Fig. 5.40, in which the points p_3 and p_4 and p_5 and p_7, each pair at a similar distance of the axis of rotation, exhibit nearly the same mean zonal flow. In the case of p_6 and p_8, also at slightly different distance from the axis of rotation, the mean zonal flow is (in modulus) larger at low latitudes (p_8). At this distance from the axis, the radial variation of the mean zonal flow is stronger.

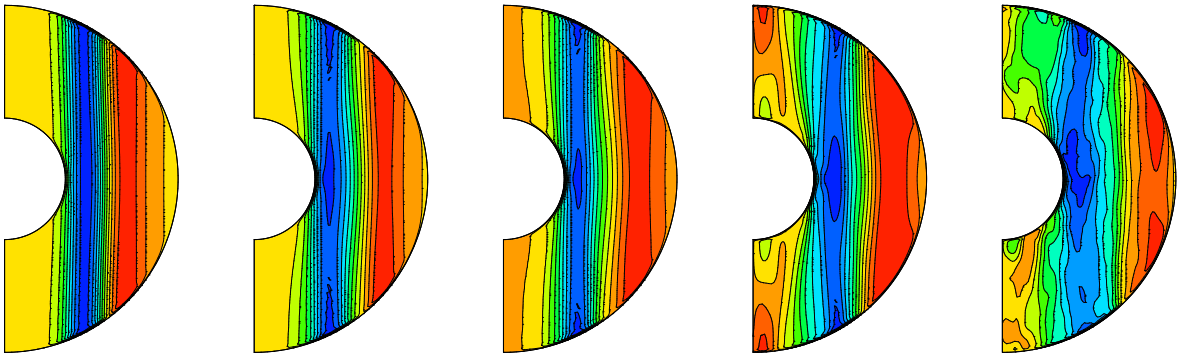

Figure 5.41: From left to right, contour plots of the azimuthally averaged azimuthal component of the velocity field $[v_\varphi]$ on a meridional section, at $Ra = 3.42 \times 10^5$, $Ra = 5.1 \times 10^5$, $Ra = 7.5 \times 10^5$, $Ra = 10^6$, and $Ra = 2 \times 10^6$, respectively.

In Fig. 5.41 the contour plots on a meridional section of a snapshot of the azimuthally averaged azimuthal component of the velocity field, $[v_\varphi]$, are shown for five representative Rayleigh numbers $Ra = 3.42 \times 10^5$, $Ra = 5.1 \times 10^5$, $Ra = 7.5 \times 10^5$, $Ra = 10^6$, and $Ra = 2 \times 10^6$. The scale of colours is different for each figure. Blue and red colours mean retrograde and prograde $[v_\varphi]$, respectively. In this sequence the above mentioned tendency of the negative circulations to expand to a wider region of the spherical shell, and the existence of positive circulations at low and mid latitudes close to the outer boundary, can be observed. With increasing Ra, the polar circulations start to develop, and the validity of the Taylor-Proudman constraint is progressively lost. At $Ra = 2 \times 10^6$, the equatorial symmetry is broken although the flows maintain a recognisable columnar structure.

To determine the importance of the azimuthal flows, the contour plots of a snapshot of the azimuthal component of the velocity field on a sphere, on the equatorial plane, and on a meridional section, are shown in Fig. 5.42 for the five representative Rayleigh numbers of Fig. 5.41 at the same time instant. The spherical sections are shown with a polar view and are taken at $r = r_i + 0.975d$ cutting the maxima of positive circulations. Meridional sections are taken at $\varphi = 0$. In this contour plots red/blue colours mean positive/negative values. The remarkable feature of this figure is that almost all the solutions exhibit the

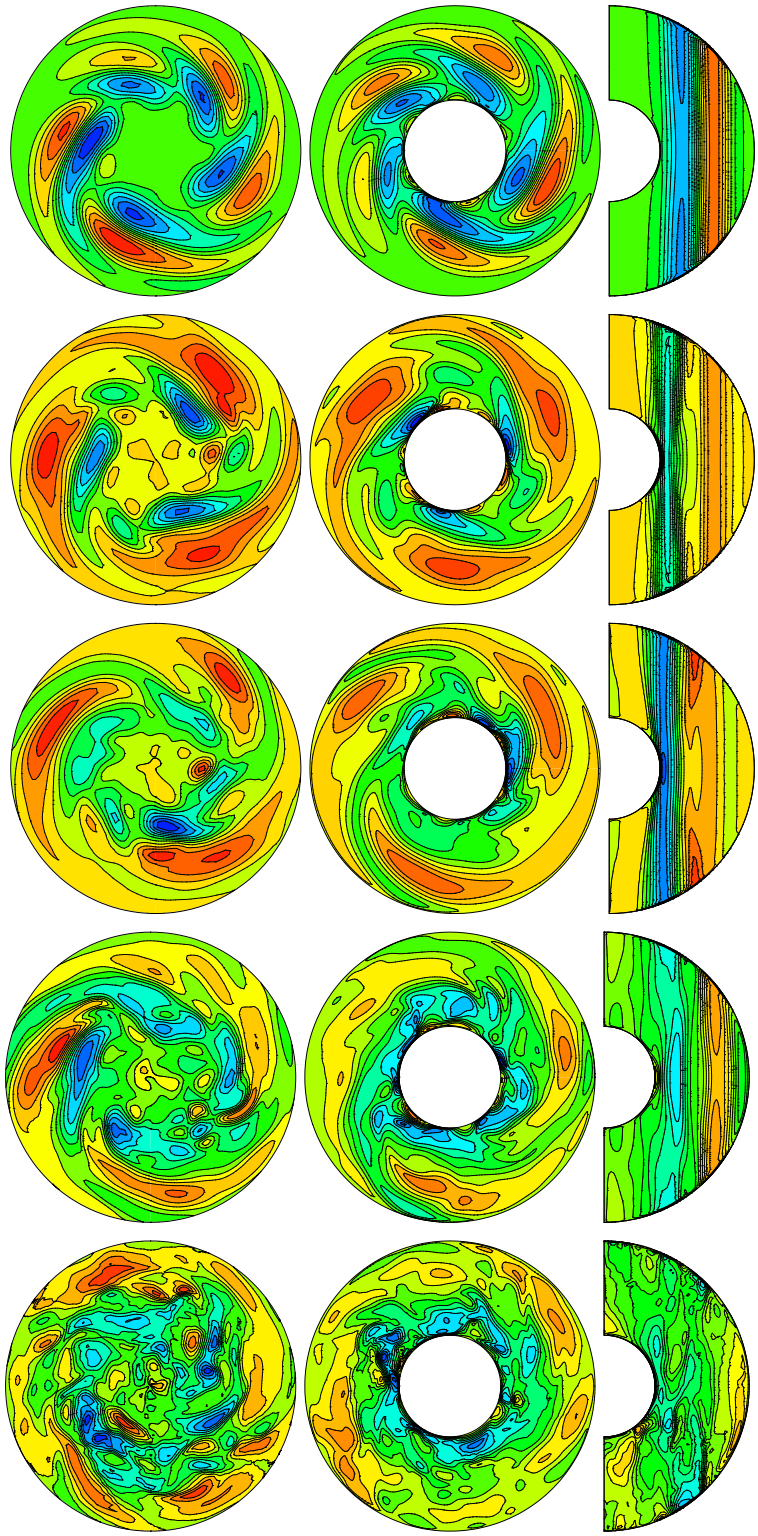

Figure 5.42: From top to bottom, contour plots of the azimuthal component of the velocity field, v_φ, on a sphere, on the equatorial plane, and on a meridional section, at $Ra = 3.42 \times 10^5$, $Ra = 5.1 \times 10^5$, $Ra = 7.5 \times 10^5$, $Ra = 10^6$, and $Ra = 2 \times 10^6$, respectively.

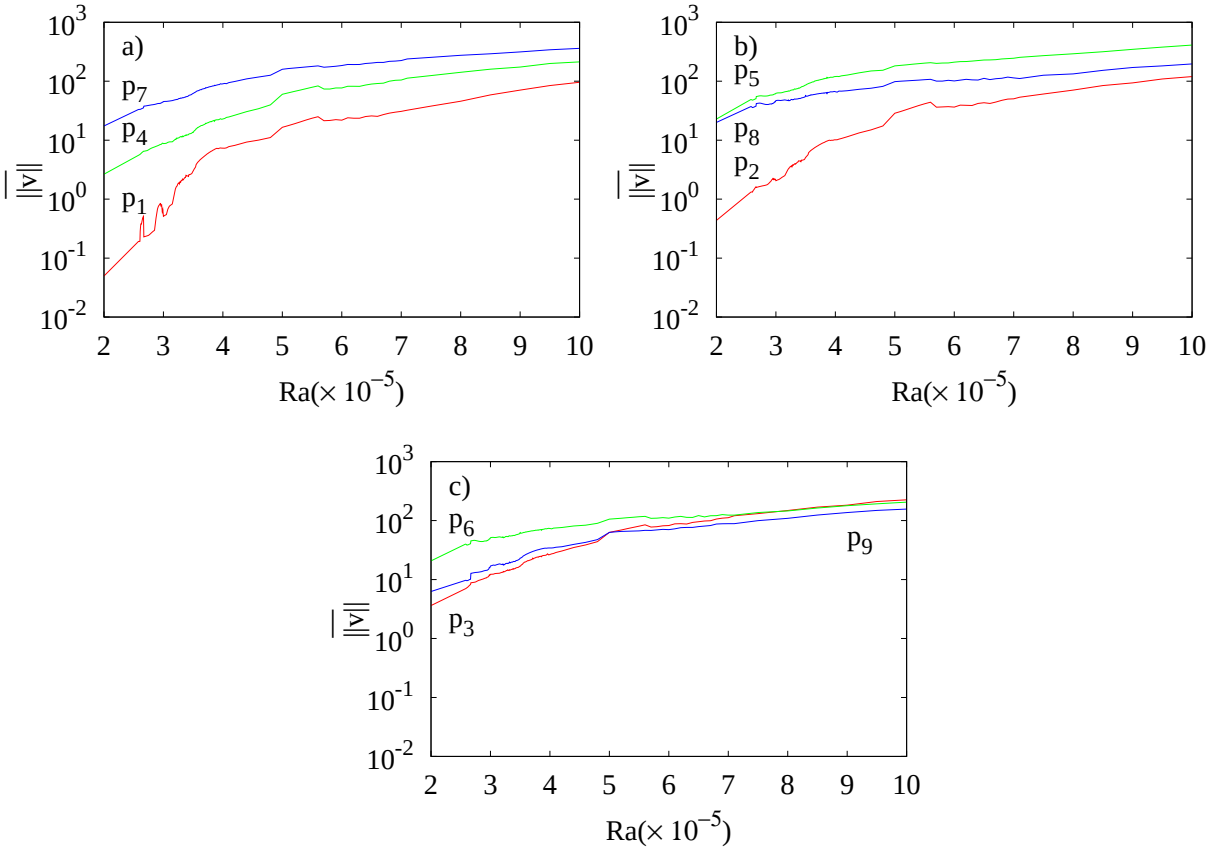

Figure 5.43: Time average of the modulus of the velocity field, $||\overline{\mathbf{v}}||$, plotted versus the Rayleigh number Ra at spherical surfaces of radius (a) $r = r_i + (r_o - r_i)/7$, (b) $r = r_i + (r_o - r_i)/2$, and (c) $r = r_i + 6(r_o - r_i)/7$. The colours mean: $\theta = \pi/8$ red, $\theta = \pi/4$ green, and $\theta = 3\pi/8$ blue.

difference between the size of positive and negative vortices. At $Ra = 3.42 \times 10^5$ both vortices are of similar size, but at higher Ra the size of the negative vortices (blue) is significantly smaller than the size of those positive (red). At the higher Rayleigh numbers, the azimuthal extend of the vortices is clearly larger than the radial one. The scale of the vortices decreases filling the shell, but some of them remain connected giving rise to large-scale structures.

The time-averaged modulus of the velocity field $||\overline{\mathbf{v}}||$ at p_i, $i = 1, \ldots, 9$, is plotted in Fig. 5.43 versus Ra. At low $Ra \approx 2 \times 10^5$, $||\overline{\mathbf{v}}||$ is similar at the points p_i, $i = 5, 7, 6, 8$, and more or less an order of magnitude greater than $||\overline{\mathbf{v}}||$ at the other points. Thus, convection is mainly localised in a cylindrical layer outside and close to the tangent cylinder. Notice that as in the case of the mean zonal flow, the Taylor-Proudman constraint is reflected in the sense that each pair of points p_3 and p_4, p_5 and p_7, and, p_6 and p_8, located at similar distance of the axis of rotation, has nearly the same $||\overline{\mathbf{v}}||$.

As Ra increases, $||\overline{\mathbf{v}}||$ increases in all p_i, but at a different rate. For instance, the increase of $||\overline{\mathbf{v}}||$ is bigger inside the tangent cylinder. The slopes of the red curves (points p_1 and p_2) in Fig. 5.43(a, b)) provide this information. However, at $Ra \approx 4 \times 10^5$ which is roughly $2Ra_c$, the rate of increase of $||\overline{\mathbf{v}}||$ is similar for all the points. Maybe, this value could be considered the critical Rayleigh number at which the polar convection defined in [127] by Eq. (2.7) gets the level of the regions outside the tangent cylinder. Our results also agree with [114] because the amplitude of convection near the poles begins to increase rapidly when $Ra \in [3Ra_c, 5Ra_c]$. Beyond $Ra \approx 6 \times 10^5$ ($O(3Ra_c)$), all the curves start to converge indicating that the regime of fully developed convection is progressively being achieved.

5.5 Numerical asymptotic limit

The physical properties computed in this section are compared with the numerical results obtained in [29] for stress-free boundary conditions. In that paper it is assumed that at low E and high Ra the viscosity is of secondary importance because the convection is maintained predominantly by the balance of buoyancy, Coriolis and inertial forces. Thus, the physical properties are expressed as a function of the modified Rayleigh number

$$Ra^* = RaE^2\sigma^{-1},$$

which does not depend on the viscosity and the thermal diffusivity. The modified Nusselt number

$$Nu^* = NuE\sigma^{-1}$$

is independent of the thermal diffusivity. For geophysical applications it is more useful to obtain the physical properties of the fluid as a function of the Rayleigh number based on the heat flux transport

$$Ra_q^* = Ra^*Nu^*,$$

instead of on the temperature contrast, which is more difficult of estimating.

In order to compare our results with [29], the differences between our dimensionless parameters (defined in Eq. (4.5), Sec. 4.2, Chapter 4) and those used in [29] must be taken into account. In this case the only difference is in the Rayleigh numbers

$$(Ra)^{\mathrm{C}} = \frac{1}{(1-\eta)}Ra, \quad (Ra^*)^{\mathrm{C}} = \frac{1}{(1-\eta)}Ra^*, \quad (Ra_q^*)^{\mathrm{C}} = \frac{1}{(1-\eta)}Ra_q^*,$$

where the super-index C indicates, from now on, a parameter as it is defined in [29]. Our definition of the physical properties such as the kinetic energy density K, the Reynolds, Re, Rossby, Ro, and Nusselt, Nu, numbers (see Table 5.1) is the same as in [29]. We have checked that Eq. (2.11) of [29] should contains the 1/2 factor like here (Eq. (5.1)) by computing some $\overline{K}$ values with stress-free boundary conditions and $\sigma = 1$.

The time averaged physical properties, the numerical resolutions, and the type of azimuthal symmetry imposed to obtain the solutions are indicated in Table 5.3. We have compared our results with those of [29] computed with $\sigma = 1$ and $\sigma = 0.3$. Notice that

Ra^*/Ra_c^*	$\overline{Re}$	$\overline{Re_p}$	$\overline{K_t/K}$	$\overline{Nu}$	σ_{K_p}	N_r	L	m_d
$E = 10^{-4}$								
1.08	15.7	8.7	0.69	1.005	≈ 0	32	54	1
1.62	41.2	19.1	0.79	1.02	0.27	32	54	1
2.69	117.5	49.1	0.82	1.10	0.04	32	54	1
5.39	258.0	105.8	0.83	1.27	0.21	32	54	1
8.08	466.1	201.0	0.81	1.64	0.22	40	64	2
10.78	678.2	311.9	0.79	2.10	0.17	50	84	2
16.16	983.9	495.6	0.75	2.84	0.16	50	84	2
26.94	1393.2	779.7	0.69	3.94	0.14	70	128	2
37.70	1677.1	983.2	0.66	4.68	0.11	70	128	2
53.88	2144.6	1303.4	0.63	5.77	0.085	80	160	2
$E = 3.162 \times 10^{-5}$								
1.26	27.7	14.1	0.74	1.008	≈ 0	32	54	2
1.57	47.7	21.8	0.79	1.018	≈ 0	32	54	2
3.14	174.5	65.1	0.86	1.1	0.30	50	84	2
6.28	449.8	161.0	0.87	1.33	0.20	50	84	2
9.42	770.7	297.0	0.85	1.71	0.17	50	84	2
12.56	1103.1	443.9	0.84	2.21	0.20	50	84	2
15.70	1359.6	572.1	0.82	2.63	0.14	50	84	2
31.40	2214.3	1008.5	0.79	4.2	0.12	70	128	2
78.50	4011.4	2113.5	0.72	7.83	0.13	80	192	2
$E = 8.165 \times 10^{-6}$								
1.21	32.5	16.7	0.74	1.006	≈ 0	50	84	4
2.77	250.7	98.8	0.84	1.12	0.40	50	84	4
5.28	604.1	220.1	0.87	1.3	0.31	70	128	4
10.41	1342.1	494.1	0.86	1.77	0.23	70	128	4
20.81	2666.2	1066.3	0.84	3.22	0.18	80	192	4
27.75	3330.5	1349.7	0.83	4.03	0.14	80	192	4
41.62	4383.9	1820.5	0.83	5.45	0.15	80	192	4

Table 5.3: Relative modified Rayleigh number Ra^*/Ra_c^*, mean Reynolds and poloidal Reynolds numbers, $\overline{Re}$ and $\overline{Re_p}$, mean ratio of the toroidal to the total KED, $\overline{K_t/K}$, mean Nusselt number, $\overline{Nu}$, relative variance of the poloidal KED, σ_{K_p}, numerical resolutions, N_r and L, and imposed m_d-fold azimuthal symmetry for three Ekman numbers.

$(Ra^*)^{\rm C}/(Ra_c^*)^{\rm C} = Ra^*/Ra_c^*$ so the comparison is straightforward. We have found larger $\overline{Re}$ and $\overline{Re_p}$ values, and smaller $\overline{Nu}$ at high Ra^*. For instance, at $E = 10^{-4}$, $\sigma = 0.1$ and $Ra^*/Ra_c^* = 53.88$ we obtain $\overline{Re} = 2144.6$, $\overline{Re_p} = 1303.4$ and $\overline{Nu} = 5.77$ while at the same E, $\sigma = 1$ and $Ra^*/Ra_c^* = 50.0$, the author of [29] obtain $\overline{Re} = 977.0$, $\overline{Re_p} = 235.0$ and $\overline{Nu} = 8.55$. At $E = 10^{-4}$, $\sigma = 0.3$, and $Ra^*/Ra_c^* = 49.5$, he obtains $\overline{Re} = 1530.0$, $\overline{Re_p} = 518.0$ and $\overline{Nu} = 6.62$. Notice that although $\sigma = 0.3$ is not far from $\sigma = 0.1$ our values of $\overline{Re}$ and $\overline{Re_p}$ are much more larger, suggesting that, at the same supercritical conditions, convection is more vigorous with non-slip boundary conditions. In order to quantify the degree of time dependence of the convection, the normalised variance of the poloidal kinetic energy density, σ_{K_p}, was obtained in [29]. At $Ra^*/Ra_c^* = 53.88$, $E = 10^{-4}$ and $\sigma = 0.1$ we obtain $\sigma_{K_p} = 0.085$ similar to $\sigma_{K_p} = 0.08$ computed there at $Ra^*/Ra_c^* = 49.5$, $E = 10^{-4}$ and $\sigma = 0.3$, and significantly smaller than $\sigma_{K_p} = 0.12$ computed there at the same E, $Ra^*/Ra_c^* = 50.0$, but with $\sigma = 1$. Thus it seems that σ_{K_p} depends more strongly on σ than on the type of boundary conditions.

Figures 5.44 and 5.45, analogous to Figs. 6 and 7 of [29], respectively, show the time averages of the physical quantities Ro, K/K_{nz}, Ro_p, Nu^*, and Ro_z as a function of Ra^*, and of Ra_q^*, respectively, for three Ekman numbers $E = 10^{-4}, 3.165 \times 10^{-5}, 8.165 \times 10^{-6}$. They are qualitatively very similar to those of [29], but quantitatively several differences can be observed due to the use of non-slip boundary conditions and the influence of σ. This influence was studied in [29] by computing also the curves for $E = 10^{-4}$ at the Prandtl numbers $\sigma = 0.3$ and $\sigma = 3$. In the following we shall compare our results for $E = 10^{-4}$ (curve of squares in Fig. 5.45) with those corresponding to $\sigma = 0.3$ in [29] (curve of stars in Fig. 11) which match with our $\sigma = 0.1$ results, in order to understand better the differences due to the different type of boundary conditions. For the analysis we take into account that in the latter figure of [29] there is a typo, and that crosses correspond to $\sigma = 3$ and stars to $\sigma = 0.3$. The starred curve of [29] falls in the range $(Ra_q^*)^{\rm C}\sigma^{-1/4} \in [2 \times 10^{-5}, 2 \times 10^{-3}]$, i.e., $(Ra_q^*)^{\rm C} \in [1.5 \times 10^{-5}, 1.5 \times 10^{-3}]$, which means that $Ra_q^*/(Ra_q^*)_c \in [4.1, 49.5]$, and

$$\overline{Ro} \in [0.0074, 0.15], \quad \overline{K/K_{nz}} \in [3, 12], \quad \overline{Ro_p} \in [0.0012, 0.052], \quad \overline{Nu^*} \in [0.00035, 0.0022],$$

while in the same relative interval, which corresponds to $Ra_q^* \in [10^{-5}, 10^{-2}]$, our physical properties give

$$\overline{Ro} \in [0.0015, 0.21],\ \overline{K/K_{nz}} \in [1.08, 1.95],\ \overline{Ro_p} \in [0.00087, 0.131],\ \overline{Nu^*} \in [0.001, 0.0058].$$

The squared points of the curve are tabulated in Table 5.3 (10 first rows), and, analogously, the starred points are in Table 4 of [29]. As has been mentioned in [29], the time-averaged Rossby number obtained only for the poloidal component of the velocity $\overline{Ro_p}$, measures the vigour of the convective vortices because the radial heat is only transported by the poloidal component. Then, our results indicate that the strength of the

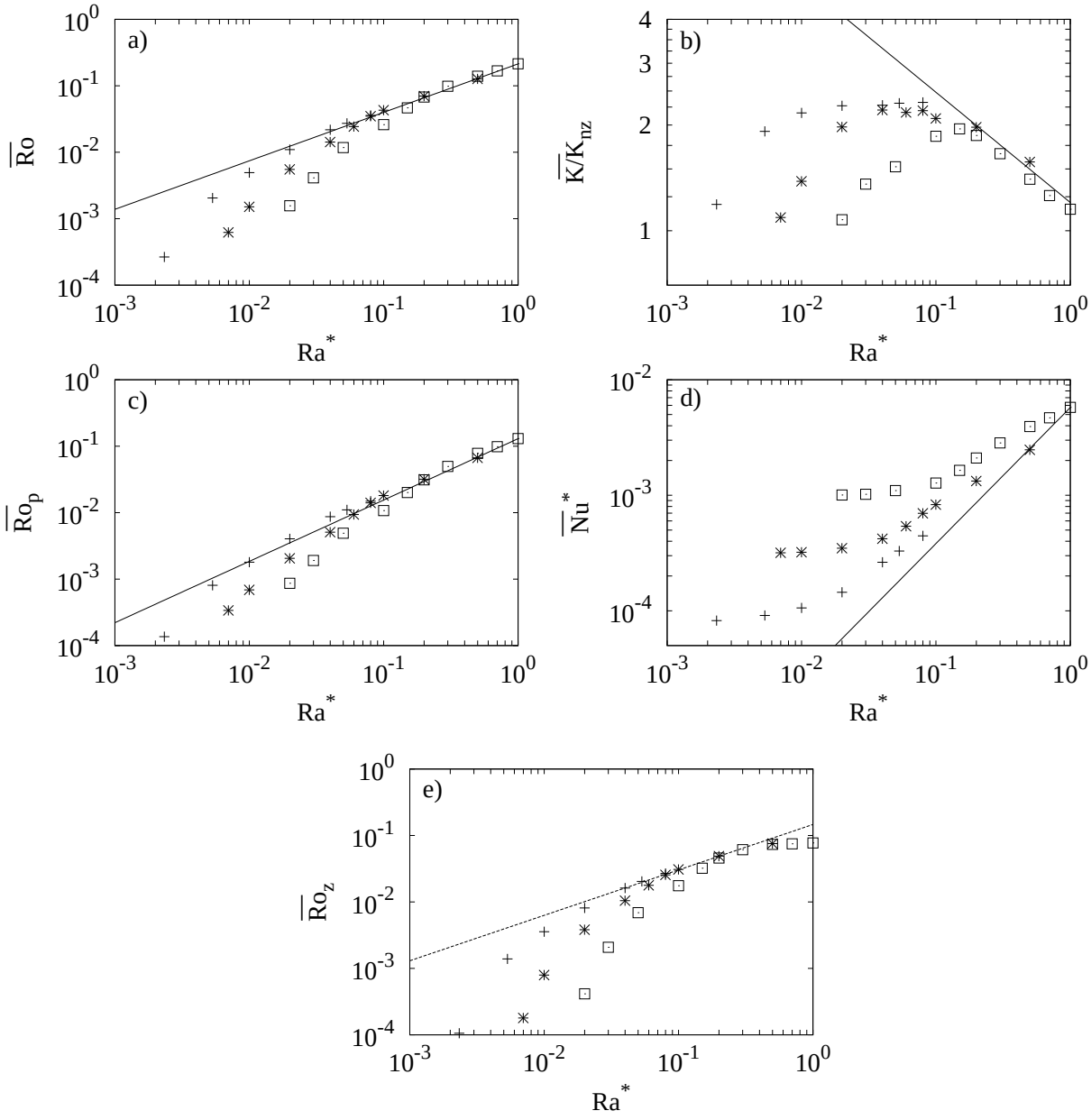

Figure 5.44: Time-averaged properties: (a) Rossby number, $\overline{Ro}$, (b) ratio of the total to the non-zonal kinetic energy densities, $\overline{K/K_{nz}}$, (c) poloidal Rossby number, $\overline{Ro_p}$, (d) modified Nusselt number, $\overline{Nu^*}$, and (e) zonal Rossby number, $\overline{Ro_z}$, versus the modified Rayleigh number, Ra^*. The symbols mean: ($\Box$) $E = 10^{-4}$, ($*$) $E = 3.165 \times 10^{-5}$ and ($+$) $E = 8.165 \times 10^{-6}$.

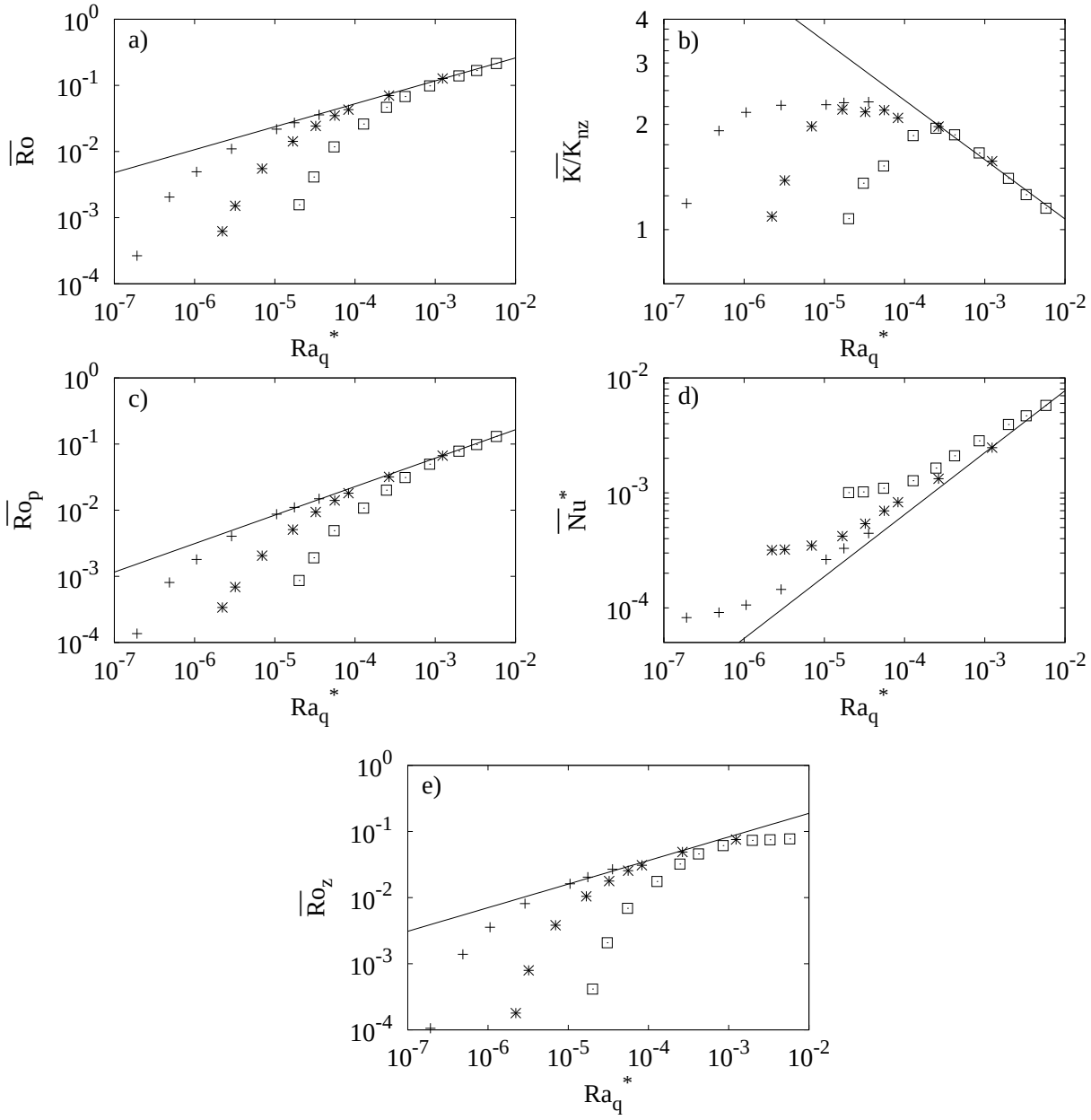

Figure 5.45: Time-averaged properties: (a) Rossby number, $\overline{Ro}$, (b) ratio of the total to the non-zonal kinetic energy densities, $\overline{K/K_{nz}}$, (c) poloidal Rossby number, $\overline{Ro_p}$, (d) modified Nusselt number, $\overline{Nu^*}$, and (e) zonal Rossby number, $\overline{Ro_z}$, versus the flux-based Rayleigh number, Ra_q^*. The symbols mean: ($\Box$) $E = 10^{-4}$, ($*$) $E = 3.165 \times 10^{-5}$ and ($+$) $E = 8.165 \times 10^{-6}$.

radial flow is larger in the case of non-slip boundary conditions with slightly smaller σ at the higher relative Rayleigh numbers. Moreover, the ratio $\overline{K/K_{nz}}$ differs significantly. Our results are clearly smaller reflecting that the contribution of the zonal flow is weak, but there are some maxima at which it is roughly the 50% of the kinetic energy density. This value is significantly larger than the $10\% - 20\%$ found in [10], also with non-slip boundary conditions at similar E and η, and Ra about six times the critical, but for $\sigma = 1$. For a fixed Ra^*/Ra_c^*, the increasing of the ratio $\overline{K/K_{nz}}$ with decreasing σ was also confirmed in [29]. This suggests that small σ values can favour zonal circulations at intermediate regimes (see Fig. 6(c) of [29]) independently of the type of boundary conditions. Finally, for most of the solutions shown in Table 5.3 the Nusselt numbers are slightly larger than those of Table 4 in [29], exept for the strongly supercritical solutions with $Ra^*/Ra_c^* > 35$. This fact indicates that the zonal flow weakens faster in the stress-free case. As $\overline{Nu^*} = \overline{Nu}E\sigma^{-1}$, and our Prandtl number is lower, we obtain always larger modified Nusselt numbers.

In Figs. 5.44 and 5.45, plotted for various E, it is observed that $\overline{Ro_z}$ tends to reach constant values for sufficiently large Ra^* and Ra_q^*, respectively. As a consequence there is a change in the sign of the slope of $\overline{K/K_{nz}}$. In [29], this change was attributed to a gradual loss of geostrophy of the flow columns, and a corresponding decorrelation of the Reynolds stresses. These latter, drive the large-scale zonal flow when the azimuthal and cylindrical radial components of the velocity field are correlated. Beyond the maximum of $\overline{K/K_{nz}}$, the regime of fully developed convection without equatorial symmetry and high heat transfer rates begins. For $E = 10^{-4}$, the maximum is close to $Ra^* = 0.15$ in Fig. 5.44, and $Ra_q^* = 3 \times 10^{-4}$ in Fig. 5.45, namely it is roughly six times the critical. The flow patterns of the solutions computed before and after the maximum were shown in Figs. 5.37 and 5.38. As in [29], for fixed Ra^* (Ra_q^*) and decreasing E, there is a convergence of the solutions in the limit $E \to 0$, and possible asymptotas are included in Fig. 5.44 (Fig. 5.45). They are computed by only taking the highest Ra^* (Ra_q^*) values of each E, except for $\overline{Ro_z}$ in which figure the region of saturation at high Ra^* (Ra_q^*) is discarded. We proceed in this way because we are interested in obtaining the extrapolation at low Ra^* (Ra_q^*) (see Sec. 5.7), and the asymptota would supply and upper bound of $\overline{Ro_z}$. The solutions at the highest Ra^* (Ra_q^*) correspond to the last row of each block of Table 5.3. The parameters and the statistical errors of the fittings $a(X)^b$, with $X = Ra^*(Ra_q^*)$, and the potential laws are shown in Table 5.4, and in Eqs. (5.2-5.6) and Eqs. (5.7-5.11), respectively.

$$\overline{Ro} = 0.21(Ra^*)^{0.73}, \tag{5.2}$$

$$\overline{K/K_{nz}} = 1.2(Ra^*)^{-0.31}, \tag{5.3}$$

$$\overline{Ro_p} = 0.13(Ra^*)^{0.92}, \tag{5.4}$$

$$\overline{Nu^*} = 0.0057(Ra^*)^{1.2} \tag{5.5}$$

$$\overline{Ro_z} = 0.15(Ra^*)^{0.68}. \tag{5.6}$$

X	Property(X)	a	$\epsilon(a)$	b	$\epsilon(b)$
Ra^*	$\overline{Ro}$	0.21	0.0027	0.73	0.026
	$\overline{K/K_{nz}}$	1.2	0.077	-0.31	0.052
	$\overline{Ro_p}$	0.13	0.0027	0.92	0.054
	$\overline{Nu^*}$	0.0057	0.00016	1.2	0.094
	$\overline{Ro_z}$	0.15	0.0072	0.68	0.024
Ra_q^*	$\overline{Ro}$	1.3	0.045	0.35	0.0061
	$\overline{K/K_{nz}}$	0.49	0.055	-0.17	0.015
	$\overline{Ro_p}$	1.2	0.023	0.43	0.0034
	$\overline{Nu^*}$	0.093	0.011	0.54	0.021
	$\overline{Ro_z}$	0.97	0.32	0.36	0.036

Table 5.4: Coefficients and their absolute errors ϵ of the potential laws $a(X)^b$, $X = Ra^*, Ra_q^*$, for the time-averaged Rossby number, $\overline{Ro}$, ratio of the total to the non-zonal kinetic energy densities, $\overline{K/K_{nz}}$, poloidal Rossby number, $\overline{Ro_p}$, modified Nusselt number, $\overline{Nu^*}$, and zonal Rossby number, $\overline{Ro_z}$.

$$\overline{Ro} = 1.3(Ra_q^*)^{0.35}, \tag{5.7}$$
$$\overline{K/K_{nz}} = 0.49(Ra_q^*)^{-0.17}, \tag{5.8}$$
$$\overline{Ro_p} = 1.2(Ra_q^*)^{0.43}, \tag{5.9}$$
$$\overline{Nu^*} = 0.093(Ra_q^*)^{0.54}, \tag{5.10}$$
$$\overline{Ro_z} = 0.97(Ra_q^*)^{0.36}. \tag{5.11}$$

Analogous power laws than those of Eqs. (5.2-5.6) and Eqs. (5.7-5.11), were given in Eqs. (3.1-3.4) and Eqs. (3.5-3.8) in [29] for $\sigma = 1$ and stress-free boundary conditions. By comparing his results for $\sigma = 0.3,\ 1$ and 3 the author found a universal power law for $(Ra_q^*)^{\mathrm{C}}\sigma^{-1/4}$. The asymptotic lines are given by his Eqs. (3.5-3.8) by replacing $(Ra_q^*)^{\mathrm{C}}$ by $(Ra_q^*)^{\mathrm{C}}\sigma^{-1/4}$. In order to determine the deviation with respect to the non-slip boundary conditions, we have computed the corresponding prefactor of the modified power laws (Eqs. 3.5-3.8) for $\sigma = 0.1$ and our Ra_q^*. It results that

$$\overline{Ro} = 0.79(Ra_q^*)^{1/5}, \tag{5.12}$$
$$\overline{K/K_{nz}} = 0.24(Ra_q^*)^{-2/5}, \tag{5.13}$$
$$\overline{Ro_p} = 0.81(Ra_q^*)^{2/5}, \tag{5.14}$$
$$\overline{Nu^*} = 0.13(Ra_q^*)^{5/9}. \tag{5.15}$$

The exponents of the power laws for $\overline{Ro_p}$ and $\overline{Nu^*}$ of Eqs. (5.9) and (5.10), agree very well with Eqs. (5.14) and (5.15), respectively. The prefactor is slightly smaller for $\overline{Nu^*}$ and slightly larger for $\overline{Ro_p}$, in agreement with the preceding comparison, i.e., at highly supercritical parameters the radial heat transport is more efficient in the stress-free case despite the larger $\overline{Ro_p}$ value of the non-slip case. As has been noticed previously, the Ra_q^* dependence of $\overline{Ro}$, and $\overline{K/K_{nz}}$ differs substantially (compare Eqs. (5.7) and (5.8) with Eqs. (5.12) and (5.13)). These differences are not surprising because the latter properties are influenced by the zonal flow, which is clearly sensible to the different types of boundary conditions. In the following section the numerical fittings obtained for the time-averaged quantities will be contrasted with scalings obtained in previous experimental studies [6, 104, 41].

5.6 Comparison with experimental results

In this section, the numerical results and the scaling laws for the physical quantities (whose definitions are summarised in Table 5.1, Sec. 5.2), obtained in the previous sections, are compared with some experimental results for liquid gallium in [6] in a set-up with our same radius ratio $\eta = 0.35$, with an experiment with liquid sodium [104], and finally, with the more recent experiment with gallium [41]. The use of non-slip boundary conditions is adequate for this comparison.

Two experimental fluids with different σ are used in [6], gallium ($\sigma = 0.027$) and water ($\sigma = 7$). For the former, which matches better with $\sigma = 0.1$, the results are obtained for $10^{-7} < E < 10^{-6}$ and $Ra_c < Ra < 10Ra_c$. Although their E is two orders of magnitude smaller than ours, some significant similarities are found. It is important to notice that our dimensionless parameters (defined in Eq. (4.5), Sec. 4.2, Chapter 4), as well as the time and length scales used to obtain our dimensionless equations, are the same as those used in [6]. Then the comparison is straightforward.

All the flow patterns described in [6] for the liquid gallium are turbulent, even at $Ra = 1.2Ra_c$. This contrast with our results in which windows of periodic and quasiperiodic motions appear in this range of Ra. This is not surprising because it is well known that the interval of Rayleigh numbers where this type of motions occur decreases as σ or E decrease. In addition, the experimental set-up is not well suited for fluids near the onset of convection, so it was difficult to find experimentally quasiperiodic motions in the low range of parameters. For the same reason, they were unable to find intermittent motions such as those shown in section 5.3.2, or those studied in [51], and [29]. Our results close the possibility, pointed out in [6], that non-slip boundary conditions prevent the system from developing intermittent flows near the onset of convection.

The measurements of [6], suggest that the radial size of the cell of convection generally increases with Ra. This occurs also for their estimates of the lateral extend of the cell. These features can be also observed in our contour plots of Secs. 5.3.6, and 5.4, at $E =$

10^{-4}. On the other hand, the time-averaged azimuthal velocity $\overline{v_\varphi}$ measured in [6], along the radial distance between the two boundaries at the equator, is retrograde near the inner cylinder, while remains prograde far away. This feature is also shared by our numerical results of the mean zonal flow $[\overline{v_\varphi}]$ (see Sec. 5.4). To quantify the convective part of the flows, the authors of [6] measured the variance of the radial component of the velocity field defined as $\sigma^*_{v_r} = \sqrt{\overline{(v_r - \overline{v_r})^2}}$, at the radial distance where it is maximum, i.e., at $r = r_{\max}$, which falls near the inner boundary. They obtain that the values of $\sigma^*_{v_r}$ and $\overline{v_\varphi}$ are comparable and both increase when E is decreased. We have observed the same behaviour between our estimates of the convective $\overline{Ro_p}$, and zonal $\overline{Ro_z}$ contributions to the flow (compare Figs. 5.44(c) and 5.44(e)), although these estimates are volume averages.

In Fig. 5.46(a), $-[\overline{v_\varphi}]^d$ in mm/s, computed near the inner boundary and close to the equator (see figure caption) is shown versus $Ra/Ra_c - 1$ for $E = 10^{-4}$, $E = 3.16 \times 10^{-5}$, and $E = 8.165 \times 10^{-6}$. Assuming that $\sigma = 0.1$ corresponds to the Prandtl number of the Earth's outer core, we take $\nu = 1 \times 10^{-6}$ m^2/s estimated by [91], to obtain the dimensional values. In addition, by considering the shell gap of the experiment $d = 0.07$ m, we get $[\overline{v_\varphi}]^d = 0.014[\overline{v_\varphi}]$ mm/s. To facilitate the comparison the measures of $-\overline{v_\varphi}^d$ for gallium at $E = 1.5 \times 10^{-6}$ and water at $E = 2.4 \times 10^{-6}$, taken from [6], are superposed in the same figure. They are taken at the equator and also near the inner boundary. In spite of dealing with global and local quantities at different E, the order of magnitude of $-[\overline{v_\varphi}]^d$ and $-\overline{v_\varphi}^d$ and the tendency of the curves are coherent. As can be seen in the figure, our curve falls between those experimental reflecting the intermediate σ value, despite the great difference in E. On the other hand, as it has been seen in Sec. 5.5, for each decreasing E there is an increasing Ra from which $-[\overline{v_\varphi}]$ remain constant, i.e. when $E \to 0$ the saturation of the solution might be delayed to $Ra \to \infty$. This phenomenon can also be identified in the local measurements of [6] (see their Fig. 8).

The set of scaling laws derived in [22], under the assumptions of negligible dissipation in the outer Ekman layer and quasi-geostrophic approximation were adopted in [6] when inertia dominates the dynamics. In particular, for the Rossby number based on the variance of the radial component of the velocity field $Ro_{\sigma^*_{v_r}} = \sigma^*_{v_r} E$, they obtain $Ro_{\sigma^*_{v_r}} \sim (Ra^*_q)^{2/5}$. Notice that $Ro_{\sigma^*_{v_r}}$ refers to a time-averaged quantity despite it does not have an overline. This fact is indicated by the subindex which refers to the variance of v_r. This power law agrees with their experimental results at $r = r_{\max}$, and also with our numerical results for $\overline{Ro_p}$, although this latter is volume-averaged. Remember that Eq. (5.9) obtained in Sec. 5.5, gives the exponent 0.43. However, in the quantification of the zonal flow the situation is different. From the equation of the time-averaged azimuthal component of the velocity the scaling law

$$|\overline{v_\varphi}| \sim (RaNu\sigma^{-2})^{4/5} E^{9/10} = (Ra^*_q)^{4/5} E^{-3/2}, \tag{5.16}$$

was derived in [6]. In order to compare with the experimental data they assumed a constant Nusselt number because no experimental data for the heat flux were available.

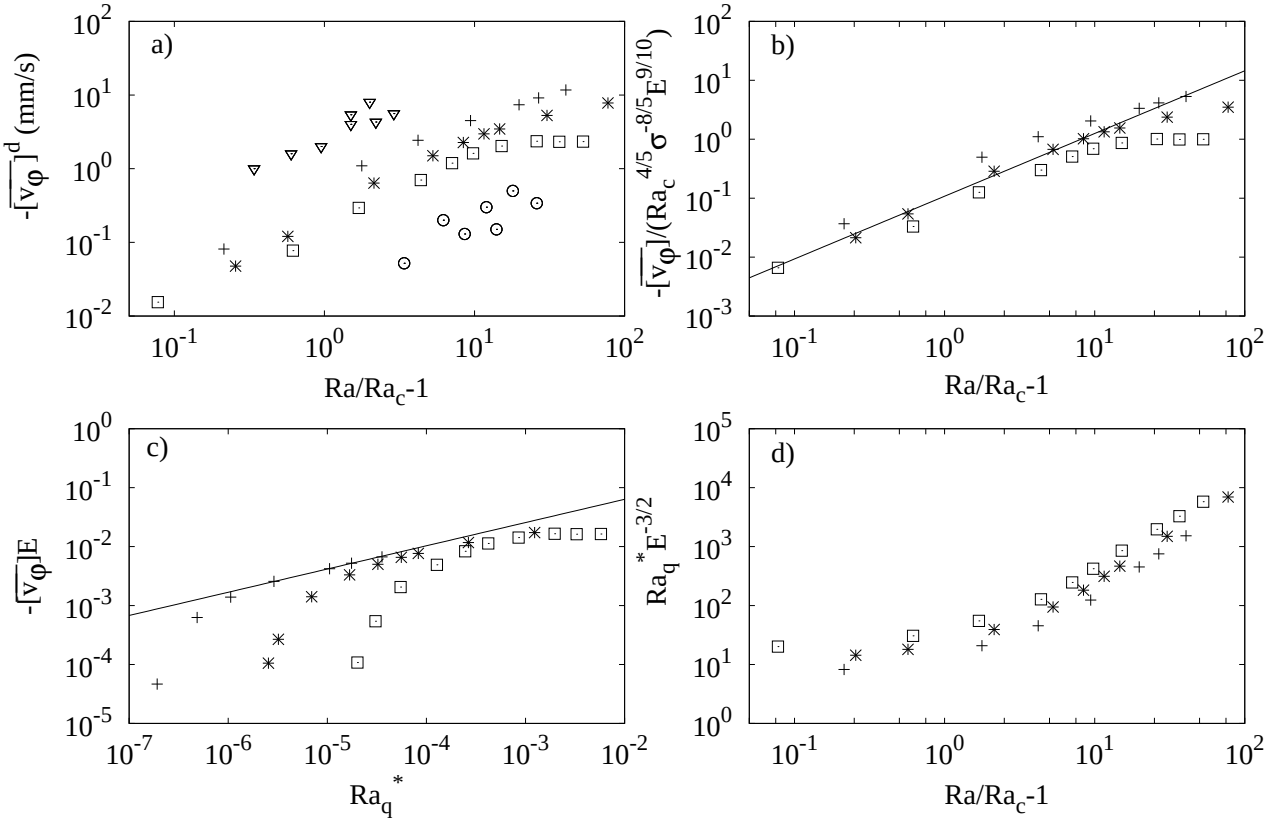

Figure 5.46: (a) Time average of the dimensional azimuthally-averaged azimuthal component of the velocity field $-[\overline{v_\varphi}]$ in millimetres per second, at $r = r_i + (r_o - r_i)/7$ and $\theta = 3\pi/8$, plotted versus $Ra/Ra_c - 1$. (b) Same as (a) but for $-[\overline{v_\varphi}]$ in dimensionless form and normalised with $Ra_c^{4/5}\sigma^{-8/5}E^{9/10}$. (c) Same as (b) but normalised with E^{-1} and plotted versus the flux-based Rayleigh number Ra_q^*. (d) Flux-based Rayleigh number Ra_q^* normalised by $E^{3/2}$ and plotted versus $Ra_c/Ra - 1$. The symbols mean: ($\square$) $E = 10^{-4}$, ($*$) $E = 3.16 \times 10^{-5}$ and ($+$) $E = 8.165 \times 10^{-6}$. Moreover, $\bigtriangledown$ and $\odot$ correspond to experimental measures of liquid gallium and water, respectively, taken from [6].

To support this approximation, they argued that variations of Nu are not dramatic when compared to those of Ra. Figure 5.46(b) shows $-[\overline{v_\varphi}]$ (at the same spherical coordinates as in Fig. 5.46(a)) normalised by $Ra_c^{4/5}\sigma^{-8/5}E^{9/10}$. The same dependence is shown in Fig. 12 of [6] but for $-\overline{v_\varphi}$ evaluated at $r = r_{\max}$ at the equator. We find a linear dependence with a prefactor of 0.1 while they found as exponent 4/5. The slope is larger in our case, but the fitting is poor (about 10% of error in the exponent and 40% in the prefactor). The region in which $[\overline{v_\varphi}]$ tends to constant is not considered in the fitting.

Our scaling relations for the mean zonal flow differ from those of the mean azimuthal

velocity given by Eq. (5.16). As can be seen in Fig. 5.46(c) we obtain

$$-[\overline{v_\varphi}]\,E \;=\; 0.4(Ra_q^*)^{0.40}, \quad \text{at} \quad r = r_i + (r_o - r_i)/7 \quad \text{and} \quad \theta = 3\pi/8. \qquad (5.17)$$

The error for the exponent is about 3% and for the prefactor about 10%. For the reasons explained before, in this case, the regression is performed by using the largest Ra_q^* points corresponding to the lowest E curve. At other radial distances (not shown in the figure) we have found

$$-[\overline{v_\varphi}]\,E \;=\; 0.1(Ra_q^*)^{0.35}, \quad \text{at} \quad r = r_i + (r_o - r_i)/2 \quad \text{and} \quad \theta = 3\pi/8, \qquad (5.18)$$

$$[\overline{v_\varphi}]\,E \;=\; 0.1(Ra_q^*)^{0.40}, \quad \text{at} \quad r = r_i + 6(r_o - r_i)/7 \quad \text{and} \quad \theta = 3\pi/8. \qquad (5.19)$$

Notice that close to the outer boundary the mean zonal flow is positive, and in modulus it is four times smaller than close to the inner boundary. From Eqs. (5.17-5.19) it is easy to see that for E and Ra_q^* tending to zero $-[\overline{v_\varphi}]$ becomes larger at $r = r_i + (r_o - r_i)/2$.

The Rossby number based on the mean zonal flow, $\overline{Ro_{[v_\varphi]}} = |[\overline{v_\varphi}]|E$ given by Eq. (5.17), exhibit a slightly different power law dependence than the time-averaged zonal Rossby number $\overline{Ro_z}$ given by Eq. (5.11) and defined in Table 5.1. The ratio of the latter to the former increases slowly from 3 at $Ra_q^* = 10^{-2}$ to 10 at $Ra_q^* = 10^{-15}$ meaning perhaps that at very low Ra_q^* values, the axisymmetric part of the poloidal component of the velocity field (which contribute to $\overline{Ro_z}$ and does not do it to $\overline{Ro_{[v_\varphi]}}$) starts to be important.

In order to check that the discrepancies between the fittings of Eq. (5.16) and Eq. (5.17) are not due to having not reached the very high Re regime, which is characterised by the conditions given in Eq. (18) of [6], the quantity $Ra_q\sigma^{-2}E^{3/2} = Ra_q^*E^{-3/2}$ is plotted versus $Ra/Ra_c - 1$ in Fig. 5.46(d). As in [6], all the values are larger than 10, which ensures the validity of the inertial regime. According to [41], Eq. (5.16) may be inadequate because the increase of the characteristic length scale is neglected, and also because the length scale is obtained from the convective instead of the azimuthal velocity.

Recently, an experiment in liquid sodium ($\sigma = 0.01$), with a set-up similar to that used in [6], was performed [104]. Ekman numbers $E^{\mathrm{S}} = E$ down to 10^{-8} and Rayleigh numbers $Ra^{\mathrm{S}} = Ra$ up to 10^9 were reached. The super-index S means values used in [104]. Notice that in Table 1 of [104] there is a typo and the Ekman number should be $E = \nu/(\Omega d^2)$. Their definition of the Rayleigh number includes the centrifugal ($\Omega^2\mathbf{r}$), instead of the gravity term ($\gamma\mathbf{r}$), because they model the gravity by the centrifugal acceleration. However, they use our definition of the Rayleigh number (Eq. (4.5) of Sec. 4.2 in Chapter 4) in their comparisons with other studies, such as [6]. Thus it seems that they are assuming $\Omega^2 = \gamma$.

Small-scale convective, as well as large-scale zonal flows, were observed in [104]. The latter being estimated from the time average of the azimuthal velocity, which they measure in m/s from temperature probes situated close to the inner surface near the equator. This time-averaged velocity will be noted by $\overline{v_\varphi}^d$, from now on. At this point they found $\overline{v_\varphi}^d$

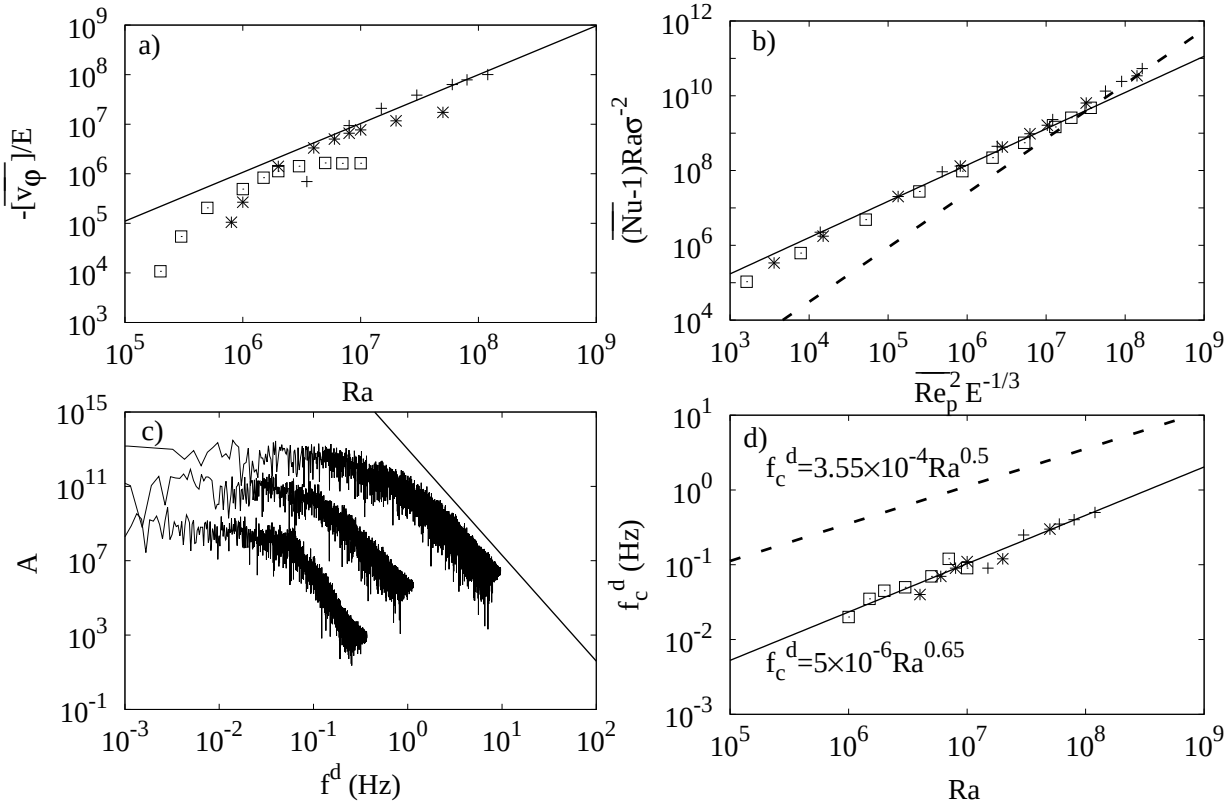

Figure 5.47: (a) Time average of the azimuthally-averaged azimuthal component of the velocity field $[\overline{v_\varphi}]$, at $r = r_i+(r_o-r_i)/7$ and $\theta = 3\pi/8$, normalised by E and plotted versus Ra. (b) The convective heat flux $(\overline{Nu}-1)Ra\sigma^{-2}$ plotted versus $\overline{Re_p}^2 E^{-1/3}$. (c) Frequency spectra of the temperature perturbation for $E = 3.16\times10^{-5}$ in Hz. They correspond, from bottom to top, to $Ra = 4\times10^6$, $Ra = 8\times10^6$, and $Ra = 5\times10^7$, respectively. (d) Knee frequency f_c plotted versus Ra. The symbols mean: $\boxdot$ ($E = 10^{-4}$), $*$ ($E = 3.16\times10^{-5}$) and $+$ ($E = 8.165\times10^{-6}$). The solid line is our fitting, and the dashed that of [104].

retrograde as occurs in our numerical results for $[\overline{v_\varphi}]$ and in the experiments of [6]. In contrast to this latter study, the authors of [104] suggest a scaling relation $|\overline{v_\varphi}| \sim Ra^{\mathrm{S}}E^{\mathrm{S}}$ by balancing Coriolis and buoyancy forces. The same relation is obtained if it is supposed that the azimuthal motions come from thermal winds. Although the exponent of Eq. (5.9) for the convective flow, $\overline{Ro_p}$, agree with [6], the exponent of our numerical fitting for the mean zonal flow (Eq. (5.20) below) agree better with those of $|\overline{v_\varphi}|^d$ given in Eq. (8) of [104]. This is shown in Fig. 5.47(a) where $-[\overline{v_\varphi}]/E$ is plotted versus Ra. The solid line corresponds to the relation

$$-[\overline{v_\varphi}] \;=\; 1.3RaE, \quad \text{at} \quad r = r_i + (r_o - r_i)/7 \quad \text{and} \quad \theta = 3\pi/8. \tag{5.20}$$

and at other radial distances (not shown in the figure)

$$-[\overline{v_\varphi}] = 0.04Ra^{1.15}E, \quad \text{at} \quad r = r_i + (r_o - r_i)/2 \quad \text{and} \quad \theta = 3\pi/8, \tag{5.21}$$

$$[\overline{v_\varphi}] = 0.3RaE, \quad \text{at} \quad r = r_i + 6(r_o - r_i)/7 \quad \text{and} \quad \theta = 3\pi/8. \tag{5.22}$$

The first law can be compared with $|\overline{v_\varphi}|^d = (7\kappa/d)Ra^{\rm S}E^{\rm S}$, derived in [104]. Notice that in this formula there is a factor 2 with respect their Eq. (8), which has a typo. In viscous units for $\sigma = 0.01$ it gives $|\overline{v_\varphi}| = 350Ra^{\rm S}E$. Although the relation of $|\,[\overline{v_\varphi}]\,|$ and $|\overline{v_\varphi}|$ with Ra and E is the same, the comparison reflects the dependence of the zonal flows on σ. Other factors that can contribute to the difference are that $|\,[\overline{v_\varphi}]\,|$ is an azimuthally averaged quantity, and $|\overline{v_\varphi}|$ is not, the probe is located closer to the inner sphere than our results, and the perturbation introduced by axis of rotation in the experiment. Notice that Eq. (5.21) indicates again the strong strength of the mean zonal flow in the centre of the shell at high Ra.

Up to now two different scalings for the mean zonal flow (Eq. (5.17) and Eq. (5.20)) have been obtained but, as it will next be shown, they are consistent despite the not very accurate determination of the fittings. If they are rewritten as a function of Ra^* one can check that both are consistent. Equation (5.20) is equivalent to $y_1 = -[\overline{v_\varphi}]E = 1.3\sigma Ra^*$, and by using Eq. (5.5), Eq. (5.17) transforms into $y_2 = -[\overline{v_\varphi}]E = 0.05(Ra^*)^{0.88}$. It is easy to see that $y_1/y_2 \approx 26\sigma(Ra^*)^{0.12}$, and that for $\sigma = 0.1$, $y_1/y_2 \in [0.1, 10]$ for the wide range of $Ra^* \in [10^{-12}, 10^5]$, y_1/y_2 being nearly the unity close to $Ra^* = 10^{-4}$. So, both laws are compatible. This range includes the values of Fig. 5.44 and, as it will shown in next section, values similar to those of the Earth's outer core conditions.

Another feature that our results share with those of [104] and also [75] is that, for each E computed, the zonal contribution of the flow saturates at the highest Ra. This tendency remains clear in the mean zonal flow of Figs. 5.46(a, b, c), and Fig. 5.47(a), and is clearly exhibited by the curves corresponding to the larger E (see the $E = 10^{-4}$ curves). This is also confirmed by the saturation of $\overline{Ro_z}$, and by the decreasing of the ratio $\overline{K/K_{nz}}$ in Figs. 5.44 or 5.45, corresponding to high Ra^* and Ra_q^* values. Then, when using the mean zonal flow scalings (Eq. (5.17) or Eq. (5.20)) to extrapolate real geophysical values, the results must be taken as an upper bound.

As was mentioned in [6] or in [104], low σ fluids are not suitable for heat transfer. In the latter experiments with liquid sodium the Nusselt number never exceeds 2. In our case, at a slightly larger $\sigma = 0.1$, $\overline{Nu}$ is always lower than 8 (see Table 5.3) and very similar to that shown in Table 4 of [29] for $\sigma = 0.3$ and stress free boundary conditions. Following [49, 105] the scalar relation $(Nu^{\rm S} - 1)Ra^{\rm S}\sigma^{-2} \sim (Re^{\rm S})^2(E^{\rm S})^{-1/3}$ was derived in [104] for the convective heat flux. It was obtained by balancing the global and the local energy dissipation of the convective cells using an estimation of the convective cell size at the onset. When they assume $Re^{\rm S} = U^{\rm S}d/\nu$, being $U^{\rm S} = \Omega d\sqrt{\alpha\Delta T}$ their estimation of the convective velocity, the relation agreed with their experimental results of the convective heat flux. It was measured at the outer part of the apparatus at mid latitudes. However,

they do not give the prefactor of the fitting and thus we can only compare the exponents. In terms of our dimensionless parameters the above relation reads $(\overline{Nu}-1)Ra\sigma^{-2} \sim \overline{Re_p}^2 E^{-1/3}$. We have checked this scaling from Fig. 5.47, where $(\overline{Nu}-1)Ra\sigma^{-2}$ is plotted versus $\overline{Re_p}^2 E^{-1/3}$. The results agree with those of [104] at small and moderate $\overline{Re_p}$, when the slope of the solid line is is 0.98 with 9% of error (the prefactor is 218 with an error of 40%), but we predict a larger increase at high $\overline{Re_p}E^{-1/3}$. For these values the relation estimated from the dashed line is

$$(\overline{Nu}-1)Ra\sigma^{-2} = 4\times 10^{-2}(\overline{Re_p}^2 E^{-1/3})^{1.45}. \tag{5.23}$$

One source of the differences could come from the dependence of the heat transfer on the latitude [104]. In our results the convective heat transfer in Fig. 5.47 is taken over the whole outer boundary including the polar region, where convection is strongly developed at high $\overline{Re_p}$. Notice that in Fig. 5.44 $\overline{Nu^*}$ increases rapidly at high Ra^*. In addition the design of the apparatus prevents the development of convection in the polar regions while in the numerical simulations this effect is not present. Finally it must be mentioned that our numerical results are computed by imposing m_d-fold symmetry. All these differences could explain the discrepancies found in both analysis. On the other hand, making use of the definition of Ra_q^* and assuming $\overline{Nu} \approx \overline{Nu}-1$ at high $\overline{Re_p}$, Eq. (5.23) can be transformed into

$$\overline{Ro_p} \approx 3(Ra_q^*)^{0.35}E^{0.13}, \tag{5.24}$$

which is different from the scaling of Eq. (5.9) obtained in Sec. 5.5. Let us analyse in more detail both scalings to see if they are compatible. Let y_1 and y_2 be the values of $\overline{Ro_p}$ corresponding to Eq. (5.24) and Eq. (5.9), respectively. Then $y_1/y_2 \approx 0.4(Ra_q^*)^{0.08}E^{-0.13}$. It is easy to see that for the small realistic E, $y_1/y_2 \in [0.33, 3]$ for a wide range of Ra_q^*, including the values of Fig. 5.45. Therefore both scalings would give similar $\overline{Ro_p}$ values. For instance, at $E = 8.165\times 10^{-6}$, $y_1/y_2 \in [0.33, 3]$ for $Ra_q^* \in [5\times 10^{-10}, 4\times 10^2]$, and $y_1/y_2 = 1$ at $Ra_q^* = 5\times 10^{-4}$. At very low $E = 10^{-15}$, $y_1/y_2 \in [0.33, 3]$ for $Ra_q^* \in [5\times 10^{-26}, 5\times 10^{-14}]$, and $y_1/y_2 = 1$ at $Ra_q^* = 10^{-19}$.

In contrast to our experience, and as in [6], periodic or quasiperiodic motions were not found in the sodium experiments [104]. They obtained always non-periodic frequency spectra from the time series of temperature probes taken close to the inner boundary and at the equator. These spectra present a sharp change of slope at the critical frequency $f_c = 2.0\Omega\sqrt{\alpha\Delta T}$ (knee frequency). In Fig. 5.47(c), three frequency spectra for the temperature perturbation Θ are shown. From bottom to top, they are plotted at $Ra = 4\times 10^6$, $Ra = 8\times 10^6$, and $Ra = 5\times 10^7$, for fixed $E = 3.16\times 10^{-5}$. In this case, a softer change of slope towards the high frequencies, but also close to -5.7 (marked by the solid line), can be appreciated. The knee frequency also increases with Ra, however the rate of increase, for moderate σ, is larger than that for $\sigma = 0.01$. In Fig. 5.47(d) the knee frequency f_c is plotted versus Ra for the non-periodic solutions, and the values are shown in Table 5.5.

$E = 10^{-4}$			$E = 3.162 \times 10^{-5}$			$E = 8.165 \times 10^{-6}$		
Ra/Ra_c	f_c^d	S_θ	Ra/Ra_c	f_c^d	S_θ	Ra/Ra_c	f_c^d	S_θ
1.08	?	1	1.26	?	1	1.21	?	1
1.62	?	1	1.57	?	1	2.77	?	1
2.69	?	1	3.14	?	1	5.28	0.09	1
5.39	0.02	1	6.28	0.04	1	10.41	0.25	0
8.08	0.035	0	9.42	0.07	0	20.81	0.35	0
10.78	0.045	0	12.56	0.09	0	27.75	0.4	0
16.16	0.05	0	15.70	0.11	0	41.62	0.5	0
26.94	0.07	0	31.40	0.12	0			
37.70	0.12	0	78.50	0.3	0			
53.88	0.09	0						

Table 5.5: Relative Rayleigh number Ra/Ra_c, dimensional knee frequency $f_c^d = (\nu/d^2) f_c$ with $\nu = 10^{-6}$ m^2 s^{-1} and $d = 0.2$ m, and equatorial symmetry ($S_\theta = 1$ equatorially symmetric and $S_\theta = 0$ without equatorial symmetry), for three Ekman numbers. The critical Rayleigh numbers Ra_{sb} of the symmetry breakings satisfy: $Ra_{sb} \in [10^6, 1.5 \times 10^6]$ for $E = 10^{-4}$, $Ra_{sb} \in [4 \times 10^6, 6 \times 10^6]$ for $E = 3.162 \times 10^{-5}$, and $Ra_{sb} \in [1.5 \times 10^7, 3 \times 10^7]$ for $E = 8.165 \times 10^{-6}$.

The points fit to dimensional (Hz) law

$$f_c^d = 5 \times 10^{-6} Ra^{0.65}, \quad \text{at} \quad r = r_i + (r_o - r_i)/7 \quad \text{and} \quad \theta = 3\pi/8, \tag{5.25}$$

represented by the solid line. We obtain 5% of error in the exponent, and 50% in the prefactor. These errors are not excessive because of the uncertainty in determining f_c over figures like Fig. 5.47(c). With the error propagation, that of f_c can reach more than 100%.

We have found some variation of the frequency with the radial distance for this turbulent flows, part of which perhaps can be due to the uncertainty introduced by the large errors

$$f_c^d = 6 \times 10^{-6} Ra^{0.6}, \quad \text{at} \quad r = r_i + (r_o - r_i)/2 \quad \text{and} \quad \theta = 3\pi/8, \tag{5.26}$$

$$f_c^d = 5 \times 10^{-5} Ra^{0.45}, \quad \text{at} \quad r = r_i + 6(r_o - r_i)/7 \quad \text{and} \quad \theta = 3\pi/8. \tag{5.27}$$

In this case the exponents are obtained with 8% of error, but that for the prefactor reach 50%.

The knee frequency of [104] in terms of our parameters is $f_c^d = 2\nu(\sigma^{-1} Ra)^{1/2}/d^2$ (Hz). By using $\sigma = 0.01$, $\nu = 7.1 \times 10^{-7}$ m^2/s and $d = 0.2$ m, corresponding to the liquid sodium experiment gives

$$f_c^d = 3.55 \times 10^{-4} \sqrt{Ra}. \tag{5.28}$$

It is included in Fig. 5.47(d). In the range of parameters studied it is one order of magnitude higher in the experiment. The authors of [104] suggested that f_c marks the primary frequency at which the energy, not fully dissipated by the convective vortices, is injected into the largest scales. Then by means of the large-scale flows it is also dissipated in the viscous boundary layers. As can be seen in Table 5.5 and Figs. 5.37 and 5.38, the equatorial symmetry breaking of the flow, and the fully developed convection at very high latitudes, can be related with the existence of the knee frequency in the spectrum.

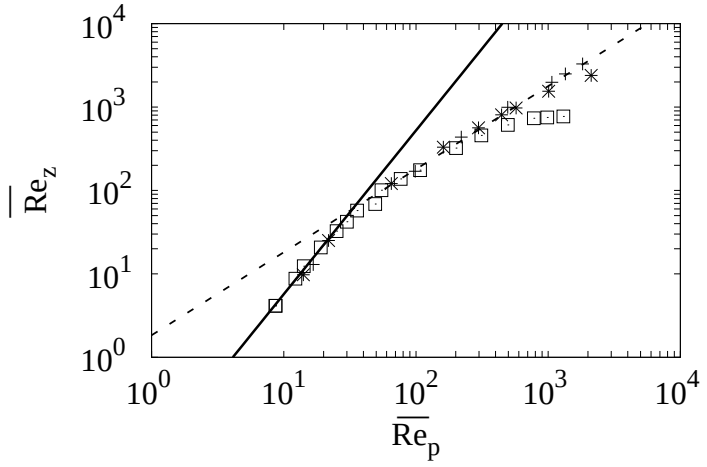

Figure 5.48: Time-averaged zonal Reynolds number plotted versus the time-averaged poloidal Reynolds number. The symbols mean: ($\Box$) $E = 10^{-4}$, ($*$) $E = 3.16 \times 10^{-5}$ and ($+$) $E = 8.165 \times 10^{-6}$.

Finally, a last comparison with a gallium experiment [41], checked by the own authors with quasi-geostrophic numerical simulations, is performed. At weak supercritical regimes, they found a quadratic dependence between the volumetric root-mean-squared radial and zonal velocities defined in Table 3 of [41] as $\tilde{U} = \left[\frac{1}{\mathcal{V}}\int_{\mathcal{V}}(\sigma^*_{v_r})^2\, dv\right]^{1/2}$ and $\overline{U} = \left[\frac{1}{\mathcal{V}}\int_{\mathcal{V}}(\overline{v_\varphi})^2\, dv\right]^{1/2}$, where $\overline{v_\varphi}$ is the time-averaged azimuthal velocity and $\sigma^*_{v_r}$ is the absolute variance defined previously. In this situation the quadratic dependence of the azimuthal motions reflects that the flow is driven by the Reynolds stresses, and the characteristic length scale corresponds to that determined at the onset of convection. Conversely, in the turbulent experiments, the authors derive a theoretical 4/3 power law for the zonal and non-axisymmetric velocities. The scaling was obtained supposing that zonal and non-zonal energy densities (see [41]) are of the same order. In this situation, and assuming a two-dimensional nature of the flow, the characteristic length scale is explained in terms of Rhines theory (see introduction of [41] and references therein). It corresponds to the scale at which the energy is transferred to the zonal flow by Rossby wave vortex interaction. As it is mentioned in [41], this scale is associated with the knee frequency f_c of Eq. (5.25)

or Eq. (29) of [104], and it depends on the magnitude of the external friction scale, which tends to damp down the growth of the zonal flow.

To compare with [41] we will quantify zonal motions using the mean zonal Reynolds number defined in Table 5.1 because our mean zonal flow $[\overline{v_\varphi}]$ is only averaged in longitude and time. The difference with [41] is that they average only the azimuthal component of the velocity. As mentioned in Sec. 5.5, the strength of our convective flow will be estimated from the mean poloidal Reynolds number, instead from the volumetric average of $\sigma^*_{v_r}$.

Figure 5.48 shows the mean zonal Reynolds number $\overline{Re_z}$, plotted versus the mean poloidal Reynolds number $\overline{Re_p}$, for the three Ekman numbers. In the figure two different regimes can be mainly identified. According to [41], in weak supercritical conditions $\overline{Re_p} \in [1, 30]$, the dependence shown by the solid line is quadratic $\overline{Re_z} = 0.05(\overline{Re_p})^{1.96}$, within a 7% of error for the exponent and 50% for the prefactor. In this case, non-zonal dominate over zonal motions, as can be seen in the ratio $\overline{K/K_{nz}}$ of Figs. 5.44 and 5.45. However, for values $\overline{Re_p} > 30$ we have obtained $\overline{Re_z} = 2\overline{Re_p}$ within 5% of error for the exponent, and 40% for the prefactor (dashed line). This linear relation differs from the 4/3 power law obtained in [41].

In the solutions belonging to this regime, the zonal contribution starts to be important and thus the ratio $\overline{K/K_{nz}}$ of Figs. 5.44 and 5.45 reaches the highest values. At sufficiently high $\overline{Re_p}$, the mean zonal Reynolds number $\overline{Re_z}$ seems to reach constant values for each E, as happens for the mean zonal Rossby number of Figs. 5.44 and 5.45 and for the mean zonal flow in Figs. 5.46 and 5.47. The dependence shown at low $\overline{Re_p}$ agrees with the scaling proposed by [41], however, they do not observe the linear dependence and the tendency towards saturation of $\overline{Re_z}$ at high $\overline{Re_p}$.

Figure 5.48 is analogous to Fig. 10 of [29] computed with stress-free boundary conditions, $\sigma = 1$ and only $E = 10^{-4}$. The change of quadratic dependence, from weak to high supercritical regimes, was also found in [29]. As mentioned in Sec. 5.5, this fact was attributed in [29] to a decorrelation of the Reynolds stresses due to a gradual lost of geostrophy. However, this explanation is declined in [41], because they observed the change of slope (from 2 to 4/3), and this effect is not possible in their quasi-geostrophic model. In our three-dimensional simulations, we have found the same quadratic relation as the quasi-geostrophic model [41], but our (and also that of [29]) change of slope is from 2 to 1. It is worth mentioning that the linear relation breaks down when the equatorial symmetry of the solutions is lost. Then the slope of the ratio $\overline{K/K_{nz}}$ becomes negative (see Table 5.5 and Figs. 5.44(b) and 5.45(b)).

5.7 Estimations for the Earth's outer core

In this section, some of the scalings obtained in Secs. 5.5 and 5.6 are used to extrapolate values for the Earth's outer core. Following [6] the flux-based Rayleigh number Ra^*_q is

obtained from the total heat flux at the core-mantle boundary (CMB), Q, that according to [52] falls in the range [1,10] TW. For $Q = 5$ TW, physical coefficients given in the first column (GSN12) of Table 5.6 and taken from [116, 91, 52], radial width of the Earth's outer core $d = 2.3 \times 10^6$ m, Earth's radius at the CMB, $r_{CMB} = 3.5 \times 10^6$ m, and $\gamma = 1.54 \times 10^{-6}$ s^{-2},

$$Ra_q = \frac{\alpha\gamma r_{CMB} Q d^2}{k\kappa\nu}, \tag{5.29}$$

gives $Ra_q \approx 3.5 \times 10^{30}$. On the other hand, taking into account the estimated Ekman number for the Earth's outer core $E = 2.6 \times 10^{-15}$ it results that $Ra_q^* \approx 4.3 \times 10^{-12}$.

The mean Reynolds and Rossby numbers, $\overline{Re}$ and $\overline{Ro}$, respectively, the mean dimensional velocity $\overline{U} = \nu/d\overline{Re}$, together with their poloidal, $\overline{U_p}$, and zonal, $\overline{U_z}$, contributions, and the mean zonal flow $|[\overline{v_\varphi}]^d|$ at $r = r_i + (r_o - r_i)/7$ and $\theta = 3\pi/8$, are estimated and their order of magnitude is included in the first column (GSN12) of Table 5.7. Notice in that table that the values for the estimators of the zonal flow, such as $|[\overline{v_\varphi}]^d|$, $\overline{Ro_z}$, etc..., are in fact upper bounds (see Secs. 5.5 and 5.6).

In addition the orders of magnitude of the above mean quantities are compared with the global Reynolds number, Re^{A}, the dimensional variance of the radial velocity, $(\sigma^a_{v_r})^d$, and the dimensional mean zonal flow, $|\overline{v_\varphi}|^d$ obtained by [6], and with the convective-based Reynolds number Re^{S} and the convective dimensional velocity U^{S} obtained by [104]. This comparison is summarised in Table 5.7.

Property	GSN12	ABNCM01	SL05
Q (TW)	5	10	–
ν (m^2/s)	10^{-6}	7×10^{-6}	10^{-6}
κ (m^2/s)	8.6×10^{-6}	4×10^{-6}	5×10^{-6}
α (K^{-1})	1.3×10^{-5}	–	–
K (Wm^{-1}K^{-1})	60	–	–
d (m)	2.3×10^6	2.26×10^6	2×10^6
E	2.6×10^{-15}	10^{-14}	10^{-15}
σ	0.12	1	0.2
Ra_q	3.5×10^{30}	10^{30}	–

Table 5.6: Physical coefficients and parameters used in the predictions for the Earth's outer core ($\eta = 0.35$). In column GSN12 the parameters are taken from [52], in ABNCM01 from [6], and in SL05 from [104].

By using Eq. (5.7) and $\overline{Ro} = \overline{Re}E$, $\overline{Re} \approx 5.2 \times 10^{10}$ is obtained. It is two orders of magnitude larger than $Re^A \approx 10^8$ given in [6], respectively. One of the sources of this difference is that our Ekman number is one order of magnitude smaller. However, our results agree better by considering only the poloidal part of the velocity field as a measure

Property	GSN12	ABNCM01	SL05
$\overline{Ro}$	10^{-4}	–	–
$\overline{Re}$	10^{10}	–	–
$\overline{U}$ (m/s)	10^{-2}	–	–
$\overline{Ro_p}$	10^{-5}	–	–
$\overline{Re_p}$	10^{9}	–	–
Re^{A}	–	10^{8}	–
Re^{S}	–	–	10^{8}
$\overline{U_p}$ (m/s)	10^{-3}	–	–
U^{S} (m/s)	–	–	10^{-4}
$(\sigma^a_{v_r})^d$ (m/s)	–	10^{-3}	–
$\overline{Ro_z}$	$\leq 10^{-5}$	–	–
$\overline{Re_z}$	$\leq 10^{10}$	–	–
$\overline{U_z}$ (m/s)	$\leq 10^{-2}$	–	–
$\lvert[\overline{v_\varphi}]^d\rvert$ (m/s)	$\leq 10^{-3}$	–	–
$\lvert\overline{v_\varphi}\rvert^d$ (m/s)	–	10^{-2}	10^{-4}
$\overline{K/K_{nz}}$	10	–	–
$\overline{U_z}/\overline{U_p}$	≤ 1	–	–
$\lvert\overline{v_\varphi}\rvert^d/U^{\mathrm{S}}$	–	–	1
$\lvert\overline{v_\varphi}\rvert^d/(\sigma^a_{v_r})^d$	–	10	–
Ra	10^{23}	–	10^{22}
Ra^*_q	10^{-12}	–	–

Table 5.7: Comparison of the order of magnitude of some physical properties and parameters for the Earth's outer core for the authors of Table 5.6. The definitions of the physical properties are summarised in Table 5.1, and Re^{A} and Re^{S} are the Reynolds numbers got by [6] and [104], respectively.

of the convective flow. From Eq. (5.9) we obtain $\overline{Re_p} \approx 6.0 \times 10^9$, and taking into account our values for ν and d, our dimensional poloidal velocity gives $\overline{U_p} \approx 2.6 \times 10^{-3}$ m/s, which is of the same order as the value $(\sigma^a_{v_r})^d \sim 10^{-3}$ m/s predicted in [6]. In contrast the convective-based Re^{S} estimated by [104] agree with Re^A, and is one order of magnitude smaller than the ours. There is the same difference between their U^{S} and our $\overline{U_p}$ or $(\sigma^a_{v_r})^d$.

Our two estimators for the strength of the zonal flows are $\overline{U_z}$ and $|[\overline{v_\varphi}]^d|$. With $\overline{Ro_z}$ given by Eq. (5.11), $\overline{U_z} \approx 1.3 \times 10^{-2}$ m/s, which is consistent with $|\overline{v_\varphi}|^d \sim 10^{-2}$ m/s obtained in [6]. In the latter work, the ratio $|\overline{v_\varphi}|^d/(\sigma^a_{v_r})^d = O(10)$ is larger than ours $\overline{U_z}/\overline{U_p} \approx 5 = O(1)$. However, [64] found from geophysical observations that zonal velocities lower than the convective should be expected. This could be explained by the fact that, for each E, the zonal flow tends to saturate at high supercritical Ra and, as it was

mentioned in the previous sections, the scalings for the zonal flow are in fact an upper bound.

On the other hand, the dimensional mean zonal flow $|[\overline{v_\varphi}]^d| \approx 1.9\times10^{-3}$ m/s is obtained from Eq. (5.17), and is one order of magnitude lower than U_z. As it was mentioned in the previous section, U_z contains the poloidal contribution, which is not present in $|[\overline{v_\varphi}]^d|$, and becomes noticeable at sufficiently low Ra_q^* (E very low). In addition, U_z is volume-averaged, $|[\overline{v_\varphi}]^d|$ is taken in a point which maximises its value, and there are important the errors in their potential fittings .

Notice that the mean zonal flow hardly exceeds by a factor 4 the value 5×10^{-4} m/s, estimated from the westward drift of the secular variation of the magnetic field, i.e., approaches rather well the *real* value. This approach is nearly exact near the CMB, where we have obtained, from Eq. 5.19, $|[\overline{v_\varphi}]^d| \approx 4.8 \times 10^{-4}$ m/s. Finally, it is important to remark that the mean zonal flow, $|[\overline{v_\varphi}]^d|$, and the poloidal velocity, $\overline{U_p}$, are of the same order. Specifically, we obtain $|[\overline{v_\varphi}]^d|/\overline{U_p} \approx 0.73$ which approaches well the observations of [64].

Our estimations of the Rayleigh number can be compared with $Ra = 3 \times 10^{22}$ (here without typo) that [104] calculated from $|\overline{v_\varphi}|^d = 5\times10^{-4}$ m/s, which is the value estimated from the westward drift of the secular variation of the magnetic field. By using this data (or 4.8×10^{-4}) and Eq. (5.20), $Ra = 3.4 \times 10^{23}$ is obtained. Although it is one order of magnitude higher than the former it remains of the same order than $Ra = 10^{23}$ predicted in a recent study [80].

Taking into account Eqs. (5.25-5.27), the kinematic viscosity, the radial width of the Earth's outer core (see Table 5.6) and the above predicted Ra, a large variation with the radial distance of the estimated knee frequency for the core, f_c^c, close to equatorial latitudes, is obtained. Specifically, $f_c^c \approx 7.5 \times 10^{-5}$ Hz, near the inner boundary, $f_c^c \approx 6.0\times10^{-6}$ Hz in the middle of the shell, and $f_c^c \approx 1.5\times10^{-8}$ Hz close to the outer boundary, is found. Notice that we have obtained time scales for the convective motions ranging from 4 hours near the inner boundary to 2 years in the outer. According this result it seems that the energy is injected into the flow at different time scales depending on the radial distance. The first frequency is more than two orders of magnitude larger than 10^{-7} given in [104], and calculated with the data also given in Table 5.6 and $Ra = 3 \times 10^{22}$, therefore their characteristic time is 174 times higher than the ours.

If f_c^c is associated with the time scale of the convective vortices it is possible to estimate their longitudinal length scale by taking into account that $\overline{U_p} \approx 2.6\times10^{-3}$ m/s. It results that near the inner sphere $\delta_c^r \sim 35$ m, in the middle of the shell $\delta_c^r \sim 435$ m, and in the outer part $\delta_c^r \sim 175$ Km. The latter value is one order of magnitude larger than the 10 Km estimated by [6] for motions near the CMB from their inertial scaling (although the convective velocities are of the same order in both studies). In addition, if the frequency of the fluctuations is due to advection of the spatial structures in the fluid, as it is supposed in [104], the length scale of the structures can be estimated by using the mean zonal flow given by Eqs. (5.17-5.19). We have $|[\overline{v_\varphi}]^d| \approx 1.9 \times 10^{-3}$ m/s, $|[\overline{v_\varphi}]^d| \approx 1.8 \times 10^{-3}$

m/s, and $|[\overline{v_\varphi}]^d| \approx 4.8 \times 10^{-4}$ m/s which gives $\delta_c^\varphi \approx 2.5 \times 10^1$ m, $\delta_c^\varphi \approx 3.0 \times 10^2$ m, and $\delta_c^\varphi \approx 3.2 \times 10^4$ m, close to the inner boundary, in the middle of the shell, and close to the outer boundary, respectively. The length scale determined by [104] is $\delta_c \sim 1$ Km, up two orders of magnitude larger than our length scales near the inner boundary and in the middle of the shell, however our results near the CMB agree very well with those of [6].

5.8 Conclusions

Two different regimes of thermal convection in fast rotating spherical shells are deeply studied along this chapter. They are the regime of oscillatory convection and the regime of fully developed convection without equatorial symmetry. The model and the parameters have been set as similar as possible to those of the Earth's outer liquid core and previous experimental studies. Non-slip boundary conditions and low Prandtl numbers were poorly considered in previous numerical studies due to the amount of numerical effort, needed to solve the Ekman layers. The use of efficient time integration methods (Chapter 4), has been determinant for integrating the low temporal scales exhibited by the flows at low E.

The changes of the time-averaged physical properties, the relative importance of the different modes which contribute to convection, and the structure of the flow patterns, have been addressed and commented. It is found that with increasing Ra, the azimuthal wave number that retains most of the total norm of the solution, tends to decrease. As has been commented, this agree with the known fact that large-scale cells are preferred at high Ra. A similar behaviour occurs through a sequence of bifurcations in a rotating annulus of [26] at $\sigma = 1$. At the highest Ra the solutions are strongly chaotic in space and time, breaking the equatorial symmetry.

In the oscillatory regime, convection is characterised by low heat transfer rates, and is strongly geostrophic. Quasiperiodic 2 and 3-tori, in some cases resonant, bifurcated from $m = 6$ and 5 travelling waves are obtained. In the case of the 2-tori, an abrupt increase of the zonal circulations occurs due the connection between the convective cells. The contribution of the zonal flow decreases when a third frequency appears giving rise to the 3-tori. For the latter solutions, the oscillations of the physical properties are smaller than in the 2-tori, and the primitive azimuthal symmetry is broken.

Aside from the first bifurcated quasiperiodic solutions, quasiperiodic and resonant windows of motions have also been found with increasing Ra. Contrarily to the solutions bifurcated from the travelling waves, they exhibit a stronger interaction between the modes as well as temporal scale oscillations of the kinetic energy with significantly lower amplitude. In the Ra intervals between the previous quasiperiodic regions, a complex time dependence, without breaking the equatorial symmetry, has been found. Despite the chaotic behaviour of the solutions, they retain certain regular patterns. Intermittent periods dominated by different wave numbers, giving rise to different physical properties, are observed. This behaviour has been related with the existence of a stable solution

which connect two unstable solutions, i.e, an heteroclinic chain. Intermittent convection was found in numerical simulations with stress free boundary conditions [51, 29]. However, when dissipation occurs in the boundary layers, as in the experiments [6, 104, 41], no evidences of intermittence has been previously found. Then, in [6] they wonder if intermittent flows are characteristic of low E or only occur when dissipation is mainly produced in the interior of the fluid. Our results show that at least the latter is not correct. The fact that in the experiments [6, 104, 41] they did not find intermittent motions is perhaps because they occur very near the onset, and their experimental settings are not suitable in this situation.

The existence of a prograde mean zonal flow close to the outer boundary at the equator, comparable to the retrograde mean zonal flow near the inner sphere, has been found by computing the azimuthal average of the azimuthal component of the velocity field at a suitable set of points inside the shell. Analogous results were found in numerical simulations on a rotating annulus in the small gap limit [89] for $\sigma = 7$ with non-slip boundary conditions, in the numerical simulations of a spherical fluid shell with stress-free boundary conditions [114], or in the gallium experiments [6] and [41] at $E \geq 2 \times 10^{-6}$. The modulus of the velocity field at the radial collocation points allows to recognise the geostrophic character of the solutions, with convection located inside a cylinder of critical radius r_c, and near the inner boundary. The already observed tendency of r_c to increase towards the outer boundary, and the increase of the convection in the polar regions with increasing Ra is in agreement with our results.

Asymptotic relations for the limit where viscosity plays a negligible role have been found. Our results computed with non-slip boundary conditions and $\sigma = 0.1$ agree qualitatively with those found in [29] with stress-free boundary conditions and $\sigma = 0.3$. However, the quantitative agreement is only observed for $\overline{Ro_p}$ and $\overline{Nu^*}$ suggesting that the type of boundary conditions for $\mathbf{v}$ does not affect the order of magnitude of the heat transfer or the convective part of the flow. We have obtained that with non-slip boundary conditions the convective flow is a bit stronger while the heat transfer is slightly less favoured than with stress-free boundary conditions. As expected, the results for the zonal flow are considerably different due to the difference in the boundary conditions.

The power laws obtained from the numerical results are compared with those derived in [6] in the framework of the quasi-geostrophic approximation, obtaining satisfactory concordance only for the convective flow ($\overline{Ro_p}$). Although our results for the mean zonal flow agree qualitatively with the results of the gallium experiment [6], our power relation agrees much better with the scaling found in the sodium experiment [104], although significant differences in the prefactors, due to the difference in the Prandtl numbers, are obtained. Like the results of the sodium experiment, our numerical results show that the mean zonal flow stagnates at the highest Ra for a fixed and positive E. This fact is consistent with the negative slope of the ratio $\overline{K/K_{nz}}$. We have observed that, in the range of Ra where the latter ratio decreases, the solutions lose their equatorial symmetry.

The power law for the convective part of the heat flux obtained in [104], by assuming

as characteristic cell size that of the onset of convection, only fits with our results up to relatively moderate Ra. However at the highest Ra, our increase is larger, favoured, perhaps, by the development of the convection in the polar regions. On the other hand, the abrupt change in the slope of the temperature frequency spectra found in [104] at high frequencies is also present in our results. We have roughly obtained the knee frequency f_c, at which the frequency spectra changes sharply its slope, and its dependence on Ra. According to [104, 41] (and references therein), this frequency is related with the inverse cascade of energy dissipation in the framework of two-dimensional turbulence. We have found that the existence of a knee frequency in the spectrum is associated with solutions without equatorial symmetry and fully developed polar convection.

The quadratic scaling for the dependence between the radial and zonal characteristic velocities derived in [41], corresponding to weak supercritical regimes, is well reproduced by our numerical results. At higher Ra the agreement is not so good. We have found an exponent 1 lower than the 4/3 obtained there. Moreover, neither in the quasi-geostrophic numerical nor in the experimental results [41] observed the tendency of the zonal flow to saturate at strongly supercritical conditions. The change of slope was explained in terms of loss of geostrophy in [29], but a new interpretation was proposed in [41] because in their scalings they obtain the change from 2 to 4/3 using a quasi-geostrophic theory. Our results confirm the break down from 2 to a lower exponent, and, at the range of Ra where it occurs, the flow is strongly geostrophic keeping the equatorial symmetry. At the highest Ra the solutions lose their equatorial symmetry and the zonal flow saturates at finite E. We have checked that the lowering of the power is not due to the $m_d = 2$ azimuthal symmetry. We have repeated some of the calculations without imposing it getting analogous results. The tendency towards saturation was also found in the sodium experiments [104].

Finally, the fittings obtained for the several physical properties are used to extrapolate Earth's outer core values following the approach of [6]. The values are obtained by first estimating Ra_q from the geophysically predicted total heat flux at the outer boundary. Using known values of the parameters E, ν, κ and d, reasonable results are obtained, which resemble very much those existing in the literature. For instance, we have predicted a value of the mean zonal flow at the core-mantle boundary nearly 5×10^{-4} m/s, estimated from the westward drift of the secular variation of the magnetic field.

5.9 Appendix A: Validation of the results and integration parameters

The new pseudo-spectral code used in this study has been written for this purpose and tested in Chapter 4 with the known benchmark [30] obtaining satisfactory results. All the integrations are performed using dealiased spectral transforms. As it is widely known,

(see for instance [114]) their use stabilise the numerical method at the most demanding computations corresponding to low E.

The solutions are computed using a high order time integration scheme described in Chapter 4, more precisely, the variable size and variable order (VSVO) semi-implicit backward differentiation-extrapolation (IMEX-BDF) formulae with the Coriolis term treated implicitly. By using Krylov techniques for the linear systems, this method has been found efficient for integrating solutions at least weakly supercritical. The maximum order k allowed to the integration has been set to $k = 5$, and the tolerances ε^a and ε^r, below which the absolute and relative values of the time discretization errors are required, are set to 10^{-3}. This allows to obtain the solutions with relative error less than 10^{-5} in comparison with solutions obtained with the very low tolerances $\varepsilon^a = \varepsilon^r = 10^{-13}$ (see Chapter 4). For several solutions it is checked that the decrease of the tolerances to $\varepsilon^a = \varepsilon^r = 10^{-6}$ does not change significantly the results.

E	Ra_c	ω_c	m_c
10^{-4}	1.856×10^5	5.063×10^2	6
3.162×10^{-5}	6.369×10^5	1.097×10^3	8
8.165×10^{-6}	2.883×10^6	2.721×10^3	12

Table 5.8: The critical parameters Ra_c, ω_c and m_c for three Ekman numbers E. The other parameters are $\eta = 0.35$, and $\sigma = 0.1$.

$E = 10^{-4}$

Ra^*/Ra_c^*	$\overline{Re}$	$\overline{Re_p}$	$\overline{Nu}$	$\overline{K/K_{nz}}$	σ_{K_p}	N_r	L	m_d
5.39	263.460	107.78	1.286	1.98	0.32	32	54	2
5.39	258.030	105.81	1.270	1.87	0.21	32	54	1
5.39	260.080	107.41	1.275	1.86	0.21	50	84	1

$E = 3.162 \times 10^{-5}$

Ra^*/Ra_c^*	$\overline{Re}$	$\overline{Re_p}$	$\overline{Nu}$	$\overline{K/K_{nz}}$	σ_{K_p}	N_r	L	m_d
15.7	1359.58	572.13	2.634	2.07	0.14	50	84	2
15.7	1359.10	571.04	2.623	2.09	0.11	50	84	1

Table 5.9: Time-averaged properties: Reynolds number, $\overline{Re}$, its poloidal contribution, $\overline{Re_p}$, the Nusselt number, $\overline{Nu}$, the ratio of the total to the non-zonal kinetic energy densities, $\overline{K/K_{nz}}$, and the relative variance of the poloidal kinetic energy density, σ_{K_p}, for two solutions at different E.

At $E = 10^{-4}$ and small Ra, the solutions are obtained without symmetry assumptions ($m_d = 1$), that is by using all the spherical harmonics in the expansions of the functions. At about Ra ten times supercritical or greater a two-fold longitudinal symmetry is assumed (only the even modes in the spherical expansions are retained) because we have

checked that this does not change significantly the mean values of the fields, and nearly halves the computational time. For obtaining the curves of Fig. 5.44 at $E = 3.162 \times 10^{-5}$ and $E = 8.165 \times 10^{-6}$, two-fold ($md = 2$) and four-fold ($m_d = 4$) azimuthal symmetry is imposed, respectively (see Table 5.3). As has been mentioned in [29] among others, this does not represent a serious problem because convection at low E is dominated by high wave numbers. See for instance Table 5.8 where the critical parameters, for the three Ekman numbers used in this study, are shown. In Table 5.9, several space and time-averaged physical properties, computed with $m_d = 2$ and $m_d = 1$, are listed for two solutions at different Ekman numbers, in order to show the small differences caused by the use of different symmetry assumptions. However, in the regime of periodic or

$[0, t_f]$	f_1	f_2	f_3
$[0, 0.5]$	64.4125	27.8997	2.06323
$[0, 1]$	64.2619	27.9203	1.87644
$[0, 2]$	64.2752	27.9231	1.82027
$[0, 3]$	64.2741	27.9234	1.81899
$[0, 4]$	64.2741	27.9233	1.81888
$[0, 5]$	64.2741	27.9233	1.81871

Table 5.10: The independent frequencies f_1, f_2 and f_3 for different time series lengths $[0, t_f]$, for a solution computed with $E = 10^{-4}$, $Ra = 2.875 \times 10^5$, $\eta = 0.35$, and $\sigma = 0.1$.

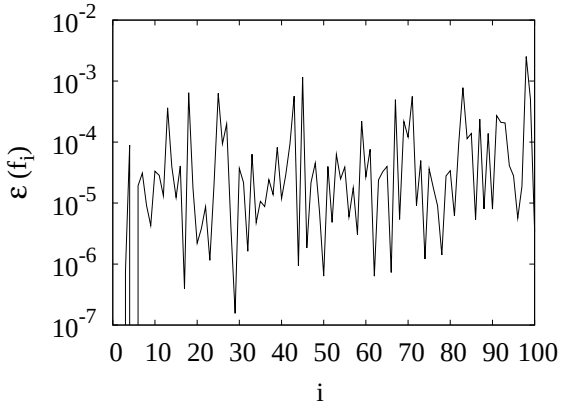

Figure 5.49: The relative error $\varepsilon(f_i^L)$ defined in Eq. (5.31), for the 100 first fundamental Laskar frequencies f_i^L, $i = 1, \ldots, 100$ of a solution computed with $E = 10^{-4}$, $Ra = 2.875 \times 10^5$, $\eta = 0.35$, and $\sigma = 0.1$.

quasiperiodic flows described in Sec. 5.3.1 and 5.3.3, the assumption of two-fold azimuthal symmetry leads to substantial differences, such as the impossibility of obtaining solutions governed by odd modes, as is the case of the $m = 5$ branch described at the beginning

of this chapter. Notice also the differences between the first frequency of the solutions in Figs. 5.1(a) 5.1(b).

At $E = 10^{-4}$, the first solution, corresponding to $Ra = 2\times10^5$, is computed by starting from an initial condition with velocity $\mathbf{v} = \mathbf{0}$, and temperature

$$T_B(r,\theta,\varphi) = \frac{r_i r_o}{r} - r_i + \frac{2A}{\sqrt{2\pi}}(1-x^2)^3 P_m^m(\theta)\cos m\varphi, \tag{5.30}$$

with $A = 0.1$, $x = 2r - r_i - r_o$, $m = 6$, and $P_m^m(\theta) = \sqrt{(2m+1)!!/2(2m)!!}\sin^m\theta$ the normalised associated Legendre function of order and degree m. The solution tends, after an abrupt transient, to an azimuthal travelling wave of wave number $m = 6$. At high Ra the calculations are started from a solution computed at previous lower Ra, perhaps changing its spatial resolution. It is worth noticing that the solutions obtained following this procedure may change depending on the Ra sequence, and also on the initial condition. For the lower E, the first solution is computed using again the initial condition given in Eq. (5.30), but with $m = 8$ at $E = 3.162\times10^{-5}$, and $m = 12$ at $E = 8.165\times10^{-6}$. As mentioned above, sometimes the given resolution is increased, and the results are compared in order to look for spatial discretization errors (see Table 5.9).

The initial transients are discarded until a stationary pattern is reached or until the time-averaged properties and the Laskar fundamental frequencies do not change substantially. In Table 5.10 the independent frequencies f_1, f_2 and f_3 of a solution computed at $E = 10^{-4}$ and $Ra = 2.875\times10^5$, are shown for several time series of increasing length. Notice in this table that for large E integrating two dimensionless time units is enough for obtaining frequencies with errors of the same order of magnitude than the requested time integration errors (10^{-3}).

In order to check the quasiperiodicity of the 2 and 3-tori, the relative errors

$$\varepsilon_i = \min_{-5\le k_1,k_2\le 5} |f_i^L - (k_1 f_1 + k_2 f_2)|/f_i^L$$

are computed for each frequency f_i^L given by the Laskar's algorithm. In Fig. 5.49 the relative errors

$$\varepsilon_i = \min_{-10\le k_1,k_2,k_3\le 10} |f_i^L - (k_1 f_1 + k_2 f_2 + k_3 f_3)|/f_i^L \tag{5.31}$$

are plotted for the 100 first fundamental Laskar frequencies f_i^L, corresponding to the quasiperiodic solution computed at $E = 10^{-4}$ and $Ra = 2.875\times10^5$. Notice that all of them have $\varepsilon_i \lesssim 10^{-3}$. The first twenty constants k of the linear combinations of the independent frequencies are shown in Table 5.11, which also includes the absolute errors $\epsilon_i = f_i^L\varepsilon_i$.

The computation of resonant orbits is performed by applying a secant method to find a zero of $R - p/q$ (within a discrepancy of 10^{-4}) as a function of Ra, where R represents the rotation number, i.e, the ratio of two frequencies, and p/q is a rational number. On

Laskar order i	k_1	k_2	k_3	f_i^L	ϵ_i
1	1	0	0	64.2741	0
2	1	-1	0	36.3509	2.5×10^{-3}
3	1	1	0	92.1975	2.4×10^{-3}
4	0	1	0	27.9257	0
5	1	0	-1	62.4566	1.2×10^{-3}
6	1	0	1	66.0930	9.7×10^{-5}
7	1	-1	1	38.1697	2.5×10^{-3}
8	1	-2	0	8.42758	4.9×10^{-3}
9	0	2	0	55.8467	4.8×10^{-3}
10	1	-1	-1	34.5322	2.5×10^{-3}
11	1	2	0	120.117	8.4×10^{-3}
12	1	1	1	94.0162	2.4×10^{-3}
13	1	-2	1	10.2490	7.6×10^{-3}
14	1	0	-2	60.6366	4.4×10^{-5}
15	1	1	-1	90.3787	2.4×10^{-3}
16	0	1	-1	26.1046	2.4×10^{-3}
17	2	-1	0	100.625	2.5×10^{-3}
18	0	0	1	1.81875	0
19	0	2	-1	54.0279	4.8×10^{-3}
20	2	-2	0	72.7016	4.8×10^{-3}

Table 5.11: Fundamental Laskar frequencies f_i of the time series of the temperature perturbation Θ at $(r, \varphi, \theta) = (r_i + (r_o - r_i)/7, 0, 3\pi/8)$. The errors ϵ_i are defined as $\epsilon_i = |f_i^L - (k_1 f_1 + k_2 f_2 + k_3 f_3)|$, being $f_1 = f_1^L$, $f_2 = f_4^L$, and $f_3 = f_{18}^L$. The parameters are $\eta = 0.35$, $\sigma = 0.1$, $E = 10^{-4}$, and $Ra = 2.875 \times 10^5$.

the other hand, the Poincaré sections are obtained by linear interpolation from the time series of the solutions. The distance between samples ($\Delta t = 10^{-4}$) is sufficiently small to provide enough accuracy for the plots.

Finally, in Table 5.12, the same volume and time-averaged physical properties as in Table 2 of [29] are shown in order to check the computation of the physical properties. They are computed by using the same parameters and boundary conditions as in [29]. We also show the mean ratio of the total to the non-zonal kinetic energy densities (shown in Fig. 6(c) of [29]). Both solutions are obtained without symmetry assumptions in longitude $m_d = 1$, although in [29] a two-fold symmetry is imposed for the solutions corresponding to $E = 10^{-4}$. The numerical resolution is also indicated in the table.

$E = 3 \times 10^{-4}$

Ra^*/Ra_c^*	$\overline{Re}$	$\overline{Re_p}$	$\overline{Nu}$	$\overline{K/K_{nz}}$	σ_{K_p}	N_r	L	m_d
5.36	40.6	12.6	1.338	2.90	0.17	32	53	1
6.7	59.9	17.0	1.470	3.80	0.33	32	53	1

$E = 10^{-4}$

Ra^*/Ra_c^*	$\overline{Re}$	$\overline{Re_p}$	$\overline{Nu}$	$\overline{K/K_{nz}}$	σ_{K_p}	N_r	L	m_d
4.3	39.7	8.43	1.134	4.84	0.28	32	53	1

Table 5.12: Results for $\sigma = 1$ and stress-free boundary conditions, corresponding to Table 2 of [29]. Time-averaged properties: Reynolds number, $\overline{Re}$, its poloidal contribution, $\overline{Re_p}$, the Nusselt number, $\overline{Nu}$, the ratio of the total to the non-zonal kinetic energy densities, $\overline{K/K_{nz}}$ (shown in Fig. 6(c) of [29]), and the relative variance of the poloidal kinetic energy density, σ_{K_p}.

Chapter 6

Conclusions and further work

6.1 Conclusions

A numerical approach for the study of the thermal convection in rapidly rotating spherical shells is performed in this dissertation. The improvement of the numerical techniques has allowed a detailed study that clarify previous results and show some unexpected aspects in the subject.

The first part of the study deals with the linear stability problem to analyse the onset of convection. Specifically, the dependence of the critical Rayleigh number Ra_c, the critical precession frequency ω_c, and the critical azimuthal wave number m_c on the Ekman and Prandtl numbers (with $\sigma \leq 0.1$), and the features of the preferred modes of convection in the parameter space, were studied.

The onset of convection has been studied in a thick shell of $\eta = 0.2$, for low σ fluids with non-slip boundary conditions, internal heating ($Ra = Ra_i$) and low E. The computations in this range of parameters are very expensive because of the Ekman layers, which appear due to the non-slip boundary conditions. For this reason this is the first exhaustive numerical study that allows to check the theoretical asymptotic laws carefully. The results of the linear stability study (Chapter 2) have been published in [79]. One of the goals of [79] is the location of the transition between the outer equatorially attached (OEA) and the spiralling columnar (SC) modes in the (σ, E) parameter space. It is also found that for very low σ, the equatorially trapped mono-cellular modes are soon superseded by multicellular modes when E decreases, in agreement with the work of [89] in a rotating annuli. The numerical potential laws obtained for the critical parameters agree well on average with the leading order of the theoretical asymptotic expansions of [94, 14, 32].

In [40] (Chapter 3), preferred polar antisymmetric modes of convection at low E have been found and described for the first time, with either non-slip or stress-free boundary conditions and internal heating. For this antisymmetric convection, the power law dependence of Ra_c and ω_c with the Taylor number Ta is numerically determined. For Ra_c

the power is 0.57 clearly lower than 2/3, the leading order of the asymptotic expansions given theoretically in [32, 14, 94]. However the same power rules are obtained for the symmetric inner modes attached to the external part of the tangent cylinder, computed with $\eta = 0.35$, $\sigma = 0.1$, differential heating ($Ra = Ra_e$) and non-slip boundary conditions.

The optimisation of the time integration method for the nonlinear problem has been undertaken in Chapter 4 and published in [39]. Semi-implicit backward differentiation-extrapolation (IMEX-BDF) or (BDF) formulae, with the non-linear terms of the equations treated explicitly or implicitly, respectively, have been implemented. The study of the efficiency of the time integration methods, with the Coriolis term treated either as semi-implicit or as fully implicit, is presented. It is shown that (preconditioned) Krylov or Arnoldi iterative methods can be used to solve the Coriolis-implicit linear system, reducing considerably the amount of memory required. Taking the Coriolis term implicitly results in a more efficient time integration for low values of the Ekman number. The results show that high order methods can be used not only to compute high-accurate solutions, but also to obtain the same accuracy as with lower order, but more efficiently. In practice, the most efficient method depends on the value of the Ekman number, on the precision wanted, and even on the type of solution.

In the second part of the dissertation the finite-amplitude convection was studied. With the parameters of the Earth's outer liquid core, two different regimes were found for $E \lesssim 10^{-4}$. By increasing the Rayleigh number, a first regime of coherent oscillatory flows is superseded by another of chaotic temporal and spatial flows. In this latter the equatorial symmetry of the former flows is broken.

The oscillatory flows are characterised by low heat transfer and they are strongly geostrophic. Quasiperiodic 2-tori and 3-tori are obtained bifurcated from travelling waves. Quasiperiodic windows of motions have also been found at high Ra. Contrarily to the solutions bifurcated from the travelling waves, they exhibit stronger interaction between modes as well as small temporal scale oscillations of the physical properties.

Complex time dependencies between the quasiperiodic regimes have been found. An intermittence of periods dominated by patterns with different wave numbers giving rise to different physical properties, is observed. This behaviour has been related with the existence of a stable solution which nearly connects two unstable solutions., i.e., it is an almost heteroclinic chain. In [28, 27], intermittent motions in a slow rotating spherical shell were associated with the existence of a heteroclinic cycle near the onset. Intermittent motions have also been found with stress-free boundary conditions in [51, 50, 29, 106]. However no evidence of this phenomenon has been found in experiments [6, 104]. Our results suggest that intermittent convection is also characteristic of low E, and it is not only limited to the stress-free case.

At the highest Ra the solutions are strongly chaotic in space and time breaking the equatorial symmetry. The existence of prograde mean zonal flows close to the outer boundary at the equator and comparable to the retrograde mean zonal flows near the inner cylinder, found in [89] for a rotating annulus, and in the experiments of liquid

gallium in [41], was confirmed.

Following the guidelines of [29] asymptotic relations for the limit where viscosity plays a negligible role, have been found. Comparable results for the convective flow and the heat transfer are obtained in both studies. However the results for the zonal flow are considerably different due to the difference between the boundary conditions. Our scaling laws are also compared with the quasi-geostrophic scaling of [6]. Although our results for the mean zonal flow agree qualitatively with the experimental results obtained using gallium [6], our scaling relation agree much better with that of [104] obtained by balancing the Coriolis and the buoyancy forces. As in the experimental study [104], employing sodium, the zonal flow stagnates at the highest Ra values for fixed E. This is consistent with the negative slope of the ratio $\overline{K/K^{nz}}$ obtained at those Ra values.

The abrupt change in the slope of the temperature frequency spectra found in [104] at high frequencies is also present in our results. The quadratic dependence between the radial and zonal characteristic velocities derived in [41], corresponding to weak supercritical situations is also well reproduced, but we have found, like in [29], a smaller increase of the zonal contribution at moderate regimes than in [41]. In addition, we have found the saturation tendency of the zonal flow at strongly supercritical conditions like in [104].

Finally, the power laws obtained for the physical properties are used to extrapolate Earth's outer core values, following the approach of [6]. In the later study the geophysical values are obtained by first estimating the value of the Rayleigh number Ra_q based on the knowledge of the total heat flux at the outer boundary. From the usual estimated parameters E, σ, ν, κ and d of the Earth's outer core, results are obtained which agree quite well with those existing in the literature.

6.2 Further work

The final objective is a better and deeper understanding of the nonlinear dynamics studied along this dissertation. For this purpose tools of Dynamical Systems theory, largely and successfully applied to systems with few degrees of freedom, will be used. Specifically the objectives, which will be undertaken are:

1. Continuation of thermal Rossby waves and study of its stability following for instance the methodology of [98]. With the help of the numerical trajectories on the unstable manifolds, we will try to find orbits nearly connecting unstable waves and other stable solutions.

2. Using nonlinear time series analysis we hope to gain some knowledge about the unstable and stable attractors described along this dissertation. Lyapunov exponents are usually used to quantify chaos in nonlinear dynamical systems. The Kaplan-Yorke dimension can also be obtained providing information about the complexity of the system and the fractal dimension of the attractors.

In order to achieve these aims, the package of numerical codes will be improved and extended. The parallel implementation of the three dimensional time integration code will allow to integrate the equations more efficiently. For this purpose the tasks will be:

- Parallel implementation of the linear solvers and of the evaluation of the nonlinear terms in the equations. The latter is the most expensive in terms of computational time.
- Study of the benefit of the use of shared, versus distributed memory using OpenMp [25] or MPI [35], for performing the previous calculations.

For the study of the stability of the thermal Rossby waves, the following tasks are suggested:

- The low-dimensional unstable manifolds of the waves can be approximated by means of temporal integration with initial conditions lying on the unstable directions. The initial conditions can be obtained through stability analysis of the waves.
- In order to deepen in complicated regimes, such as the intermittence, recent advances on proper orthogonal decomposition techniques (POD) and spectral analysis of operators [43, 93, 107, 2] can be used to find reduced dimension and normal form models.
- Recently, it has been shown that POD techniques allow to accelerate the temporal integration of two-dimensional computational fluid dynamics (CFD) problems. If it was necessary we could try to apply the method described in [2] to our three dimensional model and study its efficiency.

The procedures that will be employed for the nonlinear time series analysis are:

- State space reconstruction techniques, such as the method of delays, are used to estimate the maximal Lyapunov exponent from a time series using the TISEAN package [57]. The subroutine `lyap_k` can be used to obtain results.
- The estimation of the fully Lyapunov spectrum requires a huge numerical effort, but can be used to predict the Kaplan-Yorke dimension D_{KY} of the attractor. We will try to obtain results using the `lyap_spec` subroutine of [57].
- Study of the dependence of the Lyapunov spectrum, as well as D_{KY} with the Rayleigh number, as it was done for the physical properties in the last chapter of the dissertation.
- Another procedure, based on frequency analysis will be used to detect chaotic motions [47]. The results obtained could be compared with those using the Lyapunov spectrum.

Bibliography

[1] F.M. Al-Shamali, M.H. Heimpel, and J.M. Aurnou. Varying the spherical shell geometry in rotating thermal convection. *Geophys. Astrophys. Fluid Dynamics*, 98(2):153–169, 2004.

[2] D. Alonso, A. Velázquez, and J. M. Vega. Robust reduced order modeling of heat transfer in a back step flow. *Intnl J. Heat Mass Transfer*, 42:1147–1152, 2009.

[3] M. Ardes, F. H. Busse, and J. Wicht. Thermal convection in rotating spherical shells. *Phys. Earth Planet. Inter.*, 99:55–67, 1997.

[4] U. M. Ascher and L. Petzold. Computer Methods for Ordinary Differential Equations and Differential-Algebraic Equations. *SIAM*, 1998.

[5] D.H. Atkinson, J.B. Pollack, and A. Seiff. The galileo probe doppler wind experiment, measurement of the deep zonal winds on jupiter. *J. Geophys. Res. Planets*, 103(E10):22911–22928, 1998.

[6] J. Aubert, D. Brito, H.-C. Nataf, P. Cardin, and J.-P. Masson. A systematic experimental study of rapidly rotating spherical convection in water and liquid gallium. *Phys. Earth Planet. Inter.*, 128:51–74, 2001.

[7] J. Aubert, N. Gillet, and P. Cardin. Quasigeostrophic models of convection in rotating spherical shells. *Geochem. Geophys. Geosyst.*, 4(7):1052–1071, 2003.

[8] J.M. Aurnou, S. Andreadis, L. Zhu, and Olson P. Experiments on convection in Earth's core tangent cylinder. *EPSL*, 212:119–134, 2003.

[9] J.M. Aurnou and M.H. Heimpel. Zonal jets in rotating convection with mixed mechanical boundary conditions. *ICARUS*, pages 1–7, 2004.

[10] J.M. Aurnou and P.L. Olson. Strong zonal winds from thermal convection in a rotating spherical shell. *Geophys. Res. Lett.*, 28(13):2557–2559, 2001.

[11] O. Batiste, I. Mercader, M. Net, and E. Knobloch. Onset of oscillatory binary fluid convection in finite containers. *Phys. Rev. E*, 59(6):6730–6741, 1999.

[12] M. Borland, L. Emery, H. Shang, and R. Soliday, 2005. User's Guide for SDDS Toolkit Version 1.30, It is available on the web at `http://www.aps.anl.gov/asd/oag/software.shtml`.

[13] J. P. Boyd. *Chebyshev and Fourier Spectral Methods*. Dover, New York, 1999.

[14] F. H. Busse. Thermal instabilities in rapidly rotating systems. *J. Fluid Mech.*, 44:441–460, 1970.

[15] F. H. Busse. Convective flows in rapidly rotating spheres and their dynamo action. *Phys. Fluids*, 14(4):1301–1313, 2002.

[16] F. H. Busse and C. R. Carrigan. Convection induced by centrifugal buoyancy. *J. Fluid Mech.*, 62:579, 1974.

[17] F. H. Busse and C. R. Carrigan. Laboratory simulation of thermal convection in rotating planets and stars. *Science*, 191:81–83, 1976.

[18] F. H. Busse and A. C. Or. Convection in a rotating cylindrical annulus: thermal Rossby waves. *J. Fluid Mech.*, 166:173–187, 1986.

[19] F. H. Busse and R. Simitev. Inertial convection in rotating fluid spheres. *J. Fluid Mech.*, 498:23–30, 2004.

[20] C. Canuto, M. Y. Hussaini, A. Quarteroni, and T. A. Zang. *Spectral Methods in Fluid Dynamics*. Springer, 1988.

[21] P. Cardin, D. Brito, D. Jault, H.-C. Nataf, and J.-P. Masson. Towards a rapidly rotating liquid sodium dynamo experiment. *Magnetohydrodynamics*, 38(1–2):177–189, 2002.

[22] P. Cardin and P. Olson. Chaotic thermal convection in a rapidly rotating spherical shell: consequences for flow in the outer core. *Phys. Earth Planet. Inter.*, 82:235–259, 1994.

[23] C. R. Carrigan and F. H. Busse. An experimental and theoretical investigation of the onset of convection in rotating spherical shells. *J. Fluid Mech.*, 126:287–305, 1983.

[24] S. Chandrasekhar. *Hydrodynamic And Hydromagnetic Stability*. Dover, New York, 1981.

[25] B. Chapman, G. Jost, and R. van der Pas. *Using OpenMP. Portable Shared Memory Parallel Programming*. Scientific and Engineering Computation. MIT Press, 2007.

[26] C. X. Chen and K. Zhang. Nonlinear convection in a rotating annulus with a finite gap. *Geophys. Astrophys. Fluid Dynamics*, 96:499–518, 2002.

[27] P. Chossat. *Intermittency at onset of convection in a slowly rotating, self-gravitating spherical shell*, volume 549 of *Lecture Notes in Physics*. Springer, 2000.

[28] P. Chossat, F. Guyard, and R. Lauterbach. Generalized heteroclinic cycles in spherically invariant systems and their perturbations. *J. Nonlinear Sci.*, 9:479–524, 1999.

[29] U.R. Christensen. Zonal flow driven by strongly supercritical convection in rotating spherical shells. *J. Fluid Mech.*, 470:115–133, 2002.

[30] U.R. Christensen, J. Aubert, P. Cardin, E. Dormy, S. Gibbons, G.A. Glatzmaier, E. Grote, Y. Honkura, C. Jones, M. Kono, M. Matsushima, A. Sakuraba, F. Takahashi, A. Tilgner, J. Wicht, and K. Zhang. A numerical dynamo benchmark. *Phys. Earth Planet. Inter.*, 128:25–34, 2001.

[31] C. F. Curtiss and J. O. Hirschfelder. Integration of stiff equations. *PNASUSA*, 38:235–243, 1952.

[32] E. Dormy, A. M. Soward, C. A. Jones, D. Jault, and P. Cardin. The onset of thermal convection in rotating spherical shells. *J. Fluid Mech.*, 501:43–70, 2004.

[33] R. E. Ecke, F. Zhong, and E. Knobloch. Hopf bifurcation with broken reflection symmetry in rotating Rayleigh-Bénard convection. *Europhys. Lett.*, 19:177–182, 1992.

[34] C. C. Finlay and A. Jackson. Equatorially dominated magnetic field change at the surface of the Earth's core. *Science*, 300(5628):2084–2086, 2003.

[35] Message Passing Forum. Mpi: A message-passing interface standard. Technical report, University of Tennessee, 1994.

[36] Matteo Frigo and Steven G. Johnson. The design and implementation of FFTW3. *Proceedings of the IEEE*, 93(2):216–231, 2005. special issue on "Program Generation, Optimization, and Platform Adaptation".

[37] A. Gailitis, O. Lielausis, S. Dement'ev, E. Platacis, A. Cifersons, G. Gerbeth, T. Gundrum, F. Stefani, M. Christen, H. Hänel, and G. Will. Detection of flow induced magnetic field eigenmode in the Riga dynamo facility. *Phys. Rev. Lett.*, 84(19):4365–4368, 2000.

[38] A. Gailitis, O. Lielausis, E. Platacis, A. Dement'ev, S. Cifersons, G. Gerbeth, T. Gundrum, F. Stefani, M. Christen, and G. Will. Magnetic field saturation in the Riga dynamo experiment. *Phys. Rev. Lett.*, 86(14):3024–3027, 2001.

[39] F. Garcia, M. Net, B. García-Archilla, and J. Sánchez. A comparison of high-order time integrators for thermal convection in rotating spherical shells. *J. Comput. Phys.*, 229:7997–8010, 2010.

[40] F. Garcia, J. Sánchez, and M. Net. Antisymmetric polar modes of thermal convection in rotating spherical fluid shells at high Taylor numbers. *Phys. Rev. Lett.*, 101:194501–(1–4), 2008.

[41] N. Gillet, D. Brito, D. Jault, and H.-C. Nataf. Experimental and numerical studies of convection in a rapidly rotating spherical shell. *J. Fluid Mech.*, 580:83–121, 2007.

[42] N. Gillet and C. A. Jones. The quasi-geostrophic model for rapidly rotating spherical convection outside the tangent cylinder. *J. Fluid Mech.*, 554:343–369, 2006.

[43] D. Givon, R. Kupferman, and A. Stuart. Extracting macroscopic dynamics: model problems and algorithms. *Nonlinearity*, 17:55–127, 2004.

[44] G.A. Glatzmaier. Numerical simulations of stellar convective dynamos. I. The model and method. *J. Comput. Phys.*, 55:461–484, 1984.

[45] G.A. Glatzmaier and P.H. Roberts. A three-dimensional convective dynamo solution with rotating and finitely conducting inner core and mantle. *Phys. Earth Planet. Inter.*, 91:63–75, 1995.

[46] G.A. Glatzmaier and P.H. Roberts. A three-dimensional self-consistent computer simulation of a geomagnetic field reversal. *Nature*, 377:203–209, 1995.

[47] G. Gómez, J. M. Mondelo, and C. Simó. A collocation method for the numerical fourier analysis of quasi-periodic functions. I: Numerical tests and examples. *Discrete and Continuous Dynamical Systems-Series B*, 14(1):41–74, 2010.

[48] Kazushige Goto and Robert A. van de Geijn. Anatomy of high-performance matrix multiplication. *ACM Trans. Math. Softw.*, 34(3):1–25, 2008.

[49] S. Grossmann and D. Lohse. Scaling in thermal convection: a unifying theory. *J. Fluid Mech.*, 407:27–56, 2000.

[50] E. Grote and F.H. Busse. Dynamics of convection and dynamos in rotating spherical fluid shells. *Fluid Dyn. Res.*, 28:349–356, 2001.

[51] E. Grote, F.H. Busse, and Tilgner. Regular and chaotic spherical dynamos. *Phys. Earth Planet. Inter.*, 117:259–272, 2000.

[52] D. Gubbins. The Rayleigh number for convection in the Earth's core. *Phys. Earth Planet. Inter.*, 128:3–12, 2001.

[53] D. Gubbins and P. H. Roberts. Magnetohydrodynamics of the Earth's core. *Geomagnetism*, 2:1–183, 1987.

[54] E. Hairer, H. P. Norsett, and G. Wanner. *Solving Ordinary Differential Equations. I Nonstiff Problems (2nd. Revised Edition).* Springer-Verlag, 1993.

[55] E. Hairer and G. Wanner. *Solving Ordinary Differential Equations. II. Stiff and Differential-Algebraic Problems.* Springer, 1991.

[56] J. E. Hart, G. A. Glatzmaier, and J. Toomre. Space-laboratory and numerical simulations of thermal convection in a rotating hemispherical shell with radial gravity. *J. Fluid Mech.*, 173:519–, 1986.

[57] R. Hegger, H. Kantz, and T. Schreiber. Practical implementation of nonlinear time series methods: The tisean package. *CHAOS*, 413, 1999.

[58] P. Henrici. *Discrete Variable Methods in Ordinary Differential Equations.* John Willey and Sons, 1962.

[59] J. Herrmann and F. H. Busse. Convection in a rotating cylindrical annulus. Part 4. Modulations and transitions to chaos at low Prandtl numbers. *J. Fluid Mech.*, 350:209–229, 1997.

[60] R. Hide. Motions of the Earth's core and mantle, and variations of the main geomagnetic field. *Science*, 157:55–56, 1967.

[61] A. C. Hindmarsh. ODEPACK, a systematized collection of ODE solvers. In R. S. Stepleman et al., editor, *Scientific Computing*, pages 55–364. North-Holland, Amsterdam, 1983.

[62] R. Hollerbach. A spectral solution of the magneto-convection equations in spherical geometry. *Int. J. Num. Meth. Fluids*, 32:773–797, 2000.

[63] M. Jaletzky. *Experimental study of rotating cylindrical annulus convection.* PhD thesis, University of Bayreuth, 1999.

[64] D. Jault, G. Gire, and J. L. Le Mouël. Westward drift, core motions and exchanges of angular momentum between core and mantle. *Nature*, 333:353–356, 1998.

[65] C. A. Jones, A. W. Longbottom, and R. Hollerbach. A self-consistent convection driven geodynamo model, using a mean field approximation. *Phys. Earth Planet. Inter.*, 92:119–141, 1995.

[66] C. A. Jones, A. M. Soward, and A. I. Mussa. The onset of thermal convection in a rapidly rotating sphere. *J. Fluid Mech.*, 405:157–179, 2000.

[67] G.E. Karniadakis, M. Israeli, and S. A. Orszag. High-order splitting methods for the incompressible Navier-Stokes equations. *J. Comput. Phys.*, 97:414–443, 1991.

[68] H. B. Keller. Numerical solution of bifurcation and nonlinear eigenvalue problems. In P. H. Rabinowitz, editor, *Applications of Bifurcation Theory*, pages 359–384. Academic Press, 1977.

[69] H. Kitauchi, K. Araki, and S. Kida. Flow structure of thermal convection in a rotating spherical shell. *Nonlinearity*, 10:885–904, 1997.

[70] P. Kolodner. Repeated transients of weakly nonlinear traveling-wave convection. *Phys. Rev. E*, 47(2):1038–1048, 1993.

[71] J. Laskar. Frequency analysis of a dynamical system. *Celestial Mechanics and Dynamical Astronomy*, 56:191–196, 1993.

[72] R. B. Lehoucq, D. C. Sorensen, and C. Yang. *ARPACK User's Guide: Solution of Large-Scale Eigenvalue Problems with Implicitly Restarted Arnoldi Methods*. SIAM, 1998.

[73] L. Li, P. Zhang, X. Liao, and K. Zhang. Multiplicity of nonlinear thermal convection in a spherical shell. *Phys. Rev. E*, 71(016301):1–9, 2005.

[74] J.R. Lister and B.A. Buffet. The strength and efficiency of thermal and compositional convection in the Earth's core. *Phys. Earth Planet. Inter.*, 91:17–30, 1995.

[75] J.B Manneville and P.L. Olson. Banded convection in rotating fluid spheres and the circulation of the Jovian atmosphere. *ICARUS*, 112(2):242–250, 1996.

[76] M. S. Miesch, J. R. Elliot, J. Toomre, T. L. Clune, G. A. Glatzmaier, and P. A. Gilman. Three-dimensional spherical simulation of solar convection. I. Diferential rotation and pattern evolution achieved with laminar and turbulent states. *The Astrophysical Journal*, 532:593–615, 2000.

[77] V. Morin and E. Dormy. Dissipation mechanisms for convection in rapidly rotating spheres and the formation of banded structures. *Phys. Fluids*, 18:068104–1–068104–4, 2006.

[78] U. Müller and R. Stieglitz. The karlsruhe dynamo experiment. *Nonlinear Processes in Geophysics*, 9:165–170, 2002.

[79] M. Net, F. Garcia, and J. Sánchez. On the onset of low-prandtl-number convection in rotating spherical shells: non-slip boundary conditions. *J. Fluid Mech.*, 601:317–337, 2008.

[80] P. Olson. Laboratory experiments on the dynamics of the core. *Phys. Earth Planet. Inter.*, 187:1–18, 2011.

[81] P. Olson and J. Aurnou. A polar vortex in the Earth's core. *Nature*, 402:170–173, 1999.

[82] A.C. Or and J. Herrmann. Anomalous sideband instabilities of thermal Rossby waves at low Prandtl numbers. *Phys. Fluids*, 7(2):315–323, 1995.

[83] S. A. Orszag. Transform method for calculation of vector-coupled sums: Application to the spectral form of the vorticity equation. *J. Atmos. Sci.*, 27:890–895, 1970.

[84] D. Pazó, E. Sánchez, and M. A. Matías. Transition to high-dimensional chaos through quasiperiodic motion. *Int. J. Bifurcation and Chaos*, 11(10):2683–2688, 2001.

[85] A. S. Pikovsky. A new type of intermittent transition to chaos. *J. Phys. A: Math. Gen.*, 16:109–112, 1983.

[86] D. Pino, I. Mercader, and M. Net. Thermal and inertial modes of convection in a rapidly rotating annulus. *Phys. Rev. E*, 61(2):1507–1517, 2000.

[87] D. Pino, M. Net, J. Sánchez, and I. Mercader. Thermal Rossby waves in a rotating annulus: Their stability. *Phys. Rev. E*, 63:056312–1, pp 14, 2001.

[88] E. Plaut and F. H. Busse. Low-Prandtl-number convection in a rotating annulus. *J. Fluid Mech.*, 464:345–363, 2002.

[89] E. Plaut and F. H. Busse. Multicellular convection in rotating annuli. *J. Fluid Mech.*, 528:119–133, 2005.

[90] E. Plaut, Y. Lebranchu, R. Simitev, and F. H. Busse. Reynolds stresses and mean fields generated by pure waves: applications to shear flows and convection in a rotating shell. *J. Fluid Mech.*, 602:303–326, 2008.

[91] J. P. Poirier. *Introduction to the physics of the Earth's interior*. Cambridge University press, Manchester, 2000.

[92] Y. Pomeau and P. Manneville. Intermittent transition to turbulence in dissipative dynamical systems. *Commun. Math. Phys.*, 74:189–197, 1980.

[93] G. Rega and H. Troger. Dimension Reduction of Dynamical Systems: Methods Models, Applications. *Nonlinearity*, 41:1–15, 2005.

[94] P. H. Roberts. On the thermal instability of a rotating fluid sphere containing heat sources. *Phil. Trans. R. Soc. Lond. A*, 263:93–117, 1968.

[95] R. E. Rosensweig, J. Browaeys, J.-C. Bacri, A. Zebib, and R. Perzynski. Laboratory study of spherical convection in simulated central gravity. *Phys. Rev. Lett.*, 83(23):4904–4907, 1999.

[96] Y. Saad. *Iterative methods for sparse linear systems*. PWS pub. company, New York, 1996.

[97] Y. Saad and M. H. Schultz. GMRES: a generalized minimal residual algorithm for solving nonsymmetric linear systems. *SIAM J. Sci. Stat. Comput.*, 7:865–869, 1986.

[98] J. Sánchez, M. Net, B. García-Archilla, and C. Simó. Newton-Krylov continuation of periodic orbits for Navier-Stokes flows. *J. Comput. Phys.*, 201(1):13–33, 2004.

[99] J. Sánchez, M. Net, and C. Simó. Computation of invariant tori by Newton-Krylov methods in large-scale dissipative systems. *Physica D*, 239:123–133, 2010.

[100] J. Sánchez, M. Net, and J.M. Vega. Amplitude equations close to a triple-(+1) bifurcation point of D_4-symmetric periodic orbits in $O(2)$-equivariant systems. *Discrete and Continuous Dynamical Systems-Series B*, 6(6):1357–1380, 2006.

[101] M. Schnaubelt and F. H. Busse. Convection in a rotating cylindrical annulus. Part 3. Vacillating and spatially modulated flow. *J. Fluid Mech.*, 245:155–173, 1992.

[102] G. Schubert and K. Zhang. Dynamics of giant planet interiors. *From Giant Planets to Cool Stars, ASP Conference Series*, 212:210–222, 2000.

[103] R. A. Secco and H. H. Schloessin. The electrical resistivity of solid and liquid Fe at pressures up to 7 GPa. *J. Geophy. Res. B*, 94(5):5887–5894, 1989.

[104] W. L. Shew and D. P. Lathrop. Liquid sodium model of geophysical core convection. *Phys. Earth Planet. Inter.*, 153:136–149, 2005.

[105] B. I. Shraiman and E. D. Siggia. Heat transport in high-Rayleigh-number convection. *Phys. Rev. A*, 42(6):3650–3653, 1990.

[106] R. Simitev and F. H. Busse. Patterns of convection in rotating spherical shells. *New Journal of Physics*, 5:97.1–97.20, 2003.

[107] T. R. Simth, J. Moehlis, and P. J. Holmes. Low-dimensional modelling of turbulence using the proper orthogonal decomposition: A tutorial. *Nonlinear Dynamics*, 41:275–307, 2005.

[108] A. M. Soward. On the finite amplitude thermal instability in a rapidly rotating fluid sphere. *Geophys. Astrophys. Fluid Dynamics*, 9:19–74, 1977.

[109] J. C. Sprott, J. C. Wildenberg, and Y. Azizi. A simple spatiotemporal chaotic Lotka-Volterra model. *Chaos, Solitons and Fractals*, 26:1035–1043, 2005.

[110] G. Sullivan, T. S. Ahlers. Nonperiodic time dependence at the onset of convection in a binary liquid mixture. *Phys. Rev. A*, 38(6):3143–3146, 1988.

[111] J. Tao and F.H. Busse. Thermal convection in a rotating cylindrical annulus and its mean zonal flows. *J. Fluid Mech.*, 552:73–82, 2006.

[112] A. Tilgner. Spectral methods for the simulation of incompressible flow in spherical shells. *Int. J. Num. Meth. Fluids*, 30:713–724, 1999.

[113] A. Tilgner and F. H. Busse. Fluid flows in precessing spherical shells. *J. Fluid Mech.*, 426:387–396, 2001.

[114] A. Tilgner and F.H. Busse. Finite amplitude convection in rotating spherical fluid shells. *J. Fluid Mech.*, 332:359–376, 1997.

[115] A. M. Tilgner, M. Ardes, and F. H. Busse. Convection in rotating spherical fluid shells. *Acta Astron. et Geophys. Univ. Comenianae XIX*, pages 337–358, 1997.

[116] G. A. de Wijs, G. Kresse, L. Vočadlo, D. Dobson, D. Alfè, M. J. Gillan, and G. D. Price. The viscosity of liquid iron at the physical conditions of the Earth's core. *Nature*, 392:805–807, 1998.

[117] J. I. Yano. Asymptotic theory of thermal convection in a rapidly rotating system. *J. Fluid Mech.*, 243:103–131, 1992.

[118] K. Zhang. Spiralling columnar convection in rapidly rotating spherical fluid shells. *J. Fluid Mech.*, 236:535–556, 1992.

[119] K. Zhang. On equatorially trapped boundary inertial waves. *J. Fluid Mech.*, 248:203–217, 1993.

[120] K. Zhang. On coupling between the Poincaré equation and the heat equation. *J. Fluid Mech.*, 268:211–229, 1994.

[121] K. Zhang. On coupling between the Poincaré equation and the heat equation: non-slip boundary condition. *J. Fluid Mech.*, 284:239–256, 1995.

[122] K. Zhang and C. A. Jones. The influence of Ekman boundary layers on rotating convection. *Geophys. Astrophys. Fluid Dynamics*, 71:145–162, 1993.

[123] K. Zhang, C. A. Jones, and Sarson G. R. The dynamical effects of hyperviscosity on numerical geodynamo models. *Stud. Geophys. Geod.*, 42:247–253, 1998.

[124] K. Zhang and X. Liao. A new asymptotic method for the analysis of convection in a rapidly rotating sphere. *J. Fluid Mech.*, 518:319–346, 2004.

[125] K. Zhang, X. Liao, and F.H. Busse. Asymptotic solutions of convection in rapidly rotating non-slip spheres. *J. Fluid Mech.*, 578:371–380, 2007.

[126] K. Zhang, X. Liao, and F.H. Busse. Asymptotic theory of inertial convection in a rotating cylinder. *J. Fluid Mech.*, 575:449–471, 2007.

[127] K. Zhang and G. Schubert. Spatial symmetry breaking in rapidly rotating convective spherical shells. *Geophys. Res. Lett.*, 22(10):1265–1268, 1995.

[128] K. Zhang and G. Schubert. Magnetohydrodynamics in rapidly rotating spherical systems. *Ann. Rev. Fluid Mech.*, 32:409–443, 2000.

[129] K. K. Zhang. Convection in a rapidly rotating spherical shell at infinite Prandtl number: transition to vacillating flows. *Phys. Earth Planet. Inter.*, 72:236–248, 1992.

[130] K. K. Zhang and F. H. Busse. On the onset of convection in rotating spherical shells. *Geophys. Astrophys. Fluid Dynamics*, 39:119–147, 1987.